Delft University of Technology

Master Thesis

Acoustic Emission Detection of Kissing Bonds in Adhesively Bonded Composite Structures

Author:
Rowan Heckmanns

July 1, 2025

Preface

This thesis is conducted as part of obtaining my Master degree in Aerospace Structures and Materials at TU Delft. The thesis describes the manufacturing, testing and acoustic monitoring of bonded composite specimens containing artificial bond defects. Being able to design, produce and test my own specimens gave me a deeper understanding of working directly with composite material, while also allowing me the opportunity to become more experienced in performing complex data analysis of acoustic signals. I hope this research will be successful in furthering the development of Structural Health Monitoring methods for composite aircraft structures.

I would like to express my gratitude to Maarten Adams from SINTEG Systems, who made this thesis a possibility. I am grateful for his guidance and everlasting support over this past year. Additionally, I would like to thank my colleagues at SINTEG, for supporting me in my endeavors. A special thanks goes to Pooria Pahlavan and all other team members from SHM Next for their support and kindness.

I would also like to give a special thank you to Christos Kassapoglou, who gave me the best supervision any student could ask for. It has been my privilege to have him as my supervisor.

I would like to thank Sofia Teixeira de Freitas and Dimitrios Zarouchas for their insights regarding the technical subject matter of this thesis. Additionally, I would like to thank all staff from DASML at the Aerospace Engineering faculty for assisting me in the production and testing of my specimens.

Lastly, I would like to thank my friends and family for their support and encouragement over all these years.

Rowan Heckmanns
Delft, July 2025

Abstract

The increased use of adhesively bonded joints in aerospace structures has given rise to ample research opportunities on the topic of ensuring structural integrity. One such method of verifying bond strength is through the use of non-destructive testing methods. One particular defect type, kissing bonds or zero-volume bonds, is notoriously difficult to detect using traditional techniques such as ultrasonic C-Scan. This thesis explores the feasibility of using Acoustic Emission (AE) monitoring to detect defects and characterize failure modes for adhesively bonded composite joints. Numerous Double Cantilever Beam (DCB) specimens containing various defect types were manufactured and tested under static Mode I loading conditions. Defect types included were pristine specimens, inclusion defects and artificial kissing bonds replicated through contamination of the adherend surface using release agent.

Mechanical testing revealed that bondline defects significantly reduce the effective fracture toughness G_{eff} of defective specimens and induced alternative failure modes instead of complete cohesive failure. Most notably, specimens contaminated with release agent showed adhesion failure consistent with kissing bond type defects, while remaining undetectable when using conventional ultrasonic C-Scan inspection. AE monitoring allowed for identification of signal characteristics corresponding to cohesive failure, delamination and adhesion failure caused by kissing bonds and other defect types.

Clustering of acoustic signals revealed characteristic frequency bands for certain defect types and failure modes. In particular, a cluster of signals of 130 [kHz] and 170 [kHz] peak frequency respectively could be correlated to delamination and cohesive failure. Wavelet transforms of the measured signals further revealed the broad frequency spectrum present in all specimen types. However, inconsistencies in the characteristic failure modes attributed to certain frequency bands make this mode of identification insufficient in its current state to detect failure modes with complete certainty.

Contents

List of Figures **6**

List of Tables **9**

1 Introduction **12**
1.1 Composite Materials in Aircraft Structures . . . 12
1.1.1 The Demand for Lightweight Structures in Aviation . . . 12
1.1.2 Composite Structure Usage in Aviation . . . 13
1.2 Introduction to Adhesive Bonding . . . 14
1.3 Adhesive Bonding in Aerospace . . . 14
1.4 Structure of the Report . . . 15

2 Adhesive Bonds in Aerospace Structures **16**
2.1 Composite Material Characteristics and Failure . . . 16
2.2 Joining of Composite Structures using Mechanical Fasteners . . . 17
2.3 Adhesive Bonding Principles . . . 18
2.3.1 Adhesive Bonds as Fastening Method . . . 18
2.3.2 Fundamental Mechanisms of Adhesion . . . 20
2.3.3 Physics of Adhesion . . . 20
2.4 Failure Modes for Adhesively Bonded Structures . . . 22
2.4.1 Bond-Line Failure Modes . . . 23
2.4.2 Adhesive Bond Defects . . . 24
2.4.3 Loading Conditions and Failure Modes . . . 26
2.5 Surface Preparation for Adhesion . . . 27
2.5.1 Cleaning and Mechanical Pre-Treatment . . . 27
2.5.2 Chemical Surface Preparation for Metals . . . 28
2.5.3 Surface Activation for Composites and Metals . . . 29
2.5.4 Summary of Preparation Methods . . . 30
2.6 Adhesive Types for Composites and Metals . . . 32
2.7 Environmental Effects on Adhesive Bond Failure . . . 33
2.8 Certification Challenges and Bond Inspection . . . 36
2.8.1 FAA Regulations and Implications . . . 36
2.8.2 Conclusion on Certification of Adhesive Bonds . . . 37

3 Nondestructive Testing (NDT) Methods for Adhesive Bonds **38**
3.1 Introduction to NDT . . . 38
3.2 NDT for Bonded Joints . . . 38
3.2.1 Ultrasonic Testing . . . 39
3.2.2 Guided Ultrasonic Waves . . . 39
3.2.3 Acoustic Emission . . . 40
3.3 Comparison of NDT Methods . . . 41
3.4 Conclusion and Motivation for AE Monitoring . . . 42

4 Acoustic Emission Monitoring **43**
4.1 Fundamentals of AE . . . 43
4.2 Principles of Acoustic Emission . . . 43
4.2.1 AE for Aviation Applications . . . 44
4.2.2 The Kaiser Effect . . . 44
4.2.3 Challenges in Acoustic Emission . . . 45
4.3 Signal Processing of AE Events . . . 45
4.3.1 Damage Source Localization Method . . . 45
4.3.2 Wave Counting Method . . . 46
4.3.3 Cumulative Energy Method . . . 47
4.4 Acoustic Emission in Adhesively Bonded Structures . . . 47
4.4.1 AE in Adhesive Bonds . . . 47
4.4.2 Detection of Kissing Bonds using AE . . . 47

5 Research Proposal **48**
5.1 Literature review . . . 48
5.1.1 Acoustic Emission Testing in Literature . . . 48
5.1.2 Preemptive Detection of Kissing Bonds . . . 48
5.2 Research Objectives . . . 49
5.3 Research Hypothesis . . . 50
5.4 Expected Results and Impact . . . 50
5.5 Summary of Research Scope . . . 51

6 Methodology **52**
6.1 General Methodology . . . 52
6.2 Specimen Design . . . 53
6.3 Acoustic Emission Analysis . . . 54
6.4 Signal Processing . . . 54

7 Specimen Production **56**
7.1 Carbon Fiber Adherend Material . . . 56
7.2 C-Scan of Composite Material . . . 56
7.2.1 C-Scan Properties . . . 56
7.3 Production of Carbon Material . . . 57
7.4 Adhesive Material . . . 63
7.4.1 Production . . . 63
7.5 Contamination . . . 64
7.6 Production of Defects . . . 65
7.6.1 Pristine and Adhesive Film defects (P & AC) . . . 66
7.6.2 P & AC C-Scan . . . 66
7.6.3 Release Agent Contaminated Specimens (RA-U) . . . 69
7.6.4 RA C-Scan . . . 69
7.6.5 RA-O C-Scan . . . 74
7.7 Specimen Final Preparation . . . 75
7.8 Summary . . . 76
7.9 Discussion . . . 77

8 Mechanical Tests **79**
8.1 Test Setup and Method . . . 79
8.2 Data Processing . . . 80
8.2.1 Local Fracture Toughness G_{Ic} . . . 80
8.2.2 Global Effective Fracture Toughness G_{eff} . . . 82
8.3 Mechanical Test Results . . . 82
8.3.1 Pristine Specimens (P) . . . 82
8.3.2 Adhesive Film Carrier Specimens (AC) . . . 91
8.3.3 Release Agent Specimens (RA) . . . 96
8.4 Comparison of Results . . . 103
8.4.1 Local Fracture Toughness G_{1c} Comparison . . . 103
8.4.2 Global Effective Fracture Toughness G_{eff} Comparison . . . 105
8.5 Discussion . . . 107

9 Acoustic Results **108**
9.1 Test Setup . . . 108
9.2 Data Processing . . . 108
9.3 Data Analysis . . . 109
9.3.1 Pristine Specimens . . . 109
9.3.2 Defected specimens . . . 115
9.3.3 Comparison Defects and Pristine . . . 120
9.3.4 Cumulative Acoustic Energy and Fracture Toughness . . . 121
9.4 Acoustic Emission Clustering . . . 122
9.4.1 Unsupervised Clustering . . . 122
9.4.2 Identification of Failure Modes using Manual Clusters . . . 128
9.5 Wavelet Transform . . . 132
9.5.1 Preemptive Detection of Kissing Bonds . . . 133
9.5.2 Spectrum Comparison including All Signals . . . 137
9.6 Discussion . . . 139
9.7 Conclusion on Acoustics . . . 141

Conclusion **143**

List of Figures

1 Comparison of materials used in Airbus A320 and A350 XWB. 13
2 Failure modes for a fiber reinforced composite laminate (adapted from [21]). 17
3 Mechanical fastener failure modes (adapted from [73]). 18
4 Stress distribution for conventional fasteners and adhesive bonds [55] 19
5 Polarity of a water molecule 21
6 Bondline Failure Modes (Adapted from:[60]) 23
7 Common defects in adhesives (adapted from [12]) 25
8 Surface of a metal adherend [57] 28
9 Hydrophilic / Functional Groups (Adapted from [43]) 30
10 Flowchart of steps needed for proper surface preperation for metal and composite adherends. 32
11 Contact Angle Measurement (Adapted from [43]) 34
12 Visual representation of the Water Break Test (Adapted from [4]) 35
13 Guided Waves vs. Ultrasonic Testing (Adapted from [23]) 40
14 Active acoustic monitoring vs. Passive acoustic monitoring [22] 40
15 AE Events originating due to slip (Adapted from: [72]) 44
16 Noise and Threshold value (Trigger level) of an acoustic signal [49] 45
17 2D AE source localization using two sensors [74] 46
18 3D AE source localization using two sensors[36] 46
19 Flowchart showing the signal transformation in an acoustic emission system, from source to measured signal. 49
20 Specimen Defect Types 52
21 High Peel Stresses in Adhesive Bondlines [7] 53
22 DCB Specimen Geometry 54
23 Ultrasonic C-Scan (Immersion) 57
24 Composite stack placed on prepared tool with unperforated release film as a base layer 58
25 C-Scan of Composite Plate at Initial Manufacturing Stage 59
26 Comparison of C-Scan dB Reduction: 3H vs 18H Debulked Carbon Composites . . . 59
27 Carbon 18 Hour Heated Debulk 60
28 Carbon 18 Hour Heated Debulk - Added Dwell Stage 61
29 Curing Cycle as per Specifications 62
30 Alternative Curing Cycle with Added Dwell Stage 62
31 Curing Cycle used for Curing the Adhesive 64
32 Defect positioning and size - full width 65
33 Defect positioning and size - circular 65
34 Adhesive Carrier Film remaining on the adherend surface 66
35 P & AC Specimen Stack C-Scan 67
36 P Specimen Stack C-Scan 67
37 AC Specimen Stack C-Scan 68
38 Singular P-Specimen C-Scan 68
39 Singular AC Specimen C-Scan 69
40 Carbon plate used for Release Agent (RA) Specimens 70
41 Release Agent Stack complete C-Scan 71
42 Release Agent Stack - Covered during Corona Plasma Treatment 72
43 Release Agent Stack - Uncovered during Corona Plasma Treatment 72
44 Singular RA-C Specimen C-Scan 73

45 Singular RA-U Specimen C-Scan . . . 73
46 Release Agent Stack complete C-Scan - Circular . . . 74
47 Release Agent Stack - Uncovered - Circular . . . 75
48 Specimen Geometry with Sensor Placement . . . 79
49 Force-Displacement Curve - All Pristine Specimens . . . 83
50 Fracture surfaces of pristine specimens: (a) P1, (b) P2, (c) P3 . . . 84
51 Fracture surfaces of pristine specimens: (d) P4, (e) P5 . . . 85
52 Baseline Pristine Average Load Displacement curve . . . 86
53 Crack Length vs. Displacement with Force-Displacement Curve for Specimen P1 . . 86
54 Comparison of Crack Length and Force-Displacement Curves for specimens P2 to P5 (Part 1) . . . 87
55 Mode I fracture toughness (G_{Ic}) as a function of crack length for pristine specimens: (a) P1, (b) P2, (c) P3. . . . 89
56 Mode I Fracture Toughness (G_{Ic}) as a function of crack length for pristine specimens: (d) P4, (e) P5. . . . 90
57 Force-Displacement Curves AC-Specimens . . . 91
58 Post-test fracture surfaces of artificially contaminated specimens: (a) AC1, (b) AC2, and (c) AC3. . . . 92
59 Comparison of Crack Length and Force-Displacement Curves for AC2 and AC3 . . . 94
60 Fracture Toughness G_{Ic} versus crack length for artificially contaminated specimens: (a) AC1, (b) AC2, and (c) AC3. . . . 95
61 Force-Displacement curves of RA-U Specimens compared to Pristine Specimens . . . 96
62 Post-test fracture surfaces of RA-U specimens: (a) RA-U1, (b) RA-U2, and (c) RA-U3. 97
63 Inter-Laminar Shear Failure events for RA-U2 and RA-U3, highlighted in red 98
64 Crack length and force-displacement behavior of RA-U specimens: (a) RA-U1, (b) RA-U2, (c) RA-U3. . . . 99
65 Mode I Fracture Toughness (G_{Ic}) plotted over crack length for RA-U specimens: (a) RA-U1, (b) RA-U2, (c) RA-U3. . . . 100
66 Force-Displacement curves of RA-C Specimens compared to Pristine Specimens . . . 101
67 Post-test fracture surfaces of O-series specimens: (a) O1, (b) O2, and (c) O3. 102
68 G_{Ic} plotted over crack length distance – RA-O1 . . . 103
69 Comparison between P & AC Specimens - G_{1c} . . . 104
70 Comparison between P & RA Specimens - G_{1c} . . . 105
71 All Acoustic hits captured during testing - P2 . . . 109
72 Increase in hits at point near maximum load . . . 110
73 All Acoustic hits captured during testing - P2 - Highlighted AE Hit Bursts 110
74 Total cumulative hits measured compared to force - P2 . . . 111
75 Total cumulative energy measured compared to force . . . 111
77 Cumulative Hits - P1 . . . 112
76 Hits detected during testing - P1 . . . 112
78 Cumulative hits comparison between partially delaminated specimen (P1) and cohesively failed specimens (P2-P5) . . . 113
79 Cumulative energy comparison between partially delaminated specimen (P1) and cohesively failed specimens (P2-P5) . . . 113
80 Deviation in cumulative hits - pristine specimens (cohesive failure) . . . 114
81 Deviation in cumulative acoustic energy - pristine specimens (cohesive failure) 114
82 Hits detected during testing - AC2 . . . 115
83 Total cumulative hits measured compared to force - AC2 . . . 116

84 Total cumulative energy measured compared to force - AC2 . . . 116
85 Cumulative hits comparison between AC specimens . . . 117
86 Cumulative energy comparison between AC specimens . . . 117
87 Hits detected during testing - P1 . . . 118
88 Total cumulative hits measured compared to force - RA-U2 . . . 118
89 Total cumulative energy measured compared to force - RA-U2 . . . 119
90 Cumulative hits comparison between RA specimens . . . 119
91 Cumulative energy comparison between RA specimens . . . 120
92 Cumulative hits comparison between specimen types . . . 120
93 Cumulative energy comparison between specimen types . . . 121
94 Acoustic signals grouped using a Automatic Clustering Approach - P2 (10.000 signals) 123
95 Comparison of unsupervised AE clustering for specimens P1 and P3. . . . 124
96 Clusters of P3 . . . 125
97 Clusters of AC2 . . . 126
98 Clusters of RA-U2 . . . 126
99 Heatmap of all clusters for all specimens . . . 127
100 Fracture surfaces of specimens M1, M2, and M3. . . . 129
101 Heatmap of all clusters for all specimens (Mist added) . . . 130
102 Bridging of Adhesive Carrier fibers . . . 131
103 Morlet Wavelet Transform of an Acoustic Signal - P2 . . . 132
104 Morlet Wavelet Transform of an Acoustic Signal - P3 - Cluster 3 . . . 133
105 Morlet Wavelet Transform of an Acoustic Signal - RA-U1 - Cluster 6 . . . 133
106 Scattering observed in signal frequency spectrum prior to reaching contaminated area. - RA-U1 . . . 134
107 Scattering observed in signal frequency spectrum in pristine specimen - P3 . . . 135
108 Examples of transformed signals across three specimens, showing presence or absence of high-frequency scattering. . . . 136
109 Signature Frequency Spectrum of P1 . . . 137
110 Signature Frequency Spectrum of AC2 . . . 138
111 Signature Frequency Spectrum of RA-U1 . . . 138

List of Tables

3 Comparison between mechanical fasteners and adhesive bonding methods 20
4 Typical Defects in Adhesive Bonds and their Associated Failure Modes 25
5 Surface Preparation Methods for Adhesive Bonding 31
6 Comparison of Conventional UT, Guided Waves and Acoustic Emission (AE) 41
7 Comparison of NDT Techniques for Adhesive Bond Evaluation 42
8 Acquisition Parameters for C-Scan. 57
9 Thickness measurements of specimen over bonded area 76
10 Global Effective Fracture Toughness G_{eff} for different Specimens 105
11 Comparison of G_{eff} values of specimens to average of P2 - P5. 106
12 Acquisition parameters for AE measurements. 108

Nomenclature

Abbreviations

Abbreviation	Definition
AC	Adhesive Carrier film
AE	Acoustic emission
AET	Acoustic Emission Testing
CFRP	Carbon fiber reinforced polymer
CTE	Coefficient of thermal expansion
DCB	Double Cantilever Beam
FAA	Federal Aviation Administration
GUW	Guided Ultrasonic Waves
ILSF	Inter laminar shear failure
MBT	Modified Beam Theory
NDT	Non-destructive testing
NDI	Non-destructive inspection
P	Pristine
PCA	Principal Component Analysis
PMC	Polymer Matrix Composite
RA	Release Agent
SHM	Structural Health Monitoring
SOM	Self-Organizing Map
TDOA	Time difference of arrival
UT	Ultrasonic Testing

List of Symbols

Symbol	Definition	Unit
a	Crack length	[mm]
b	Specimen width	[mm]
Δ	Crack correction factor	[mm]
Δa	Bond crack length	[mm]
δ	Cross-head displacement	[mm]
θ	Contact angle	[rad]
E	Elastic modulus	[Pa]
F	Correction factor	[-]
G_{eff}	Global effective fracture toughness	[J/m^2]
G_{Ic}	Mode I fracture toughness	[J/m^2]
G_{TOT}	Total energy release rate	[J/m^2]
P	Applied load	[N]
S	Signal frequency	[kHz]
t	Time	[s]
U	Area under Force-Displacement curve	[N $\cdot$ mm]

1 Introduction

The following thesis is a study on using Acoustic Emission (AE) for detecting defects in adhesively bonded composite structures. A literature review is conducted, which acts as the foundation of the coming research by exploring the current technological developments and industry challengers regarding this objective.

The increased demand for composite structures in the aerospace industry will be outlined, along with the current technological challenges. The advantages of using adhesive bonds in composite structures will then be explained, along with the current challenges that are preventing this excellent form of mechanical fastening from being implemented to the fullest potential. Lastly, the current selection of Nondestructive Testing (NDT) methods available in the current day will be named, explained and compared to determine which methods are suitable for analyzing such structures.

1.1 Composite Materials in Aircraft Structures

1.1.1 The Demand for Lightweight Structures in Aviation

Modern aviation has revolutionized global mobility. It has enabled people to connect, develop international business relations and relocate more efficiently than ever. Economic growth in the developing world has caused an increasing demand for commercial aviation, bringing more people together every day.

However, this growth does come at an environmental cost. In 2012, commercial aviation has accounted for 1.3% in global CO_2 emissions. While seemingly small, this contribution is expected to rise to 22% of global CO_2 emissions by 2050 due to a rise in global demand [47].

To meet current objectives of international climate agreements, such as the Paris Accords, the amount of CO_2 emitted by aircraft must be continuously reduced through innovation. The current Paris Agreement states that aviation must reduce emissions by 50% before 2040 and net zero by 2050 [27]. Efforts to achieve these goals include the development of alternative propulsion methods, such as electric, hydrogen-powered aircraft, as well as the adoption of sustainable aviation fuel. Alongside advancements in the ways of propulsion, improved structural efficiency is another key part of sustainable design.

One of the key aspects of reducing emissions is by reducing the structural weight of an aircraft. Between 1960 and 2018, the aviation sector has made steady progress by continuously reducing the CO_2 emitted per passenger per kilometer by 87.5%, thanks to in large part the introduction of more efficient turbofan engines and the increased uses of lightweight design and materials such as carbon-fiber composites [39]. Aircraft designed using lightweight composite structures directly reduce fuel consumption and as a result, reduce emissions and operating costs. When aircraft transition to a structure made primarily of composite materials, an estimated contribution of 20-25% of the industry CO_2 reduction target can be realized [71].

Additionally, in zero-emission concepts, such as hydrogen-powered aircraft, composite materials play a different and important role. Due to their high specific strength, composites are currently being used to produce pressurized and cryogenic tanks, allowing for hydrogen to be stored using minimal

weight while containing the extreme pressures and thermal loads.

While composite components produce more emissions and are more energy-intensive to manufacture when compared to conventional aluminium structures [71], life-cycle assessment of commercial aircraft reveal that less than 1% of total CO_2 emissions is contributed to the production of the aircraft. The remaining 99% of total emissions during the entire life and use of a commercial aircraft are resulting from burning fossil fuels [62]. Therefore, any reduction in the operating emissions can have great impact on the overall sustainability of an aircraft during its operational lifetime [71].

In addition to the environmental impact of lightweight structures, reducing the amount of fuel used per passenger introduces financial incentives. Reducing fuel consumption directly reduces operating cost, which is one of the driving factors behind technological developments in the aviation industry. They are critical for airline fleet selection and competitiveness in innovation between aircraft manufacturers.

1.1.2 Composite Structure Usage in Aviation

With the need for structurally efficient aircraft established, the aerospace industry is rapidly shifting toward the adoption of carbon fiber reinforced polymers (CFRP's). These materials allow for structurally efficient designs that reduce carbon emissions, improve efficiency and lower operational cost. This emphasizes the role composite materials will have enabling the next generation of sustainable aircraft.

Carbon Fiber Reinforced Polymers have been developed and produced as a material since the 1950's. However, they have only recently been used for larger structural components in aircraft. The first aircraft to have its fuselage and wings made out of majority composite being the Boeing 787 Dreamliner, introduced in 2013. A direct comparison in material use between the Airbus A320 and newer Airbus A350 XWB can be found in Figure 1.

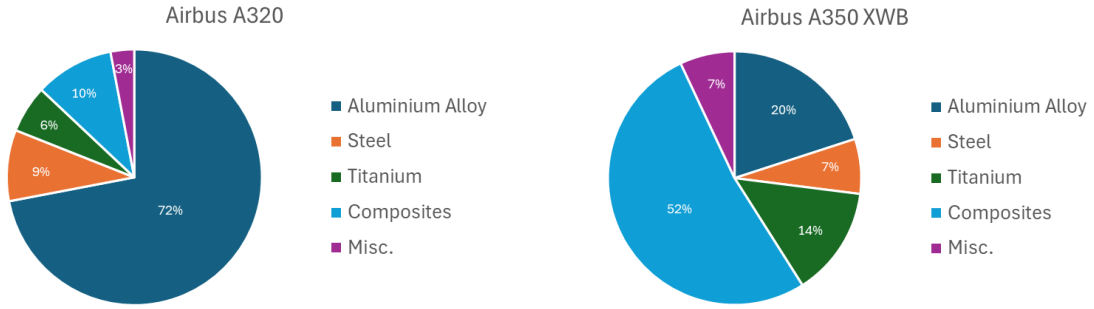

(a) Airbus A320 (introduced in 1984) [3]

(b) Airbus A350 XWB (introduced in 2013) [31]

Figure 1: Comparison of materials used in Airbus A320 and A350 XWB.

Composite materials are characterized by being made of two or more materials with different material properties [25]. Typically, a strong and stiff component is present, known as the reinforcement.

These reinforcements are bounded in a softer component material, often referred to as the matrix material. The matrix acts as a binder for the composite material, as it protects the reinforcement from the environment, keeps the reinforcement together and transfers stress within the material.

Fastening composite parts together to create larger structures such as fuselages and wings seems an appropriate alternative to creating large, single part structures. It is therefore also the current industry standard, making the joining of components a large contributor to the manufacturing process.

1.2 Introduction to Adhesive Bonding

The method of joining structural composite parts is becoming increasingly more important. Mechanical fasteners such as bolts and rivets have been the industry standard for metallic structures in the past, but their usage in composite structures has certain design challenges. Drilling fastener holes for bolts and rivets in composite material damages the reinforcing fibers, causes cracks in the resin matrix and can result in delaminations [35] [64]. Fastener holes or inserts can be added into the design of the composite part itself, reducing the need for post-manufacturing drilling. Additionally, inserts are embedded in the material, but only held together by the weaker matrix material of the composite.

Post-manufactured holes also allow for more flexible positioning when joining parts, reducing the need for stricter tolerances when accounting for variations in the part geometry due to manufacturing variables [73].

Traditional fasteners are made from high-density metals, adding to the weight and complexity of the structure. These metals, including aluminium, titanium alloys and types of stainless steel when in contact with the composite material can also cause galvanic corrosion [45]. When fasteners are exposed to a corrosive environment, galvanic corrosion is amplified [54]. Galvanic corrosion also plays a factor when bonding dissimilar materials, such as when fastening carbon composite to aluminium structure, either through direct contact or using metallic fasteners [56] [42].

1.3 Adhesive Bonding in Aerospace

With the growing demand for usage of composite materials in the aerospace industry, the traditional method of joining using mechanical fasteners often introduces the aforementioned challenges such as added weight, stress concentrations and galvanic corrosion when in contact with carbon-fiber based components. An alternative mechanical fastening method is using adhesive bonding.

Adhesive bonding offers a lightweight, corrosion-resistant alternative, which also enables the more uniformly transfer of load imposed by fastener holes. Adhesive bonding has therefore taken center stage when it comes to enabling the design of lightweight, fuel-efficient aircraft designs and is increasingly used for primary and secondary structural applications.

While promising, adhesive bonds have their own technological challenges. Environmental durability, bondline defects and difficulties with regards to quality assurance severely reduce the reliability and usage of adhesive bonds in primary structures. Adhesive bonds, unlike mechanical fasteners, can not be as easily verified using visual inspections. This critical concern creates challenges when it comes to certification of bond structures and long-term reliability of bonded components.

1.4 Structure of the Report

This thesis is presented as follows. Chapter 2 will explore the fundamentals of adhesion, the types of adhesives used in aircraft structures and the current technological challenges preventing broader adoption of adhesive bonding in the modern day aerospace industry. Chapter 3 will explain different nondestructive testing methods, highlighting its potential strengths and weaknesses when it comes to bondline detection. Chapter 4 will highlight the fundamentals of Acoustic Emission. This method is used to detect elastic waves caused by damage propagation. Next, in chapter 5 the research proposal is described based on the gaps found in literature and chapter 6 discusses the research method. This includes the distinction of different types. The samples are tested using a Double Cantilever Beam (DCB) tests. Additionally, the method of capturing acoustic signals which will be related to the failure being induced at that given time is outlined. Chapter 7 describes the steps involved in producing the specimens whereas chapter 8 shows the results of the mechanical test. Chapter 9 shows the final acoustic results. Lastly, in chapter 10 the conclusions of the research will be stated.

2 Adhesive Bonds in Aerospace Structures

To understand the role of adhesives in aerospace structures, it is important to review composite material behavior, fastening methods for composites and the technological challenges involved. These will be presented in this chapter.

2.1 Composite Material Characteristics and Failure

Most commonly, these reinforcements are made of polymer fibers, such as carbon polymer chains being the reinforcing component in carbon fiber. These types of composite are called Polymer Matrix Composites (PMCs). Depending on the direction of the fibers within the material, the material has different material properties in different directions. This is called an anisotropic material. In general, fiber reinforced composite material is strongest and stiffest when it is loaded along the fiber direction, where the reinforcing fibers can most effectively carry loads. It is consequently weaker when it is loaded in the transverse direction, where only to weaker matrix material holds the composite together.

Composite material is made out of layers, where a singular example is referred to as a lamina. Most commonly it has fibers in either one direction (Unidirectional) or in two directions perpendicular to each other (multidirectional or woven). By stacking multiple layers of composite sheets or lamina, a laminate is created.

The ability to optimize each layer in the composite, combined with the anisotropic nature of the material itself, specific material properties can be designed to be used for specific use cases. This allows for creating lighter-weight structures when compared to conventional, isotropic materials such as aluminium.

Due to the way composites are manufactured, careful consideration must be made when designing larger aircraft structures. Larger and more complex single aircraft parts have an increased likelihood of containing manufacturing defects. For defects which can not be restored, such large complex parts are often scrapped which adds to the total cost of production. It is at times beneficial to create multiple smaller parts which can be attached together to create a coherent structure. This in turn requires additional steps, curing cycles and methods of fastening which can also be costly [30].
Because composite material is composed of two or more constituents, there are more ways for the material to fail when compared to metals [75]. This is complicated by the fact that the material will behave differently depending on the manner or direction it is loaded in, again differentiating itself from metal materials. The main failure modes for fiber reinforced composites are:

1. **Delamination:** Separation between the composite layers in the laminate, caused by impact events or inter-laminar shear loads.
2. **Fiber Failure:** Breaking of the reinforcing fibers due to excessive load.
3. **Matrix Failure:** Cracking and failure of the matrix material due to excessive loads.
4. **Fiber pullout or de-bonding:** Detachment of the fibers from the surrounding matrix material without the fibers themselves breaking.

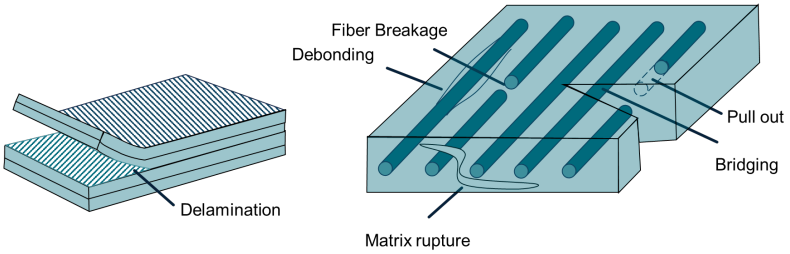

Figure 2: Failure modes for a fiber reinforced composite laminate (adapted from [21]).

Due to the fact that composite materials are composed of two or more components, it is generally more difficult and costly to manufacture. Challenging stages of manufacturing involve high temperatures and pressures in order to allow for the necessary chemical reactions. This complex manufacturing process increases the likelihood of the final material containing manufacturing defects [48]. Defects in the matrix material or defected reinforcement fibers can drastically reduce the strength and durability of the material. Manufacturing defects common in these materials are voids or larger delaminations and poor matrix resin distribution.

Composite aerospace structures therefore are typically assembled from smaller composite components joined together. This requires a reliable method of joining, using either mechanical fasteners or adhesive bonding. Each of these techniques has its own engineering challenges. Both methods are explored in the following section.

2.2 Joining of Composite Structures using Mechanical Fasteners

Mechanical fasteners can lead to several failure modes in the composite material due to higher stress concentrations, including Tension Failure, Shear-Out Failure and Bearing failure as can be seen in Figure 3 [73].

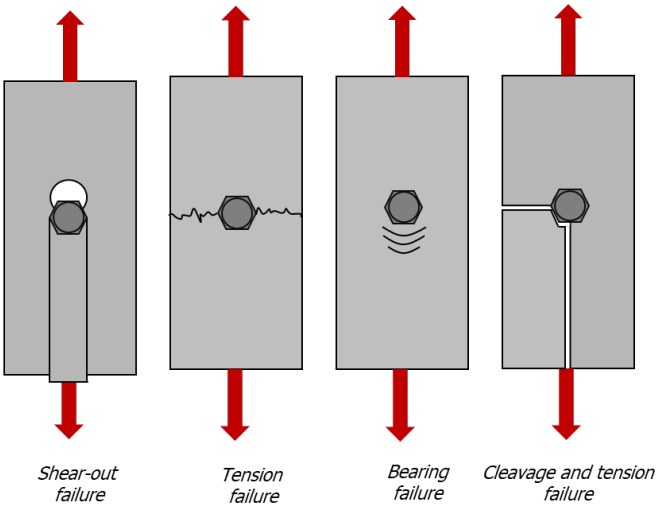

Figure 3: Mechanical fastener failure modes (adapted from [73]).

Bolted joints in ductile metal structures have the advantage of being able to yield, redistributing the stress to surrounding material and reducing stress concentrations around the bolt hole itself. Composite structures however do not have such advantage [51].

The edges of the hole themselves can be prone to delaminations, caused by either the drilling operation itself or the loading subjected to the fastener while in use [26] [35]. In general, using the fasteners also increases the total weight of the structure and can greatly increases cost due to assembly time [30].

2.3 Adhesive Bonding Principles

2.3.1 Adhesive Bonds as Fastening Method

Adhesive bonds grant several advantages over traditional fasteners in terms of structural effectiveness and manufacturing efficiency. Adhesive bonding is especially interesting for composite structures as opposed to metallic structures, as the previously mentioned structural complications introduced by using mechanical fasteners have shown [9].

Adhesive joints allow for a better distribution of the stresses through the joint and surrounding structure. Due to the fact that no hole is required, it allows for a continuous bond and thus a more uniform stress distribution, as can be seen in Figure 4 [17].

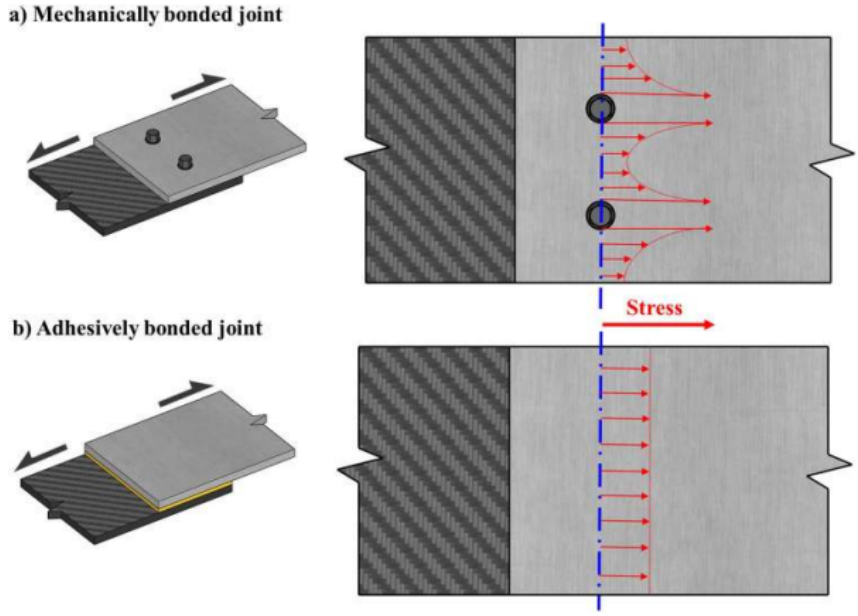

Figure 4: Stress distribution for conventional fasteners and adhesive bonds [55]

This reduction in peak stresses due to a more uniform stress distribution also causes adhesive bonds to perform better under fatigue loading. The delaminations caused by drilling traditional fastener holes can also be avoided by using adhesives. Such delaminations caused by drilling can grow significantly under fatigue loading [32]. Holes in any structure also cause stress risers, which can cause fatigue crack initiation and growth at those locations [52].

Adhesive bonds eliminate the risk of galvanic corrosion occurring in metallic fasteners when contacting composite material [59]. They also allow for more effective joining of dissimilar materials, due to the insulating properties of adhesives preventing galvanic corrosion in the base material itself [66] [65]. The manufacturing process itself is simplified due to reducing the number of components and assembly stages [30].

In short, adhesive joints have many advantages over traditional fasteners. They eliminate the need for heavy fasteners, which increase weight. The lack of holes in the structure allows for more efficient load distribution and reduces the need for additional reinforcements which further adds to lightweight design. Furthermore, uniform stress distribution allows for more optimal use of surrounding material. Structural components can be made thinner, as they no longer require a set thickness to accommodate fastener heads and nuts, further reducing structural weight.

Adhesives not only enable broader usage of composite materials in aircraft structures, the characteristics of adhesive joints themselves allow for an even lighter weight design method. Adhesive joints will play an increasing role of importance in the aerospace industry and will be a cornerstone for lightweight design, reducing emissions, operating cost and manufacturing waste.

While adhesives bonds show many advantages over mechanical fasteners, the complex nature behind producing reliably strong bonds remains one of the main challenges preventing manufacturers from using this to its upmost potential. Bonded joints require careful decontamination and surface preparation prior to bonding to ensure that the adhesive correctly sticks to the adherend material. Manufacturing defects and environmental exposure can also greatly affect the structural performance. An understanding of these underlying mechanisms of adhesion is therefore required in order to assess structure performance of any adhesive bond.

Table 3: Comparison between mechanical fasteners and adhesive bonding methods

Property	**Mechanical Fasteners**	**Adhesive Bonding**
Weight impact	High (fasteners + inserts)	Low
Stress distribution	Localized Concentrations	Uniform
Galvanic risk	Present	Low
Inspection	Possible visually	Difficult / not possible
Assembly	Simple	Complex

2.3.2 Fundamental Mechanisms of Adhesion

Definition of adhesion

The Federal Aviation Administration (FAA) defines a "bonded system" as a joint consisting of a base adherend material, a method of surface preparation, an adhesive material and a bonding process. This is according to a Recommendation Report on structural bonding signed and authorized by several large aviation manufacturers and operators, making it applicable to use as a broader definition for bonded aerospace structures [20]. Adhesion is defined as the adherence of materials due to interatomic and intermolecular forces between the surfaces of the adhesive and the attached surface [33].

2.3.3 Physics of Adhesion

It can be stated that there are two primary types of adhesion, namely physical adhesion and chemical adhesion.

Physical Adhesion: Involves intermolecular forces, which are attraction forces between different molecules. Two types of such forces are Van der Waals forces and Mechanical Interlocking.

Van der Waals Forces: Molecules are electrically neutral. They contain equal parts protons and electrons and thus have no overall charge. Polar molecules however have an uneven distribution of electrons in their structure, causing permanent poles of electrical charge, similar to a magnet. One such molecule is water as can be seen in Figure 5.

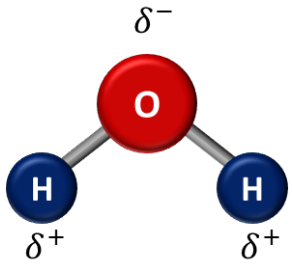

Figure 5: Polarity of a water molecule

Van der Waals forces are created when attraction occurs between different molecules due to opposite poles in the molecular structure. These forces are called intermolecular, as the attraction is between different molecules. Van der Waals forces are increased when acting on an "attractive surface". Such a surface is said to have a high Surface Energy.

Surface Energy

Surface energy refers to the amount of attractiveness of a surface to other molecules. Water for example has a high surface energy, evident by water droplets maintaining their shape and sticking together. Polyethylene has low surface energy, making it difficult to adhere or paint any polyethylene surface.

Hydrogen Bonds

Hydrogen bonds are a type polar interaction commonly between hydrogen [H] and Oxygen [O] atoms between different molecules. Hydrogen bonds create stronger and more directional forces compared to Van der Waals forces and occur between highly electronegative atoms and hydrogen, such as H-O, H-N and H-F.

Hydrogen bonds are caused by dipole-dipole interactions. A water molecule like mentioned before and in Figure 5 has strong polar interactions. It has a highly positive hydrogen part and is bonded to a highly electronegative oxygen atom. Oxygen wants to complete it's outer atomic ring and thus shares an electron with the hydrogen atom. Hydrogen by already being small and having to share its single electron means it becomes highly positive in this case, creating strong interactions with other polar molecules.

While Van der Waals and hydrogen bonds can affect adhesion greatly, their contribution for creating a strong, adhesive bond is minimal [33]. However, for the purposes for creating a strong bond, using a surface with high surface energy can greatly improve adhesion. When a surface has high surface energy, it is referred to as being more "wettable". The surface is more attractive, causing adhesive material to spread consistently over the desired area. This allows for the creation of stronger chemical bonds.

To test the wettability of a surface, water break tests are conducted prior to adhesion to test the reactivity of the surface before bonding. Usually, a certain amount of water is dropped on the surface. If the water beads up, this is an indication of the surface not being prone to chemically bond. This

could be due to oxide layers in case of metals or the presence of contamination. If the water spreads out, this shows the surface is more accustomed to bonding. By measuring the angle at which the water drop contacts the surface, surface energy can be made quantifiable [68].

Mechanical Interlocking: Occurs when an adhesive physically grips into a rough surface. This can be either through a rough or porous surface. The adhesive is embedded in the microscopic gaps in the adherend surface, causing an increased bond strength. Mechanical Interlocking is a mechanical effect and does not involve molecular interactions. In terms of structural adhesion, mechanical interlocking can not be relied upon and under peel loading and tensile loading, it is small in terms of providing structural rigidity by itself [13].

Surface roughness can however significantly contribute by being more receptive to chemical bonds, as well as by providing more surface area for the adhesive to bond to. These additional chemical bonds allow for a much stronger type of adhesion, namely chemical adhesion [13].

Chemical Adhesion: is achieved through chemical bonds, more specifically for adhesives covalent bonds. Covalent bonds are a strong, permanent bond created through chemical reactions. As a result atoms between the adhesive and the adherend surface share electrons, creating atomic bonds.

Chemical adhesion is highly resilient to environmental exposure. This is due to covalent bonds being more resistant to degradation of various types including thermal influences, mechanical loading and chemical reactions once cured. A strong, reliable bond means that chemical bonding is essential to the aviation industry, where reliability of a structure behaving as anticipated is of importance.

In order to achieve a strong chemical bond, proper steps have to be taken. Chemical adhesion is highly dependent on the surface chemistry of the adherend. Firstly, a surface has to be free of contaminants, such as dirt or grease. This can stop an adhesive from bonding to a surface as it acts as a barrier, not allowing the needed chemical reactions to take place. Secondly, a reactive interface between the adhesive and adherend surface must be created in order covalent bonds to form. In order to achieve good bonding, the adherend material must first have proper Surface Preparation compatible with the adhesive used. Surface preparation is thus an essential step to adhesive bonds and it can takes on many forms.

Various mechanisms thus contribute to adhesion itself. However, a bond can still fail due to mechanical loads, manufacturing defects or environmental effects. The following section outlines the failures that can occur in adhesive bonds.

2.4 Failure Modes for Adhesively Bonded Structures

Adhesive joints can fail under excessive loading like any other method of mechanical fastening. Improper bonding, material defects, environmental degradation or incorrect loading of the structure can all greatly reduce the load required to onset structural failure. These different failure mechanisms can be grouped into bond-line failure, manufacturing defects and loading-failure.

2.4.1 Bond-Line Failure Modes

The four main types of adhesive bond failure are [15]:

- **Cohesion Failure:** Fracture of the adhesive itself.
- **Adhesive Failure:** Failure at the adhesive and adherend interface.
- **Substrate Failure:** Failure of the adherend material.
- **Mixed Failure:** Combined failure of the bond due to multiple present failure modes.

These distinct failure modes have been visualized in Figure 6.

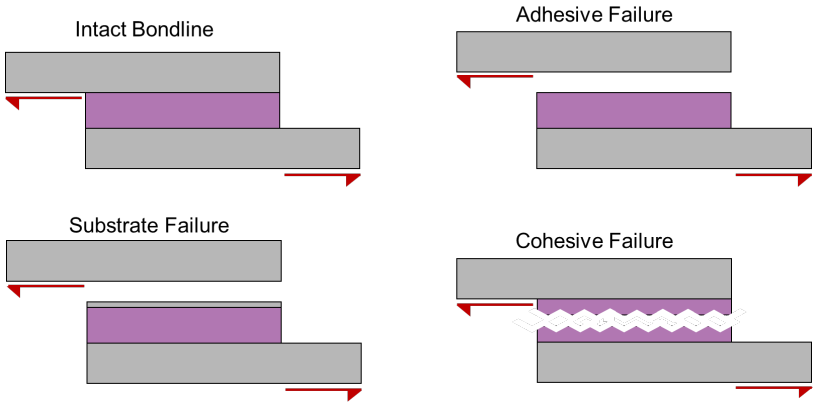

Figure 6: Bondline Failure Modes (Adapted from:[60])

Adhesion failure indicates that the formation of chemical bonds did not occur. This can be through contamination or insufficient surface preparation. It can also be due to improper curing of the adhesive and the bond being degraded over time [16]. In general, It is characterized by a smooth fracture surface, with the adhesive completely detaching from one side of the adherend surface Adhesion failure is associated with weak bonds and low failure loads compared to cohesion failure [16]. Cohesion failure occurs when good adhesion between the surfaces is achieved, but the adhesive itself fractures under load. It is characterized by adhesive material being attached on both adherend surfaces [16].

Mixed failure occurs when there is partial cohesion failure and partial adhesion failure. This is due to a partial lack of bonding at the interface. It is characterized by the fracture surface showing both a smooth surface where no bond formation occurred and a rough surface of still attached adhesive material where bond formation did occur. Because part of the bond showed cohesive failure, the strength of this bond is in between complete adhesion and complete cohesion failure [16].

Substrate failure occurs when the bonded joint shows a higher strength than the adherend material. This allows the bonded joint to be fully utilized in terms of structural performance [15]. If the adhesive bond is strong enough such that the adherend material surrounding the bond will fail first, the bonded joint may be certified by testing only the surrounding structure to show sufficient structural performance [14].

2.4.2 Adhesive Bond Defects

Defects present in adhesive bonds can significantly affect strength and durability of a bonded component. These defects result resultant from either manufacturing defects or develop while in service [64].

Manufacturing Defects: are a result of improper manufacturing, surface preparation and curing of the adhesive. The manufacturing defects found in adhesive bonds are:

- **Voids & Porosity**: Trapped air in the adhesive bond reduces the load-bearing capability of the adhesive. Voids are large air pockets in the adhesive material, while a porous adhesive shows small air pockets distributed in the adhesive, either locally or completely. Voids can be formed due to exposure of adhesive film to moisture due to improper storage [15].
- **Surface Disbonds:** Surface disbonds are caused by trapped air in between the adhesive and interface [64].
- **Poor adhesion:** Either caused by inclusions, contaminants or improper surface preparation. This disrupts the interface between the adhesives and adherend [64].
- **Kissing Bonds:** These are a unique type of defect caused by local disbonding, with no significant gap in between the adhesive and adherend. They are also called zero volume disbonds [64]. They are a type of surface disbond, but are placed in a separate category due to their significant impact on joint strength and the extreme difficulty of detection using nondestructive testing methods [64].
- **Contamination or Inclusion:** Contamination such as dust and grease can cause insufficient chemical bonds to form between the adhesive and adherend, which promote interfacial or adhesion failure.
- **Improper Curing:** Caused by incorrect pressure, temperature or fabrication, chemical bonds within the adhesive are weakened, causing cracks to form in the adhesive itself.

Each of the defect types has their own impact on bond performance in different ways, depending on size, severity and applied loading. Table 4 summarizes the most common defects types.

Table 4: Typical Defects in Adhesive Bonds and their Associated Failure Modes

Defect Type	Description	Likely Failure Mode
Voids / Porosity	Trapped air bubbles or incomplete contact at the adhesive / adherend interface	Cohesive failure (due to stress concentrations), early crack initiation
Surface Disbonds	Lack of contact between adhesive and adherend	Adhesion failure (no chemical bonding at the interface)
Kissing Bonds	Zero-volume disbond at the interface, conventionally undetectable	Adhesion failure or sudden mixed failure under load
Improper Curing	Incomplete crosslinking of adhesive	Cohesive failure (reduced strength), fatigue sensitivity
Contamination (Grease, Dust)	Surface layer prevents formation of chemical bonds	Adhesion failure, inconsistent bond strength
Inclusions	Unintended particles embedded in the adhesive	Localized cohesive failure or delamination
Adhesive Cracks	Pre-existing cracks in the adhesive layer	Crack propagation sensitive to fatigue, cohesive failure

Voids, porosity and surface disbonds are defect types that reduce strength of the adhesive itself, increasing likelihood of cohesive failure [16]. An overview of defects that can occur in adhesive bonds is shown in Figure 7.

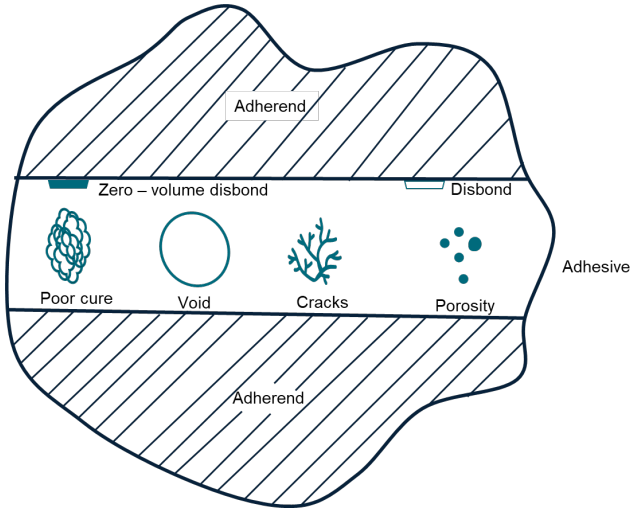

Figure 7: Common defects in adhesives (adapted from [12])

In-Service Defects: can be caused by environmental exposure or loading events. Defects such as disbonds can be caused by impact events.

- **Disbonds due to Impact:** Can originate during service related incidents such as tool drops or in flight events such as bird strikes.
- **Environmental Effects:** Excess moisture, degradation from UV exposure and thermal effects can weaken the bond over time.
- **Galvanic Corrosion:** While less prevalent in composite structures, exposed carbon fibers can undergo galvanic corrosion and lead to degradation of the bonded structure.

2.4.3 Loading Conditions and Failure Modes

Tensile Loading

Under tensile loading, stress is usually distributed, the load is therefore distributed over the entire bond line. Weak adhesion results in adhesion failure. If adhesion is strong, the resulting failure mode is cohesive failure or substrate failure, depending on which has the higher overall strength. Adhesion defects however can weaken the strength of the adhesive under tensile loading, causing early onset of cohesive failure or crack initiation. Voids can act as nucleation points for crack initiation, inclusions act as stress concentrations and improper curing leads to reduced tensile strength of the adhesive material.

Shear Loading

Shear Loading is the most applicable and common load condition found in aviation structures. Shear forces act parallel to the surface of the adhesive, meaning they act on the adhesive layer. If the adhesive is well bonded to the substrate, cohesion failure occurs when the shear stress exceeds the shear strength of the adhesive material.

Adhesive defects can onset early failure under shear loading conditions. Improper cure, voids and cracks can significantly reduce shear strength of the adhesive. Larger voids can have the ffects of reducing the effective bonding cross sectional area between, acting as local stress concentrators.

The composite material can also greatly affect shear strength of the bond. A 90-degree fiber layer contacting the adhesive can result in significantly reduced shear strength compared to a composite lay-up where the outside layer is a 0-degree ply. Besides the local weaker interface between the adhesive and composite, the inefficient distribution of stresses from the material to the adhesive can also cause stress concentrations [55].

Peel Loading

Peel loading causes high stresses at the edges of adhesive bonds. This load is directed to the interface between the adhesive and the substrate. If the adhesion between the adhesive and substrate is weakened, this results in separation of the two at lower loads due to weaker adhesion failure occurring. Adhesive defects that promote failure under peel loading are related to weakened bonds between the composite and adhesive, caused by improper surface treatment or contamination. Improper curing can also prevent from the necessary chemical reactions taking place, causing adhesion

failure under peel loads.

Fatigue Loading

Cyclic loading causes degradation of the adhesive over time. This can occur as a result of mechanical cyclic loading or thermal cyclic loading. This loading can result in crack nucleation and propagation, both of which can be accelerated through environmental exposure. These cracks eventually act as stress concentrations, leading to cohesive failure of the bond. Fatigue life can be reduced through defects in the adhesive, such as existing cracks, voids and porosity or moisture absorption, leading to the weakening of chemical bonds. Despite these risks for failure, a well bonded adhesive can be highly resistant to fatigue loading [2].

Understanding how bonds may fail highlights the critical importance of proper surface preparation, quality control and selection of adhesives with sufficient strength.

2.5 Surface Preparation for Adhesion

The effectiveness of adhesive bonds is highly sensitive to a range of influencing factors. The strength and reliability of bonded joints are not only determined by the adhesive itself, but also by how well the bonded surfaces are prepared, the effects of the environment during and after bonding and the effects of contamination of the bond layer itself.

This section highlights the critical contributing factors to bond quality, including surface preparation, sources of contamination and the forming of chemical bonds to the substrate. Understanding these factors is essential to ensuring an structurally strong bond required in aerospace applications.

2.5.1 Cleaning and Mechanical Pre-Treatment

Prior to the formation of chemical bonds, the adherend surface must be clean and uniform. Contaminants such as grease, dust or oxidation must be removed as they prevent molecular bonds from forming. Cleaning and abrasion methods remove these contaminants and prepare the surface for chemical bonding.

Degreasing / cleaning: An important step required for any adhesion application process, even for simple household applications. Many know any application process begins with a clean surface. Contaminates are removed from the surface and is typically done with isopropanol or acetone. Other similar detergents can be used for this process dependent on the process. This step is applicable to both metallic and composite materials.

Mechanical abrasion: Abrasion can be performed using sanding or grit blasting. This step is used to create a uniform surface, increase surface area and improve mechanical interlocking to achieve a stronger bond [29]. Mechanical abrasion can also be used as a method of cleaning, ensuring the surface is free from dust, grease and unwanted oxide layers [33]. It is applicable to both metallic and composite materials. For composites however, care needs to be taken to not damage the fibers or excessively damage the resin.

2.5.2 Chemical Surface Preparation for Metals

For metallic bonding, oxide layers and hydrated surfaces inhibit the formation of chemical bonds. These layers are formed over time when a metal surface is exposed to the atmosphere. The substrates must be removed or made more stable through methods such as etching and anodization. Primers can also be applied to increase compatibility with adhesives and to protect the treated surface.

Etching: This step removes metal oxide layers using either highly acidic or highly alkaline fluids [12]. Exposed metal over time naturally creates an natural oxide layer when exposed to the environment. Figure 8 shows in detail the surface of a metal oxide surface. The different layers consist of the following:

- Metallic layer. This consists of pure aluminium atoms
- Metal oxide layer: This is a thin oxide layer that forms when the aluminum reacts with oxygen in the air. It consists of aluminum and oxygen atoms (Al2O3).
- Hydroxide (OH) layer: When exposed to the environment, the metal oxide layer can absorb moisture from the air. The surface becomes hydrated and less stable [57].
- Hydrated water layer: Over time, the oxide surface can absorb water molecules, forming a hydrated layer that weakens the adhesion potential.

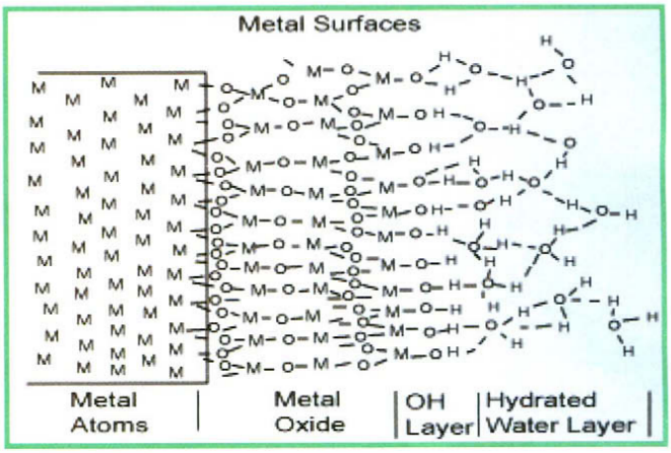

Figure 8: Surface of a metal adherend [57]

Chemical etching removes this layer such that only the bare metal remains. It can also remove organic contaminants and be used to change the topography of the surface for better bonding [12]. This step is usually followed by an anodization process. This step is applicable to metals.

Anodization: this step, often done after etching, recreates a uniform, thicker oxide layer on metal surfaces. This oxide layer is less hydrated and thicker, making it more stable when compared to a natural oxide layer. The hydroxide layer and hydrated water layer are no longer present.Therefore the outer most layer which contacts the adhesive is an aluminum oxide layer. The oxygen atoms are

receptive to forming atomic bonds with reactive groups in the adhesive, creating strong atomic bonds.

The anodization step can also create a porous structure, making it easier for a viscous adhesive to seep in and create mechanical interlocking. This step is applicable to metals.

Over time when exposed to the environment, hydrated layers can reform. Bonding soon after anodization is recommended, in order to protect the anodized layer. Priming is also often performed.

Priming: is often performed after anodizing. It protects the newly made oxide layer. For example, it stops the oxide layer from becoming hydrated due to moisture. Certain primers also act as a chemical bridge, promoting the creation of chemical bonds. Certain adhesives do not bond well directly to a metallic oxide layer. Primers can enhance compatibility between the adhesive and the substrate, containing functional groups that make the primer compatible with both. Primers also preserve the porous structure created in the anodization step when appropriately applied. Priming can also be done for composite materials after a previous surface preparation step such as sanding or plasma treatment to preserve the surface and make it more chemically compatible with adhesives.

2.5.3 Surface Activation for Composites and Metals

Next to mechanical and chemical preparation of the surface, surface treatment methods such as Plasma Etching and UV/Ozone Treatment can further change the surface chemistry of the material. These methods introduce functional groups. These increase wettability of the surface and promote the formation of chemical bonds with the adhesive. This is especially relevant for composite materials were etching is not viable.

Plasma Treatment: a plasma flame is applied to the surface. This ionizes the gas supplied through the plasma torch. In composites, this creates a chemically active surface by introducing functional groups that bond strongly to the adhesive. This also creates a more wettable surface [43] and also removes contaminants at the same time. When plasma treating composites, it is important to avoid thermal degradation effects such as melting of the thermoplastic polymer matrix due to applied temperatures when thermoplastic adherends are used [61]. For metals, the hydrated surface layer is removed and the oxide layer is thickened and made more uniform. Plasma etching also increases roughness for metallic surfaces. [28]. It also adds functional groups and removes contaminants.

Plasma etching can be done using several gasses, including regular air. It can be done under pressure or under atmospheric conditions. Atmospheric plasma etching as a method for surface preparation has been used in industry by large manufacturers such as Boeing for consistency and reliability for the bonded surface [9]. Using plasma treatment for decontamination can be considered more effective when compared to chemical solvents as it reduces the need for working with flammable and chemical waste [28] [67].

UV / Ozone: This process uses UV light and Ozone gas to create highly reactive atomic oxygen and once again introduce functional groups on the substrate. The atomic oxygen also oxidizes surface grease and other contaminants, thus also cleaning the substrate itself. It is therefore very comparable to Plasma Treatment. It is applicable for both metals and composites.

Both Plasma treatment and UV Ozone treatment creates functional groups. These are either oxygen based Hydroxyl (-OH) or nitrogen based Amine (-NH2) groups. These functional groups are highly reactive and bond strongly to reactive groups in adhesives [67]. For example, epoxy based adhesives contain Epoxide (-C-O-C-) which creates covalent bonds with Hydroxyl and Amine groups introduced to the surface due to Plasma treatment of UV Ozone [8] [67].

As a secondary effect, functional groups also function as hydrophilic groups. These groups improve surface wettability allowing the adhesive to spread and flow more effectively [67]. Functional groups also increase Van der Waals interactions and the improved wettability increases the ability for the adhesive to mechanically lock into surface irregularities, but as mentioned before these contribute minimally to the total strength of the adhesive joints.

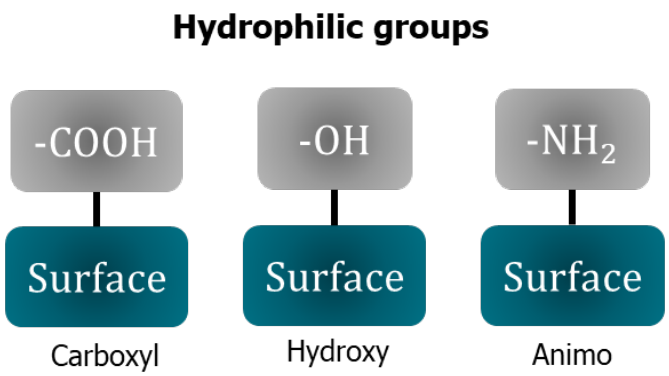

Figure 9: Hydrophilic / Functional Groups (Adapted from [43])

2.5.4 Summary of Preparation Methods

Table 5 gives an summarizes these main methods of surface preparation, related steps required and the key points.

Table 5: Surface Preparation Methods for Adhesive Bonding

Surface Preparation Method	Adherend	Prior Steps Required	Key Points
Degreasing / Cleaning	Metals & Composites	None	Removes contaminants, usually using chemical solvents. Improves adhesive bonding.
Mechanical Abrasion	Metals & Composites	None	Increases surface area for better mechanical interlocking. Can damage composite fibers.
Etching	Metals	None	Removes oxide layers, improving adhesive bonding.
Anodization	Metals	Etching (recommended)	Creates a stable, thick oxide layer that improves bonding. Can add porosity for mechanical interlocking.
Priming	Metals & Composites	Often after anodization	Enhances adhesive bonding, acts as a chemical bridge. Preserves porous anodized surface.
Plasma Treatment	Metals & Composites	None	Introduces functional groups, increases wettability, and removes contaminants.
UV/Ozone Treatment	Metals & Composites	None	Introduces functional groups and removes contaminants.

Figure 10 shows step by step the surface preparation steps required for both metallic and composite materials. Please note that some steps might be optional, depending on the other processes used for preparing the surface. This figure will be used as a general reference for the upcoming research.

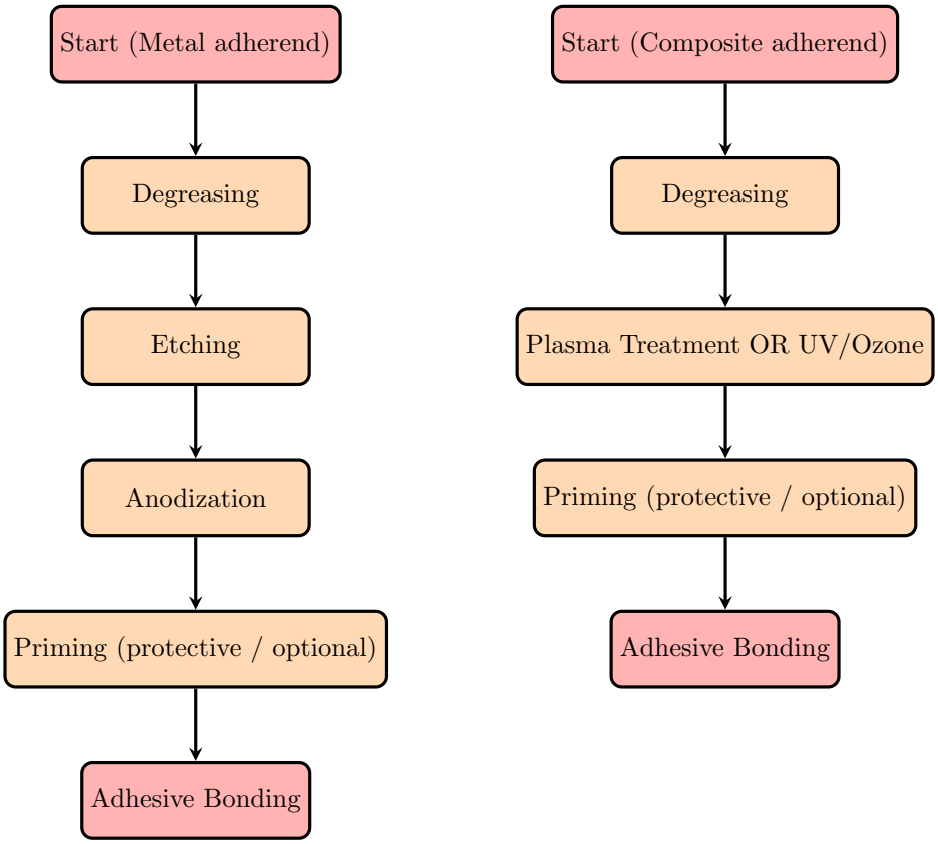

Figure 10: Flowchart of steps needed for proper surface preperation for metal and composite adherends.

Conclusions Chemical vs. Physical Bonds
Chemical bonds are the primary driving force behind strong and durable adhesives when compared to physical bonds [33]. However, physical adhesive forces have also been researched in this review for it is still of essence to consider its contribution. Chemical bonds are sensitive to improper surface preparation methods, curing cycles or surface contamination. If any of the surface preparation steps is compromised, it can completely halt the formation of strong chemical bonds. When these fail to develop, the only resulting adhesion remaining are driven by physical phenomena. This can be considered a "weak bond". It is not always self evident that a weak bond has formed as partial adhesion still remains. When a smaller area of a bond is compromised, it is likely hidden while still being surrounded by a strong bond.

2.6 Adhesive Types for Composites and Metals

For structural aircraft applications the most commonly used structural adhesives for both composite and metal structures are epoxy based adhesives and structural acrylic adhesives:

Epoxy based Adhesives: widely used due to high strength, resistance to increased temperatures,

chemical solvents and other environmental effects [1].

Epoxy based adhesives are especially applicable for composites containing an epoxy-based matrix as both the adhesive and composite resin are similar in chemical structure. The adhesive itself is also able to create a cross-linked network, increasing bond strength [67]. Additionally, epoxy based resins react strongly to Hydroxyl groups, allowing for strong covalent bonding if such functional groups are present after surface treatment [50] [67]. Similar coefficients of thermal expansion (CTE) also minimize thermal stresses which could cause delaminations or bond failure. This is especially relevant for aerospace applications that undergo significant thermal changes. Being comparable in curing cycles, epoxy-based adhesives are regularly cured alongside the composite material, reducing the number of total curing cycles needed to create a bond.

Epoxy-based adhesives are regularly used for bonding metal surfaces [67]. However, due to metals typically having a higher CTE which can become problematic with epoxy based adhesive when undergoing large temperature fluctuations.

Structural acrylic adhesives: characterized by their high strength and are also use for structural applications. Due to their higher flexibility compared to epoxy based adhesives, they are more applicable for bonding metals than composites as they can reduce thermal stresses improved by temperature changes in metals with a higher CTE. This is especially relevant for structures undergoing regular thermal cycling.

2.7 Environmental Effects on Adhesive Bond Failure

Contamination: can be considered any unwanted substance on the surface which can affect adhesion such as dust, grease and natural oxidation.

- Dust can be considered as any fine particle present on the surface. This could occur during the manufacturing process of the joint, improper storage or transportation between different manufacturing stages. Dust prevents the adhesive from distributing properly on the surface. It also acts as a physical barrier between the adhesive and adherend surface, preventing the formation of chemical bonds.
- Grease often contaminates a surface due to improper handling. Grease from touching the material without protective gloves, can be sufficient enough to act as a barrier preventing chemical bonds from forming. It also reduces surface energy, decreasing wettability making it more difficult for the adhesive to form a strong bond.
- Natural oxidation, especially in aluminium alloys can lead to improper bonding as previously stated in subsection 2.5. A natural oxide layer can be considered a contamination if its presence is not intended, due to for example improper removal or reformation after prior surface preparation steps due to being exposed to the environment for sufficient enough time. In metal bonds, hydration of the oxide layer is one of the primary causes of failure [16].

The effects of contamination can be severe. Most forms of contamination reduce the formation of chemical bonds. It must therefore always be minimized through the following methods:

- Materials must be stored in controlled environments to reduce exposure to dust, moisture and other contaminants.

- Protective films should be used to prevent contamination of either the adherend material or the adhesive.
- Production should be done in an environmentally controlled environment with controlled humidity.
- Production should be done in a clean environment in order to prevent dust or grease from contaminating the surface. For critical applications, production should be done in clean-rooms or highly controlled environments to avoid the spread of dust.
- Minimize transport or movement of materials.
- Minimize human contact with bonding surfaces. Clean gloves should be worn to avoid contaminating surfaces with grease or dust.
- clean environment and prevent dust from settling on surface.

Many surface preparation methods are used for cleaning adherend surfaces as discussed in subsection 2.5. After such steps, several methods exist to determine if the decontamination was successful.

One common method is using Contact Angle Measurements. This method evaluates surface wettability by measuring the angle between a drop of water and the adherend surface, as can be seen in Figure 11. A low contact angles indicates a more wettable surface, indicating successful decontamination and a clean surface which allows the liquid to spread. If the contact angle is high, wettability is low indicating contamination such as grease. Using accurate camera's, contact angles can be accurately quantified in order to give an indication for surface cleanliness [68].

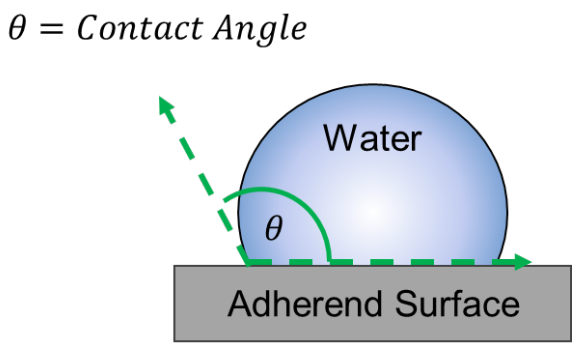

Figure 11: Contact Angle Measurement (Adapted from [43])

Another such method is the Water Break Test. This test is more simplified and is based on observing how water behaves when sprayed on a surface. A continuous, thin film of water indicates a clean surface as the water is allowed to spread, indicating good wettability [70]. If the water beads up or breaks into multiple steams, this is an indication of contamination as can be seen in Figure 12. While simple and fast to perform, the test is reliant on the interpretation of the observer and less quantifiable [70].

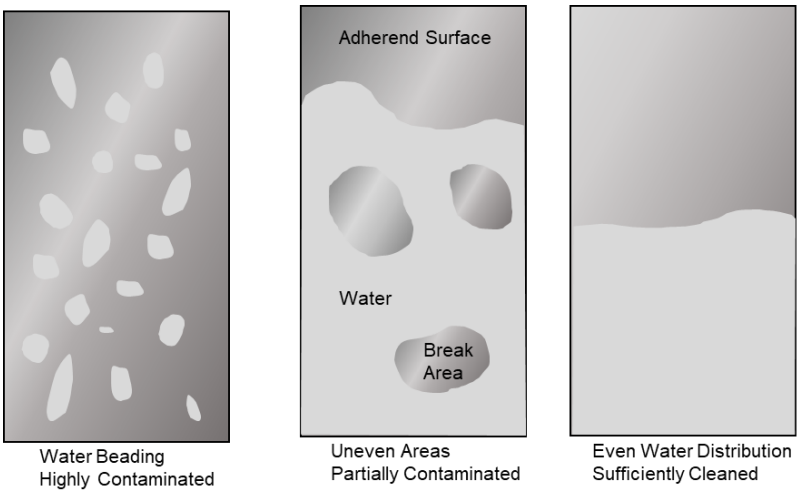

Figure 12: Visual representation of the Water Break Test (Adapted from [4])

For aerospace applications, contact angle measurements are preferred due to providing a quantifiable way of determining surface wettability. The measurable data can be used for quality control or validation of the surface preparation method.

Environmental Effects: One advantage adhesives have over traditional fasteners is a reduced risk of galvanic corrosion, as previously mentioned in subsubsection 1.1.2. However, adhesive bonds are not immune to being damaged through environmental effects.

- **Temperature:** thermal cycles cause expansion and contraction, especially for metals with a higher CTE. This difference in CTE between the adhesive and the adherend causes thermal stresses, which can promote crack growth. At higher temperatures, adhesives lose strength and stiffness due to thermal softening. At lower temperatures, adhesives can be prone to brittle failure. It is therefore important to use adhesive that remains stable under expected thermal conditions and to accommodate for thermal expansion of the joint.
- **Humidity:** over time, adhesive can absorb moisture, weakening chemical bonds. This is called Hydrolysis of the adhesive. Adhesives can also swell due to absorbing moisture, causing disbonding from the substrate [58] [64]. To minimize these effects, moisture-resistant adhesives can be used as well as using correct edge sealing methods to avoid trapping moisture within the bond.
- **UV Radiation:** this can cause polymers to degrade, breaking cross-linked polymer chains. Over time this can weaken the adhesive. Using coatings or primers which are UV-resistant can reduce this effect.
- **Aggressive Chemicals:** oils, fuels and fluids used in aircraft can degrade adhesives by weakening polymer material. Chemically resistant adhesives are preferred or the use of coatings and other protective layers can be used to avoid contact with the adhesive in case of fluid leaks.

2.8 Certification Challenges and Bond Inspection

2.8.1 FAA Regulations and Implications

Creating a reliable structural bond is a complex endeavor due to the many manufacturing, environmental and design complications. An added complexity is the irreversible nature of structural adhesive bonding. Additionally, adhesive bonds can not be visibly inspected to verify if good bonding was achieved.

Certification requirements exist in order to ensure that a bonded joint is sufficiently strong, despite possible manufacturing defects. The FAA mandates that any bonded joint, the failure of which would cause catastrophic failure of the aircraft, must have sufficient strength to carry the limit loads, as verified by either one of the three following methods [18] [19]:

1. Large disbond areas must be accounted for through design features that ensure that structural strength remains sufficient even if the adhesive joint partially fails.
2. Critical bonds in each production article are required to undergo proof testing which will apply the critical limit design load of the bond to verify structural strength.
3. Nondestructive inspection (NDI) methods must ensure that the strength of each joint is sufficient, repeatedly and reliably.

Here, nondestructive inspection or NDI is aligned with the terminology used by the FAA. In the reviewed literature and the following thesis, nondestructive testing or NDT will be used to describe the same technology and methods.

These three design requirements are created to take into account unknown manufacturing defects and their influence on the bond strength. However, they also introduce new challenges. Structural weight is increased by adding design features in order to satisfy method 1, for example large excess of adhesive area. It may also be the case that redundant fasteners are to be used as a mechanical backup in conjunction with the adhesive bond to provide sufficient strength to the structure should the bond fail [30].

Method 2, which requires proof testing of every production article by applying a certain limit design load to each critical bonded joint is impractical for large-scale manufacturing. While it would be a valid method to ensure structural integrity, it requires each critical bond to be loaded to near-destructive loads, which can significantly increase production time and cost [6]. Additionally, such tests do not account for weak bonds formed after manufacturing caused by environmental exposure over time and eventual bond degradation [19].

As both methods 1 and 2 show significant drawbacks, NDI introduces itself as the most practical alternative. NDI (or NDT) has the advantage of offering a non-invasive way to inspect bonds without adding significant weight to the structure, nor requiring costly proof loading of components. A reliable NDT method can reduce the use of conservative design, reducing the need for over-sized bondlines and redundant mechanical fasteners. However, current NDT methods have limitations, particularly in detecting weak bonds or kissing bonds [15] [16]. Currently, there are no reliable NDT methods that can accurately detect such defected bonds [30].

2.8.2 Conclusion on Certification of Adhesive Bonds

While adhesive bonding shows great promise for the development of lightweight aerospace structures, current certification requirements and the shortcomings of current NDT methods have required that adhesive joints be subjected to conservative design practices, increasing structural aircraft weight. Developing reliable NDT methods, particularly ones able to detect weak bonds or kissing bonds, could provide a more accurate assessment of bond strength, potentially reducing the need for weight increasing design features or extensive structural testing of each component. The following section will explore various NDT methods applicable to adhesive joints in more detail.

3 Nondestructive Testing (NDT) Methods for Adhesive Bonds

To ensure structural integrity of adhesive bonds, non-destructive testing (NDT) methods are used widely in the aerospace industry. These methods of inspection allow for the evaluation of bonds without damaging the structure. Certain defects, such as kissing bonds may have full geometric contact while showing little to no structural rigidity. These flaws can not be visually inspected and are often unable to be detected using conventional NDT methods. The following chapter provides an overview of the current used NDT techniques to study adhesive bonds, compare their effectiveness and highlight potential strengths and weaknesses. An emphasis is made on their ability to detect interface-level bond defects. Lastly a motivation for exploring Acoustic Emission (AE) monitoring as a potential method for detecting kissing-bond type defects is outlined.

3.1 Introduction to NDT

Nondestructive Testing (NDT) is a method of analyzing a structure, material or component without causing damage to the structure itself. Essentially, NDT allows one to use measurement techniques allowing to see into a material and detect hidden features or defects.

NDT methods can be utilized to determine if an adhesive bond was properly fabricated without containing inclusions or defects that can lead to early failure. Ideally, the objective of any NDT method is to directly correlate the strength of a joint to the measured parameter. As of current, there are no standardized NDT method used for certification of bonded structures [30]. Some defects are detectable, such as large disbonded areas, porosity and material inclusions [19]. However, monitoring interfacial bonding defects such as kissing bonds or weak bonds can not be done reliably [12] [19].

If a reliable, accurate and replicable NDT method is found certifying bondlines, this could lead to increase usage of adhesive bonds in aerospace structures, leading to weight reduction, emission reductions and cost reductions as outlined in Chapter 1.

Having discussed the various defect types in adhesive bonds in Chapter 2, it can be stated that kissing bonds are particularly challenging to detect. Whereas voids, inclusions and disbonds have detectable matter (either trapped air or contaminants such as debris), kissing bonds are caused by the lack of chemical bonds on the micro-scale. The detection of such bonds remains critical, as kissing bonds can greatly affect the integrity of bonded structures. These defects and their effect on the remaining bond strength are as of now, not accurately measurable using NDT methods [46] [30] [19].

The primary focus of this research is to further the development of reliable NDT techniques, with a primary focus on detecting kissing bonds in adhesively bonded composite structures due to this difficulty of detection, the challenges regarding certification and the critical consequences on structural integrity.

3.2 NDT for Bonded Joints

In order to allow for certification for bonded joints, Nondestructive Testing methods are to play a key role when it comes to guaranteeing structural integrity. The detection of flaws in adhesive

bonds requires highly sensitive and reliable NDT methods, especially for flaws such as kissing bonds. Among all available NDT methods, Guided Ultrasonic Waves (GUW), Acoustic Emission (AE) and Ultrasonic Testing (UT) show to be most applicable.

3.2.1 Ultrasonic Testing

Ultrasonic testing is an active monitoring method for detecting larger defects in adhesive bonds. The method works through a pulse-echo. It sends high-frequency acoustic waves into the material and can identify structural damage based on changes in the measured response [64]. Using the known wave speed and subsequent time delay, the reflected waves can be used to locate defects when the expected reflection shows irregularities.

Applications: Ultrasonic testing can be used to detect minor, local defects with high resolution. It can detect a defect shape, size and location with great accuracy. It is therefore widely used as a NDT method for detecting delaminations, voids and gaps in composites and adhesives. Two common ultrasonic techniques include A-Scan and C-Scan. A-Scan uses pulse-echo, sending signals into a material and detects reflections of this signal which interact with internal defects and features. It is therefore able to identify defect depth and location by only scanning one side. C-Scan uses a through-transmission approach, where ultrasonic signals are transmitted through the thickness and measured on the opposite side. Defected areas with delaminations, voids and inclusions attenuate the transmitted signal, which can be detected as a reduction in signal amplitude.

Limitations: While UT is accurate, it requires point-by-point inspecting. This means only a small area can be inspected at a time, making it unfeasible for large aircraft structures. It is also challenging to use for complex structures or curved surfaces. Lastly, due to the fact that kissing bonds have no internal volume of trapped air, the interface between adhesive bond containing kissing bonds is acoustically identical to a perfect bond. This renders kissing bonds largely invisible to pulse-echo UT methods. One method of UT testing is C-Scan, which has shown to be unable to detect kissing bonds [68].

3.2.2 Guided Ultrasonic Waves

GUW uses pulses elastic waves that travel along the length of a structure, unlike traditional Ultrasonic Testing which travels through the thickness of the material. These guided waves can travel long distances with minimal disturbance or energy loss, making them ideal for inspecting large areas or plate-like structures. When guided waves encounter defects in a structure, the propagation of these waves changes, which can be compared to a reference signal and analyzed to determine defect type and size. It is used primarily in pipelines, as the large surface area and simplistic structure allows for highly effective inspections [23].

Applications: Because they can inspect large areas quickly, it is more efficient compared to Ultrasonic Testing, which has to be conducted point-to-point. This difference in inspected area is visualized in Figure 13. It is highly sensitive in detecting disbonds, delaminations in composite structures. Guided waves can also be used for real-time monitoring by using permanent transducers and sensors. This is called Continuous Wave Generation, but is used more rarely compared to the alternative real-time monitoring technique, which is Acoustic Emission monitoring.

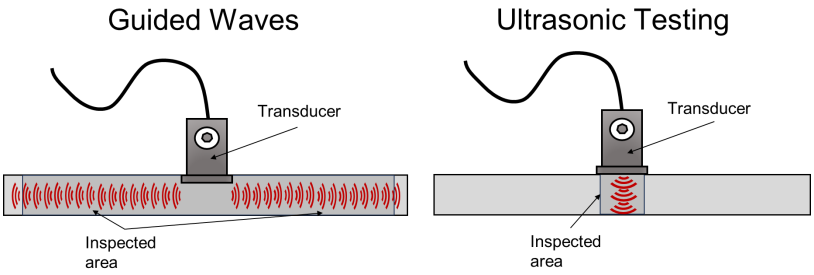

Figure 13: Guided Waves vs. Ultrasonic Testing (Adapted from [23])

Limitations: Guided waves require advances signal processing due to the wave complex nature. The waves tend to disperse, reflect and attenuate which becomes exponentially more difficult in complex structures. Additionally, it's effectiveness is limited when it comes to the detection of kissing bonds. As the interfacial effects of kissing bonds are less suitable for detection when compared to the primary use of GUW, which is detection of larger disbonds.

3.2.3 Acoustic Emission

Acoustic Emission, unlike active measuring methods such as Ultrasonic Testing and Guided Ultrasonic waves is a passive NDT method. It detects elastic waves through the release of energy in a material caused by a defect growing or appearing [22]. Sensors are used to detect these stress waves, allowing for identification of the damage and to locate defects or cracks. The difference between active and passive acoustic NDT techniques is shows in Figure 14.

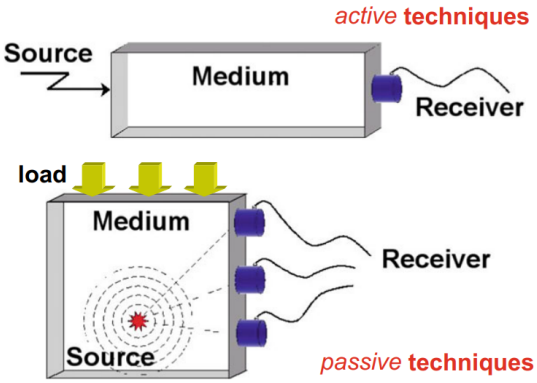

Figure 14: Active acoustic monitoring vs. Passive acoustic monitoring [22]

Applications: Unlike UT and GUW, Acoustic Emission monitors the structure in real time, making it ideal for detecting defects such as growing delaminations or cracks [22]. Like GUW, large areas can be covered [64]. Additionally, the passive nature of Acoustic Emission Monitoring allows sensors to be permanently installed in location inaccessible for inspectors using other NDT methods [49].

Limitations: Acoustic Emission signals can contain a lot of noise, especially in complex structures [64]. It requires precise calibration and it is up to interpretation what certain signals mean. Additionally in bonded composite structures, it can be difficult to distinguish between composite failure or adhesive failure due to similarities in emitted waves by each failure mode [41].

AE is widely defined as a method of Nondestructive Testing. However, due to the fact that AE requires damage to propagate or occur in order to detect the released energy, it can be said that it should not be defined as a nondestructive. Waves can thus also only be detected while undergoing loads and is not applicable under static conditions. Acoustic Emission monitoring is therefore often referred to as a Structural Health Monitoring methods or SHM. However, some do insist that AE is nondestructive, as it measures degradation under working load while other NDT measurement techniques measure degradation prior and after working load, making little difference to the end results of detecting damage [22].

For detecting adhesive defects, Acoustic Emission allows for accurate detection of adhesive defects and failures, such as adhesion failure, cohesion failure and crack growth. More importantly, AE has shown to be able to detect kissing bonds, but only when bonds are actively failing [68].

3.3 Comparison of NDT Methods

An overview of the features and characteristics of each method is shown in Table 6.

Table 6: Comparison of Conventional UT, Guided Waves and Acoustic Emission (AE)

Feature	**Ultrasonic Testing**	**Guided Waves**	**Acoustic Emission**
Real-Time or Periodic Inspection	Periodic, Point-by-point inspection	Periodic and Real-Time monitoring (limited)	Real-Time (Passive, detecting active defects)
Data Collection	Manual scanning	Continuous wave propagation	Detects stress waves from active defects
Structural Loading	Not required	Not required	Required
Defect Type	Static defects	Static and active defects	Active defects
Kissing Bond Detection	Limited effectiveness	Possible with nonlinear techniques	Effective if actively failing

Next to their technical capabilities. Each NDT method's capability towards detecting adhesive bond defects is outline in Table 7.

Table 7: Comparison of NDT Techniques for Adhesive Bond Evaluation

Technique	**Detects of Kissing Bonds**	**Depth Penetration**	**Comments**
Ultrasonic Testing	No	Moderate	Poor sensitivity to low-contrast disbonds
Guided Ultrasonic Waves	Limited	Long-range Surface Level	Suitable for structural health monitoring, but struggles with interfacial defects
Acoustic Emission	Potential	High (indirect)	Promising for in-situ monitoring, but requires interpretation

Of the reviewed monitoring methods, Acoustic Emission is most promising for detecting kissing bonds due to its sensitivity to damage propagation and the ability to monitor in real-time. By passively monitoring large surfaces for active damage, including crack growth and adhesion failure, AE can act as a first warning for damage being present under real loading conditions [22]. It's sensitivity to damage progression also provides insights in the integrity of an adhesive bond in general.

Additionally, AE has shown to be able to detect early signs of bond degradation. AE monitoring is proven to be able to detect environmental effects such as moisture absorption, that weakens bonds of time [15]. This ability is especially important to ensure long-term durability of adhesive bonds, given that degradation of the interface is a common cause of failures observed in aircraft while in-service [16].

3.4 Conclusion and Motivation for AE Monitoring

AE monitoring is likely not a standalone method for complete grasping the extend of structural damage When damage is detected through AE, more detailed inspection using Guided Ultrasonic Waves can be conducted. AE's ability of real-time monitoring for damage, combined with other scanning NDT methods and visual inspection of the surface could lead to accurately detecting and sizing damage [22].
Due to AE indicating where damage is expected to be, in-situ inspection can now be done in specific areas instead of all bonded joints in the whole structure. Periodic inspection of the entire structure, especially in aircraft can be costly and time-consuming causing aircraft to be grounded for exceedingly long periods of time. Thus, AE and GUW allow for local, detailed inspections only in the areas where it is needed, when it is needed. This method is expected to reduce maintenance time by up to 40%, greatly reducing costs [64].

This research will proceed by using Acoustic Emission testing to detect kissing bonds in adhesively bonded composite structures. This approach is based on the potential of AE as a powerful method for Structural Health Monitoring. The research aims to further develop AE monitoring techniques, enhancing the fields understanding of making kissing bonds reliably detectable, which could possibly lead to a certification method for adhesive bonds in aircraft structures.

4 Acoustic Emission Monitoring

Acoustic Emission (AE) monitoring is defined as a method of detecting elastic waves, originating from a release of energy in a structure caused by initiating or growing damage. Acoustic Emission monitoring, also known as Acoustic Emission Testing (AET) is used to detect such elastic waves using piezoelectric sensors [6].

4.1 Fundamentals of AE

The idea of using acoustic waves to detect the condition of a material is not a recent development. As early as 6500 BC, potters are believed to have recognized that cracking sounds from ceramic pots cooling after firing indicated signs of material failure. This can be regarded as the earliest form of acoustic-based monitoring of a structure [53]. Similarly, the audible cracking of wood under stress, such as those present when harvesting a tree, provides data of the current state of the wood undergoing stress. These are intuitive examples of structural degradation emitting acoustic signals. The first scientifically described AE test was described in 1934, where a metal probe would be inserted in wood, detecting through elastic waves and sounds while fracturing [34]. This laid the foundation of modern Acoustic Emission Monitoring, which was more formally defined in the 1950s. Modern day AE monitoring refers to the detection of elastic waves traveling through a structure or material using piezoelectric sensors. These detected waves are in the ultrasonic frequency range, generated by microscopic failure events [22].

4.2 Principles of Acoustic Emission

When damage occurs or grows in a material, elastic energy is released. Some is turned into heat or plastic deformation of the crystal structure. A portion of this energy is converted into elastic waves or acoustic waves. Elastic waves can be resultant from an energy release caused by a growing defect such as crack initiation or growth, delamination of a composite laminate and reinforcement fiber breakage. These waves can be detected using sensors, such as piezoelectric sensors. A detectable acoustic signal as a result of damage propagation is called an AE event. These events are captured through sensors placed on the surface of the structure, or can be embedded in a material itself. These waves are also known as stress waves.

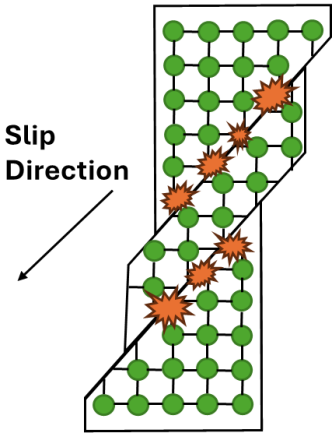

Figure 15: AE Events originating due to slip (Adapted from: [72])

4.2.1 AE for Aviation Applications

AE monitoring has seen usage for several applications in the aerospace industry. One such example is the evaluation of pressure vessels, such as composite hydrogen or other propellant tanks. Additionally, sensors can be placed on a multitude of structural components. The passive nature and real-time monitoring capability of AE monitoring allows for the detection of damage initiation or growth during use under operational loads.

In recent years, AE monitoring has played an increasingly important role for Structural Health Monitoring (SHM) systems. Here, continuous monitoring can optimize maintenance strategies based on local condition measurements gathered by acoustic signals. Such systems can allow future generation aircraft to operate with reduced downtime and maintenance cost through the implementation of digital twin analysis. For aircraft maintenance, AE is especially useful in structures where access is limited for visual inspection. Here, AE monitoring offers a lightweight and nondestructive method for monitoring a structure in-situ.

When considering adhesively bonded structures, AE shows the ability to detect damage initiation and growth under load in real time. However, the integration of these measurements techniques into a certified procedure is still an ongoing effort, largely due to the technological challenges with interpretation of the acoustic signals.

4.2.2 The Kaiser Effect

The Kaiser Effect states that once a defect within the material emits an acoustic signal due to an applied stress, the structure must then be subjected to an even higher stress in order to release more acoustic emissions. A crack for example can only be detected as it is growing due to a load higher than all previous loads already applied to the structure. This assumption is applicable under static loading conditions. Acoustic Emissions can still be detected at stresses below a previous maximum, such is the case for crack growth under fatigue loading conditions. This is known as the Felicity Effect. Both are of importance, as they govern the irreversible nature of AE monitoring [49] [69].

4.2.3 Challenges in Acoustic Emission

Due to this characteristic irreversibility of AE monitoring, signals originate only when under sufficient load. Therefore, AE monitoring can not be used to verify the presence or size of damage repeatedly, as active degradation is required. Acoustic measurements are also sensitive to background noise. This noise can originate from the structure itself (nearby machines, engines), from electronic disturbances (interference) or through environmental sources [49]. Such noise must be isolated through either physical means (such as psychically isolating the system from disturbances), or by using signal processing methods to filter out the noise as can be seen in Figure 16 [49].

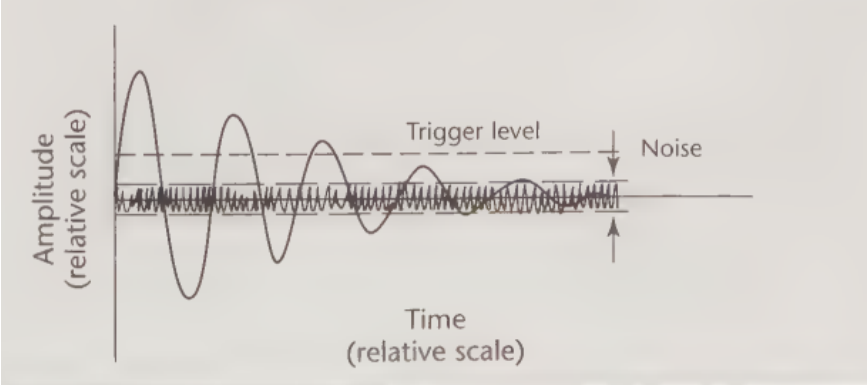

Figure 16: Noise and Threshold value (Trigger level) of an acoustic signal [49]

4.3 Signal Processing of AE Events

Once a clean signal is detected, there are several main methods of processing the data of these incoming signals and transform them in usable data for structural monitoring.

4.3.1 Damage Source Localization Method

Locating the origin of an AE event can aid in finding the location where a defect occurs and grows, which can allow for further detailed inspection. To accurately assess the location of a defect, time difference of arrival (TDOA) measurements are taken.

For simple, one-dimensional cases, at least two sensors are required to determine the location of an AE event. This gives the linear location of the defect. This is ideal for monitoring pipelines, beams and pressure vessels [74]. This method is visualized in Figure 17. However, in more realistic structures with more complex geometries, additional sensors are required for accurate localization.

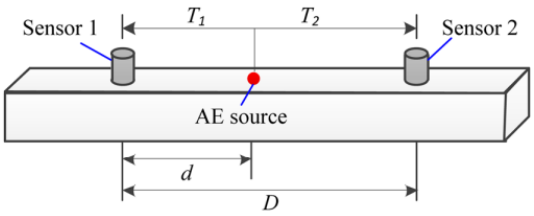

Figure 17: 2D AE source localization using two sensors [74]

For two-dimensional cases, such as flat plates, at least three sensors are required to accurately determine the location of an AE event. Through using the triangulation technique, the location of the defect emitting the signal in an isotropic material can be accurately located in a singular point [36]. The method is based on measuring the difference between arrival times. Each sensor defines it's own circle of possible defect locations based on the arrival time of the signal. The point where all circles intersect, gives the true location of the defect. This method is visualized in Figure 18. This method can be used even when the wave speed of the defect is unknown [63] or in plates made from anisotropic materials [37]. In such cases, additional mathematical adjustments must be made in order to account for the unknown wave propagation and could require additional sensors.

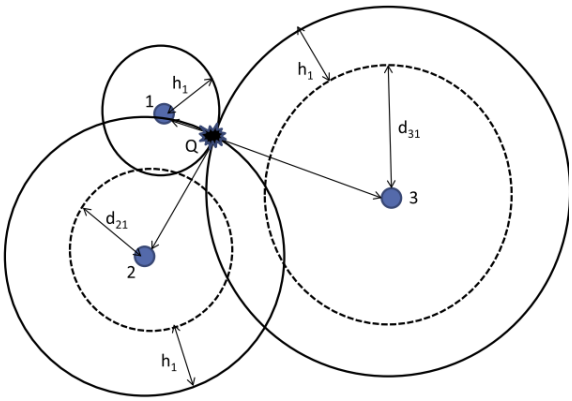

Figure 18: 3D AE source localization using two sensors[36]

4.3.2 Wave Counting Method

The Wave Counting Method uses a threshold value for a detected signal. Every instance when a signal strength crosses this threshold value, it is counted as an acoustic hit. When more hits are counted, it means more detectable acoustic events have occurred, indicating the presence of damage initiation or growth. Larger acoustic events also contain more hits per signal, allowing for the detection of larger defect occurrences based on hits measured per signal alone.

4.3.3 Cumulative Energy Method

Cumulative Energy Method does not just consider signal amplitude, but also the total signal energy. It accounts for the fact that fewer hits might indicate increase damage propagation over many hits, if these signals contain a higher acoustic energy. Larger damage events generate more energy intensive elastic waves, which are measured as acoustic wave energy.

4.4 Acoustic Emission in Adhesively Bonded Structures

4.4.1 AE in Adhesive Bonds

Despite the potential of acoustic emission monitoring, the application for adhesive bonds remains a complex and active area of study. Using localization methods, the tracking of a crack-front growing under Mode I loading has been accurately done, allowing for accurate assessment of damage growing in a composite bond [44].

It has been shown that AE can be used to identify a range of damage mechanisms within composite joints, such as matrix cracking, fiber pull-out, disbonding and cohesive failure. However, when it comes to classification of measured signals and their respective origin, challenges arise. Distinguishing between fracture mechanisms in the adhesive layer (cohesive failure) and failure occurring in the composite substrate itself is not as straightforwards, especially when both the composite matrix and adhesive are epoxy based. Their different failure modes show similar acoustic properties, making identification of failure based on their frequency content difficult [41]. This is further complicated by the nature of failure of composite joints, most often being subjected to multiple simultaneous failure modes at the same time. Further signal processing methods and interpretation of signals are to be developed, such as clustering of signals based on frequency spectrum and wavelet analysis of individual signals [68].

4.4.2 Detection of Kissing Bonds using AE

Kissing bonds are hard to detect through acoustic emission monitoring, because their complete lack of adhesion does not allow for signals to be generated to measure. As there is no bond present between the adhesive and adherend, there is nothing to break in order to generate detectable acoustic waves. The presence of kissing bonds can be confirmed using acoustic emission, based on the fact that there is this complete absence of acoustic signals. A drop in acoustic energy indicates a bad bond, while the bond is actively tested [68].

The detection of kissing bond is currently only possible while actively failing. However, the ability to detect kissing bonds preemptively with acoustic emission could lead to large developments in being able to introduce a method of certifying adhesively bonded composite parts.

5 Research Proposal

The following chapter outlines a plan for further research, based on gaps found a literature review using the background information outlined in the previous sections. Then, a research proposal is made containing the research questions, hypothesis and expected results.

5.1 Literature review

5.1.1 Acoustic Emission Testing in Literature

Prior to bonding, the specimens will have to undergo careful surface preparation to not introduce unintended contamination which might interfere with the study of sized and expected weak bonds. Shin et al. have shown that plasma etching is effective at achieving strong bonds [67]. Ma et al. discussed how plasma etching is preferred over conventional methods of surface preparation, which often can be environmentally harmful and require difficult processing conditions [43]. Plasma etching offers a more sustainable approach, which also allows for precise control of the surface preparation and activation of functional surface groups. Recent studies by Teixeira et al. [68] and Lima et al. [41] show the effectiveness of UV / Ozone surface preparation which is also preferable over chemical methods for the same aforementioned reasons. This method resulted in strong bonding of AF163-2k epoxy adhesive to carbon fiber material in both studies.

Lima et al. also showed the effect of the lay-up used for specimens on the failure of bonded composite DCB joints [40] [41]. Specimens containing all 0 degree fibers in the loading direction showed full cohesive failure, whereas other lay-ups showed delamination and other forms of adherend failure, which are undesirable when studying adhesive-interface interactions due to the presence of kissing bonds. Kupski et al. [38] showed lap-shear specimens failing cohesively when 0 degree plies were in contact with the adhesive, whereas higher degree plies in contact with the adhesive showed failure in the composite material. A stiffer adherend also showed a decrease in peel stresses at the adhesive layer, again causing cohesive failure instead of adhesive failure. Research suggests that when trying to study cohesive and adhesive failure of weak bonds, a lay-up which has increased bending stiffness and plies in the 0-degree orientation are preferred over complex or quasi-isotropic laminates.

5.1.2 Preemptive Detection of Kissing Bonds

The vast majority of research attempts to detect kissing bonds using acoustic emission detects, while the kissing bonds are actively failing. For a SHM system, this would not be sufficient as damage is detected too late, and damage reaching a kissing bond is susceptible to sudden failure. More desirable would be a measurement system that can preemptively detect a damaged bond in the early stages. Teixeira et al. [68] detected a decrease in strength of the bond and a decrease in AE energy while actively testing the weakly bonded area. However, a scattering in the measured signal broadband was noted. This scattering, which showed additional higher frequency components for low energy signals in contaminated specimens when compared to specimens with perfect bonding, could act as an early warning indicating the present of a weak bond.

The authors of the paper indicate the same, however the cause of this scattering effect is inconclusive as of yet. The authors express the need for further testing, using different contamination sizes and types to further determine the cause of the scattering effect and what parameters dictate the amount

of scattering. The scattering effect, if reproducible, is likely to originate from one of two sources.

Theory 1: The signal, which originates at the crack tip, travels through the medium. The medium, which contains a contamination, disperses or disrupts the signal. Wave mechanics, such as constructive or destructive interference, coalescence and complex harmonic interactions could result in higher frequencies. Such mechanics could take place when the wave, traveling through a contaminated medium, encounters areas with weak cohesion. An representation of the system is shown in Figure 19.

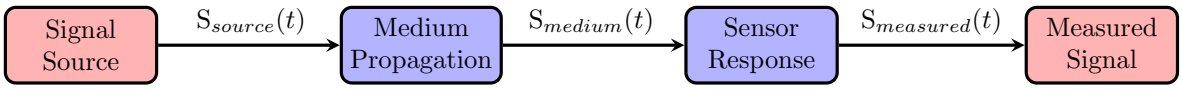

Figure 19: Flowchart showing the signal transformation in an acoustic emission system, from source to measured signal.

The signal, originating at the crack tip, becomes scattered by traveling through the medium. Here, $S_{measured}(t)$ would already have the scattering present in its broadband, with the sensor slightly affecting the signal before the signal can be analyzed, being $S_{measured}(t)$.

Theory 2: the weak bond can not be responsible for creating higher frequency signals through unknown interactions with the traveling wave and the weak bond. Instead of the signal being scattered by traveling through the medium, the new frequencies seen in the measured signal are a result of a completely different failure mode.

Instead of failure occurring at the crack tip and scattering in the medium, failure occurs at the weak bond in the medium itself. Such failure could be interfacial effects or failure in the transition region between the weak bond and the surrounded correctly bonded interface. In this case, the source of the signal originates at the defect, instead of traveling through the medium. Here, the source signal would already contain the higher frequency scattering components.

This second theory is mainly introduced, seeing as the effects a weak bond has on wave interactions is as of yet unknown. The higher frequencies are also similar to the frequency range indicating fiber breaking, identified by Lima et al. [41]. A possibility would be fiber breaking or similar failure occurring at the weak bond before the crack tip reaches this area, causing the detectable higher frequencies.

Teixeira et al. recognize in their paper that further research is needed to study this scattering effect in order to determine what causes it and which parameters determine the amount or frequencies of the scatter. One such method would be to compare the scatter of testing specimens containing various contamination, such as kissing bonds of various shapes and sizes. This thesis will attempt to study this research gap, by trying to use this method of analyzing acoustic wave frequencies for different types of kissing bond sizes.

5.2 Research Objectives

The objective of this research is to study the use of Acoustic Emission (AE) techniques to preemptively detect kissing bond defects in adhesively bonded structures. The study aims to investigate findings by Teixeira et al. on the high-frequency scattering of acoustic signals as a potential early

detection method for kissing bonds. Additionally, characterization of acoustic wave features and induced failure modes caused by artificial defects will be studied, along with the effect of defect types on fracture resistance of the bond.

The objective of this study is to try and detect kissing bonds in adhesively bonded composite structures using acoustic emission. Kissing bonds of various shapes and sizes will be tested, along with pristine bonds containing no weak bonds in order to compare the acoustic measurements. Initially, the weak bonds shall be identified based on the number of acoustic hits and acoustic energy measured. A variation in defect or damage type or size is expected to result in a difference in acoustic data measured while destructively testing the bond [68].

During the same tests, the signals which initially traveled through the medium containing kissing bonds are also measured. Differences in the scatter of this signal are attempted to be related to the size and shape of the kissing bonds. If successful, this could be seen as an early detection method for detecting kissing bonds in bonded joints using acoustic emission, something that is yet to be consistently done in research.

Finally, using the acoustic data and the force displacement data obtained from mechanical testing, an estimate of the Fracture Toughness G_{1c} of the bond will be established, attempting to correlate acoustic energy measured and the elastic energy released during the failure of the bond. If successful, this would allow for an estimation of the fracture toughness of a bonded joint containing kissing bonds, before a propagating crack would reach a contaminated area.

5.3 Research Hypothesis

The following hypothesis have been established based on findings in literature and the aforementioned research objectives:

Hypothesis 1: Kissing bonds and other defect types can be detected by analyses of the acoustic signals monitored during destructive testing of the bond.

Hypothesis 2: High-frequency scattering of the acoustic signals varies with defect size or type and can be used for preemptive detection of bond defects.

Hypothesis 3: No correlation is found between signal scattering and defect type or size, suggesting that scattering is unrelated to interfacial defects and are related to a different acoustic phenomenon.

5.4 Expected Results and Impact

This study attempts to further the research done on acoustic emission testing for adhesive bonds containing artificial defects. While a primary objective of this study is to attempt to observe the high frequency scattering effect seen in research done by Teixeira et al., it remains to be seen if this phenomenon is reproducible or measurable. A possible observation could be that the reported effect is unrelated to defect size and type but rather originates from other acoustic interactions.

Due to this uncertainty, the research also attempts to more broadly define bondline characteristics using of AE parameters. Defective specimens are expected to produce fewer acoustic signals and a lower cumulative energy. The a reduced fracture toughness could be related to these parameters, serving as a method of estimating bond strength based on detected acoustic signals.

Findings of this research could further the development of an AE-based monitoring system which can be used for the detection of defective bondlines. Such a system could act as an early warning detection of compromised bonds in structures, acting as a Structural Health Monitoring system. Weakened bonds can be detected early and inspected in more detail using other NDT methods. This would reduce the total area that has to be inspected to ones where a damaged bond is present, greatly reducing inspection cost. Furthermore, an NDT method able to detect weak bond has potential to further the development of a standardized, reliable and replicable NDT method for certifying adhesive bonds in aircraft structures.

5.5 Summary of Research Scope

The key areas of research are to explore the effectiveness of using NDT methods for detection of defects in adhesive bonds in aerospace structures. An emphasis is placed on acoustic emission monitoring, evaluating the capabilities of this method and its effectiveness at identifying bond defects and subsequent failure modes.

Test specimens are to be manufactured containing artificial defects in the adhesive interface. These are produced using different surface preparation methods and types of contamination. Test samples containing no defects will act as a control, referred to as pristine specimens.The experimental part of research will analyze bond performance through mechanical testing, followed by an analysis of the acoustic emission signals.

The research intends to place emphasis on surface preparation techniques and contamination types, both of which will be analyzed to determine their effect on adhesion. Results from the subsequent study are meant to further the development of reliable inspection methods and to improve the certification procedure for adhesively bonded joints in aerospace structures.The following chapter outlines the manufacturing, testing and measurement procedures taken to achieve the desired research objectives.

6 Methodology

6.1 General Methodology

The specimens are made of Carbon Fiber composite, bonded by using an epoxy based adhesive. These are chosen as the most relevant materials to use in order to represent modernly bonded aerospace structures. The CFRP material is to be a Unidirectional Carbon Fiber. For this research, the 2510 Prepreg System by Toray was provided. The adhesive will be AF163-2K epoxy based film adhesive by 3M, due to its availability and its prevalence use in modern day aircraft structure [24].

Several defect types will be introduced in the adherend adhesive interface. In order to simulate a kissing bond, artificial kissing bonds will be created by applying release agents on specific areas between the adhesive and adherend interface. Release agent contamination prevents the formation of chemical bonds and is highly detrimental for bond strength. The contamination agent will be Marbocote 227-CEE, which has shown to successfully recreate kissing bonds in similar research [68] [46]. Inclusion type defects will be added, such as protective film, adhesive contaminated with dust or sand and adhesive sprayed with misted water prior to bonding.

The defects will be applied using 3D printed or aluminium sheetmetal templates, allowing for accurate sizing and positioning of the defected areas. An example of the contamination sizes can be seen in Figure 20.

Figure 20: Specimen Defect Types

The surface of the adherend material will be treated using plasma surface treatment. Ma et al. [43] show that conventual methods of surface preparation, such as minimal abrasion and cleaning using solvents, can have limited effectiveness. Additionally, the process can be environmentally harmful and require difficult processing conditions. Plasma etching offers a sustainable approach and allows for precise control of surface properties and activation.

Shear forces in bonded joints are the most prevalent load case in bonded aircraft structures. It would therefore be sensible to test adhesive bonds under lap-shear according to ASTM standards. Single-lap joints however show high peel stresses due to misalignment of forces, causing secondary bending of the sample. These peel stresses result in the bonded area not failing in shear, but causes

a peeling failure. This stress distribution is represented in Figure 21.

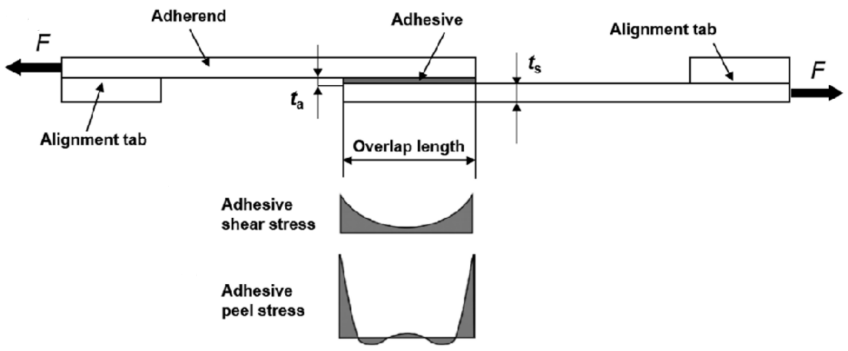

Figure 21: High Peel Stresses in Adhesive Bondlines [7]

Samples tested under lap shear conditions often end in fast, catastrophic failure. The failure occurs too rapid and the failure itself is complex, making it difficult to extract any useful data when using acoustic emission monitoring. Additionally, because of the chaotic nature of such failure, it is hard to pinpoint which signals belong to adherend failure of the composite or failure within the adhesive layer. Additionally, composite matrix failure and adhesive failure share similar acoustic frequencies, making them hard to distinguish under such failure conditions [41].

DCB testing of bonded joints is prevalent in research, as the predictable behavior of the specimen allows for careful control of the failure. This ensures that the desired acoustic signals can be captured and related to the failure being induced at that given time. Similarly, DCB testing allows for the failure to be controlled such that it will most likely occur in the adhesive, being either cohesive failure for a well-bonded region and adhesive failure for a artificial kissing bond [68].

Due to the presented difficulties of lap-shear testing, it was decided to perform mechanical testing using the more controllable DCB testing method. The samples in this research will be tested in accordance with ASTM D 5528-13 [5]. This testing analyses the Mode 1 fracture toughness G_{1c} of the adhesive bond. A linear load increase is expected, followed by gradual failure of the adhesive layer and declining force [11] [68]. It is expected that the estimated fracture toughness G_{1c} from forced-displacement data will show a variation of 20% or even higher [10]. Testing will be conducted at 4 [mm/min] in accordance with the lower limit of the ASTM standard in order to capture singular failure events instead of capturing multiple waveforms from more rapid failure [11].

6.2 Specimen Design

The composite layup of the sample adherends is chosen to be $[0]_8$. The high stiffness from multiple low angle fiber orientations is shown to promote cohesive failure of the adhesive, rather then undesired failure of the adherend material [38] [68] [41]. The specimens are made 25mm wide in accordance with the ASTM 5528-13 standard [5]. The design of the specimen can be found in Figure 22:

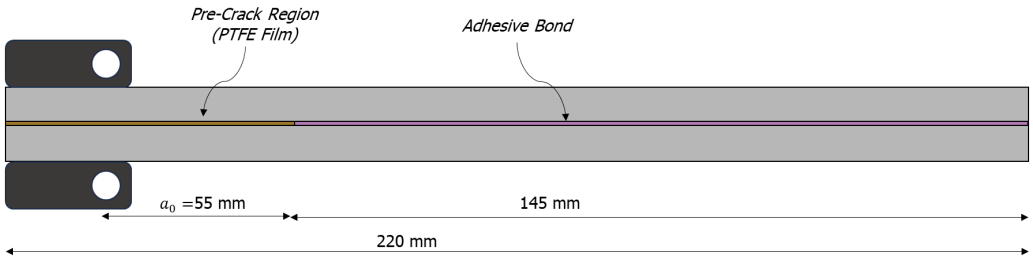

Figure 22: DCB Specimen Geometry

Loading blocks are attached to the end of the specimen to apply the peeling force. A pre-crack is inserted using PTFE tape, which is 75 [mm] in length. The pre-crack is made to match the thickness of the adhesive as closely as possible, where one layer of adhesive film is 0.24 [mm] thick. The total length of the specimen in 220 [mm], as a longer specimen will allow for a larger area to be measured. A long specimen also minimizes the effects of edge-reflections of acoustic waves, which can hinder interpretation of the measured signals causing reflections to be considered as failure events.

Additionally, the longer distance allows the wave modes of the waveform to separate as a result of dispersion [11]. Attenuation tests will be conducted to ensure attenuation of signal is not too severe. If attenuation is too high, signals will be damped out due to the material before being measured, leading to acoustic events remaining undetected. After production, specimens will be individually scanned using C-Scan after manufacturing to verify the correct application of artificial defects.

6.3 Acoustic Emission Analysis

For the Acoustic measurements, a wideband AE sensor will be used in order to capture the desired signals. The signals are expected to range between 20-1200 [kHz] as can be seen in recent research [68] [41]. This frequency range is also applicable for most acoustic emission tests in industry [49]. An amplifier of 34 [dB] is used to amplify the obtained signals. The Data Acquisition software used will be AMSY-6 by Vallen Systeme. The data sampling rate is 10 [MHz]. The sensor used is a single piezoelectric sensor of the type VS900-M.

The acoustic parameters to be measured is the total acoustic energy released and the number of acoustic hits measured that exceed a threshold amplitude of 40 [dB], which is the approximate threshold were environmental noise can interfere with the detection of signals. This acoustic data will be used to validate that the kissing bonds have been properly introduced in the bond interface, where completely disbonded areas should show no acoustic activity and partially disbonded area show a significant reduction in number of acoustic hits and total acoustic energy released [68].

6.4 Signal Processing

In order to detect the scattering phenomena as outlined in Teixeira et al., Wavelet Transforms will be performed on isolated acoustic wave signals. Specimens containing no artificial weak bond should show a signal with frequencies contained between 100 and 200 [kHz]. Specimens containing artificial weak bonds should show a frequency scatter, expected in the 300 to 600 [kHz] range.

Additionally, Fast Fourier Transforms can be used to quantify dominant frequency ranges. While they do not give insight in when frequency scatter may occur in the signal itself, their presence and quantity might be of insight when attempting to quantify the scatter. A quantifiable scatter could then be related to the before-mentioned fracture toughness and other AE parameters such as emitted AE hits and cumulative energy.

7 Specimen Production

This chapter will provide an overview of the production process of the test specimens and the detectability of added defects in the adherend/adhesive interface using conventional C-Scan methods.

A total of 26 specimens were manufactured. Due to the quantity of specimens. Multiple production iterations were needed in order to achieve specimens of sufficient quality for testing. Careful considerations were made to ensure that the production process and curing cycles would remain as consistent as possible. This was done to reduce variability of the results. Alterations of uncertainties introduced from the production process will be further discussed.

7.1 Carbon Fiber Adherend Material

The composite material provided for production of the composite adherend was 2510 Prepreg System Unidirectional carbon fiber by Toray. The chosen lay-up configuration was chosen to be $[0]_8$, as this fiber-orientation is shown to result in less adherend failure in the studied literature [41] [38].

It must be stated prior to detailing the production process that the composite provided had an estimated shelf life lasting to the end of 2018, as was noted on the provided paperwork. Next to being out-of-date, it is also uncertain if the composite was stored correctly during this time. Composite plates made from this material during the early stages of research showed large voids or resin-rich areas according to early C-Scans of the composite. This would not only affect the structural strength of the adherend, but would also make it hard to distinguish between specimens contaminated with artificial defects, and defects present in the composite material itself. Therefore, some alterations were made to the composite production and curing process. This includes excessive debulking stages to reduce voids and moisture content in the prepreg, as well as added dwell stages in the curing cycle to improve the quality of the carbon.

7.2 C-Scan of Composite Material

7.2.1 C-Scan Properties

A Olympus Epoch 650 C-Scan was used in order to scan the composite plates after curing. The sensors used were 5 [MHz] V309 Olympus transducers. The material is scanned while submerged in a water bath, where the C-Scan measures the increased reduction in the transmitted signal, compared to the impedance of the water itself. Prior to each scan, the system was calibrated to the water to create a baseline for the through-amplitude of the signal. As a reference, it can be assumed that high impedance detected by the C-Scan are due to trapped air of voids in the material. Additional C-Scan parameters can be found in Table 8.

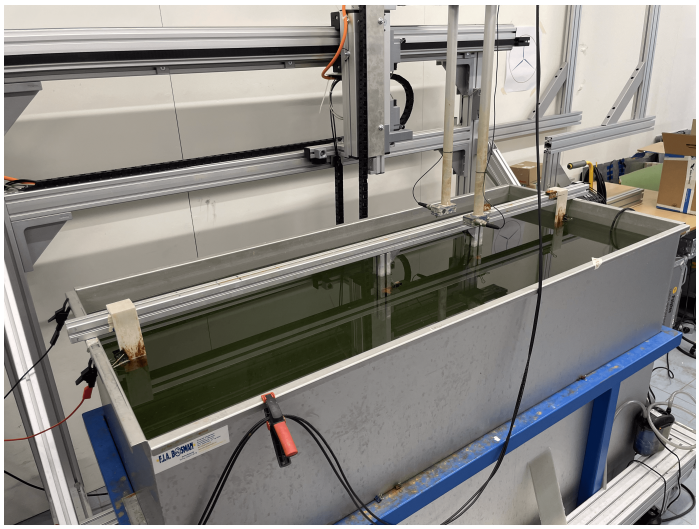

Figure 23: Ultrasonic C-Scan (Immersion)

Table 8: Acquisition Parameters for C-Scan.

C-Scan Parameters	**Value**
Sensor Frequency	5 MHz
C-Scan Frequency filter	1.5 - 8 MHz
Noise filter	10%
Baseline signal amplitude	80 dB
Scan speed	100 mm/s

7.3 Production of Carbon Material

First, an aluminium plate was cleaned using isopropanol. The plate was then treated with layers of Marbocote 227-CEE Release Agent, where 3 coats were applied in total. 5 minutes of drying time was allocated in between coats, where after applying the last coat the release agent was left to dry for an additional 15 minutes. A layer of non perforated release film Airtech A4000R was taped to the tool to act as a base, as can be seen in Figure 24. Early test specimens showed that the surface finish provided by non perforated release film resulted in better cohesive failure modes when compared to composite directly laid up on the aluminium tool surface.

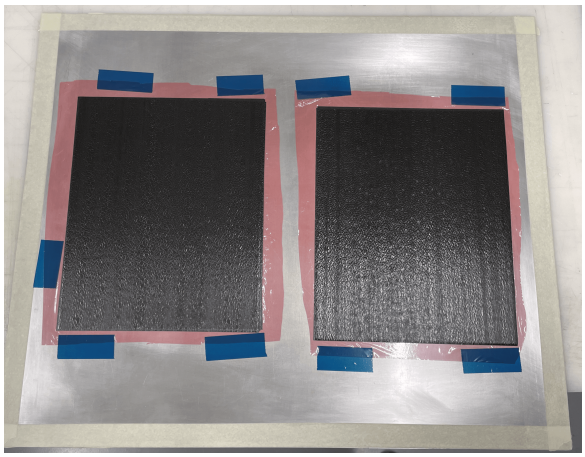

Figure 24: Composite stack placed on prepared tool with unperforated release film as a base layer

The composite material was defrosted while sealed for a minimum of 3 hours, until the composite had reached room temperature before being used. With the base provided, individual carbon sheets of 205 [mm] x 270 [mm] were cut. This size was chosen as it would provide 6 specimens per curing cycle, with 3 specimens to be produced per defect type, including cutting margins and losses. This size was also chosen as it is the largest size plate that would fit in the in-house UV/Ozone surface treatment chamber. However, this method of surface preparation was deemed insufficient and instead, Corona Plasma Surface Treatment was used.

Each layer of composite was laid using hand-layup. In between each layer of composite, a 5 minute debulking stage was applied to the composite stack using a debulking table. This subjected the composite stack to a ambient pressure of 100 [mbar], which aids in consolidation of the material and is effective at reducing voids and removing excess moisture. After the final composite layer, the entire stack was covered in peel ply, which acts as air pathway material. A second layer of non perforated release film was applied to cover the composite plates in order to constrain the vacuum from only pulling along the edges of the plate instead of along the thickness direction. Finally, the stack was covered with additional peel ply and breather material. This entire layup is vacuum bagged, sealed at the edges using LTS90B Sealant tape.

Throughout the hand-layup and preparation process, gloves were used appropriately and additional handling precautions were used to minimize the likelihood of introducing contamination unintentionally to the composite adherend. This is especially noteworthy since the research's aim is to detect artificial defects. By doing this, the likelihood of false positives detected during nondestructive measurements, or early material of bond failure during mechanical testing can be reduced.

Initial scans of the composite produced with the manufacturers curing cycle showed clear indications of imperfections in the material and overall poor quality. A scan of one of the first production iterations can be seen below in Figure 25. Here, a low reduction in [dB] indicates good transmission. The surrounding water has the lowest impedance, which is the blue region surrounding the scanned plate. Green and yellow signify minor impedance, whereas orange, red and black signify higher impedance, likely due to embedded imperfections such as resin rich areas or trapped air.

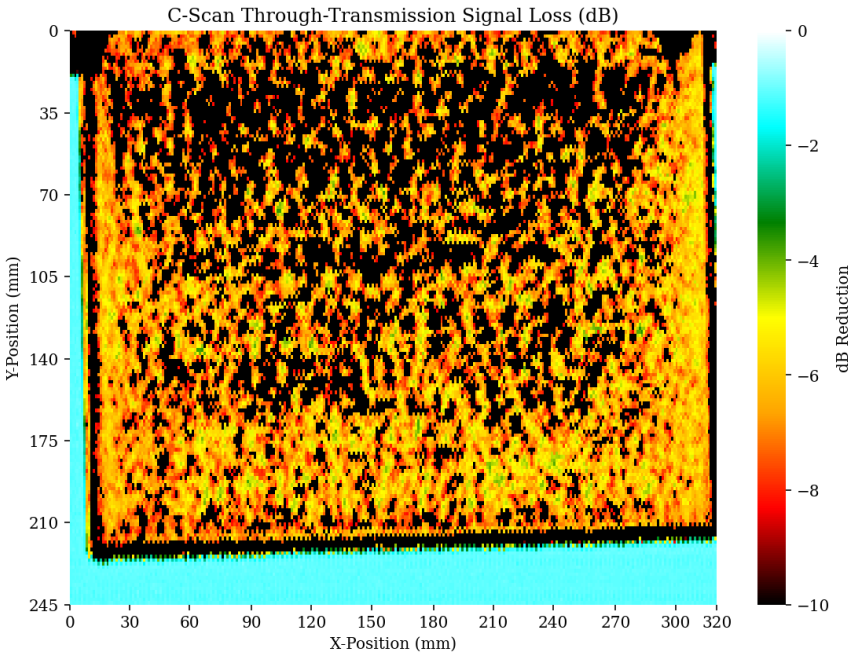

Figure 25: C-Scan of Composite Plate at Initial Manufacturing Stage

As a first step to improve on the quality of the outdated carbon, a additional debulking stage was applied. This was meant to reduce moisture which the composite likely absorbed during storage and to also reduce the likelihood of voids present in the material. As a test, two plates were subjected to a debulking stage of 3 hours and 18 hours respectively. This debulking step was conducted after vacuum bagging, meaning the entire plate was debulked. The different resulting C-Scans of this design iteration can be seen in Figure 26.

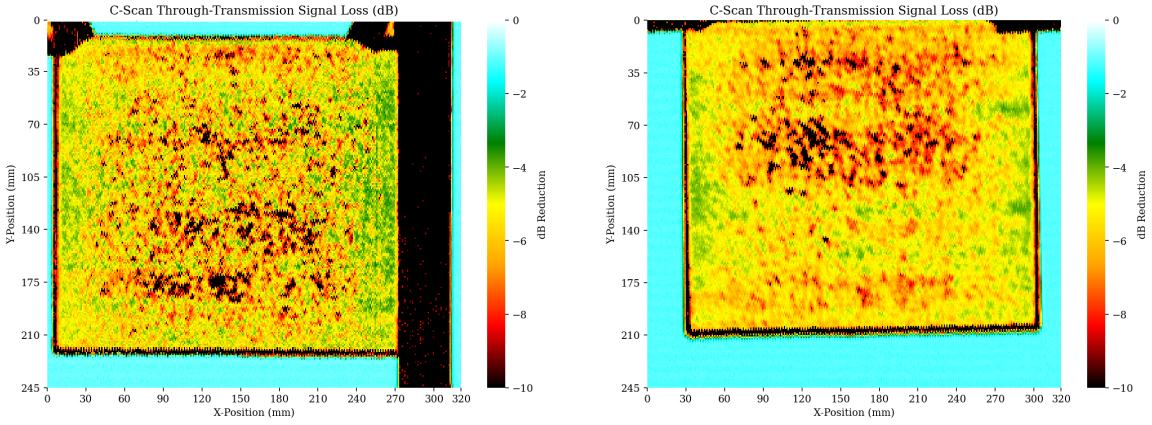

(a) Carbon 3 Hour Debulk

(b) Carbon 18 Hour Debulk

Figure 26: Comparison of C-Scan dB Reduction: 3H vs 18H Debulked Carbon Composites

As can be seen, the 18 hour debulk did result in noticeably fewer voids, being concentrated towards one top half of the plate. It was thereafter chosen to keep the 18 hour debulk cycle for future production runs. To further aid in moisture removal, the next production iteration had an 18 hour debulk heated at 40°C instead of room temperature. The result of this change can be found in Figure 27.

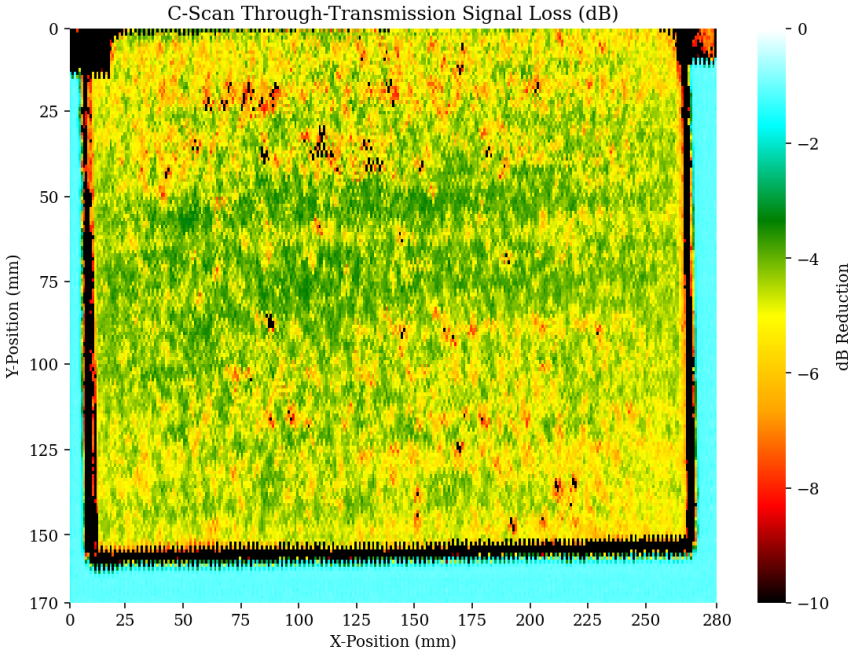

Figure 27: Carbon 18 Hour Heated Debulk

As can be seen, quality was further improved leading to less voids and overall signal impedance, indicated by the decrease in dB being blocked by the material. This is especially noticeable by the green area in the middle of the material. This further reinforced the theory that the composite material had absorbed moisture over time which should be minimized for all production iterations.

An additional dwelling period of 113°C at 30 minutes was done to further reduce the negative effects of the moisture content. At this temperature, minimal resin viscosity occurs.This does make the curing cycle deviate from the specified curing cycle in the material data sheet. However, the C-Scans of the composite material showed a great improvement in resin area distribution and the complete elimination of large voids when this additional dwelling stage was introduced. These results can be found in Figure 28.

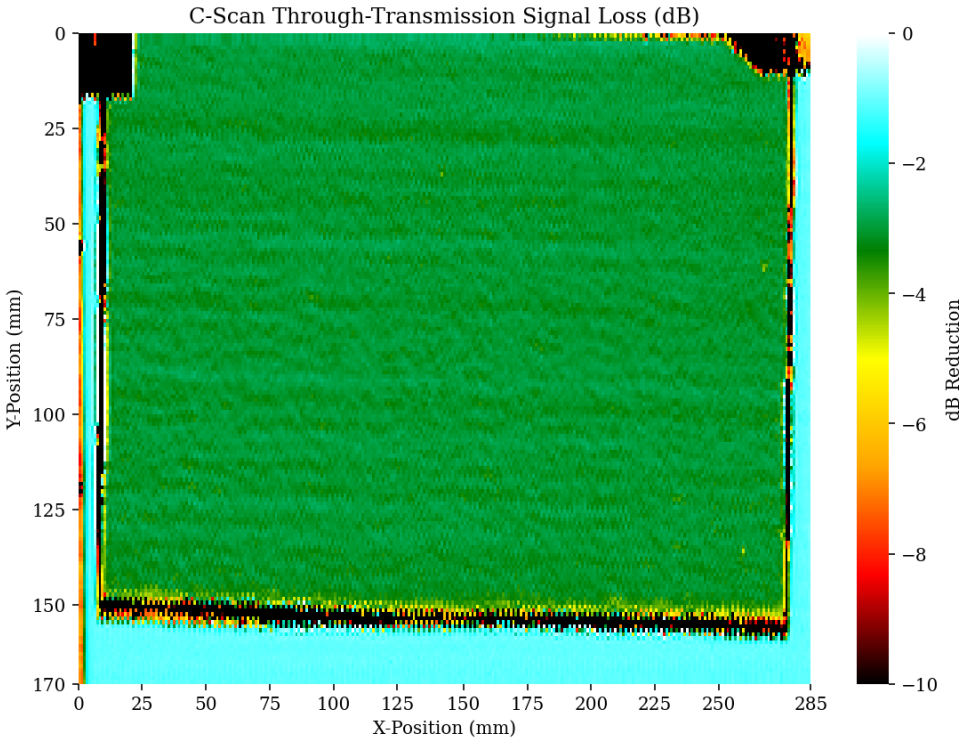

Figure 28: Carbon 18 Hour Heated Debulk - Added Dwell Stage

Several more production iterations were done to achieve this final product, including changing the lay-up procedure. This included switching release films types, changing the order of peel-ply and release films, using just peel ply and more. Once the quality of Figure 28 was achieved, a final production procedure was chosen, as previously described in subsection 7.3.

The carbon fiber prepreg, specifically meant for out-of-autoclave curing, was oven-cured under full vacuum. The recommended curing cycle as per the manufacturers specification is shown in Figure 29.

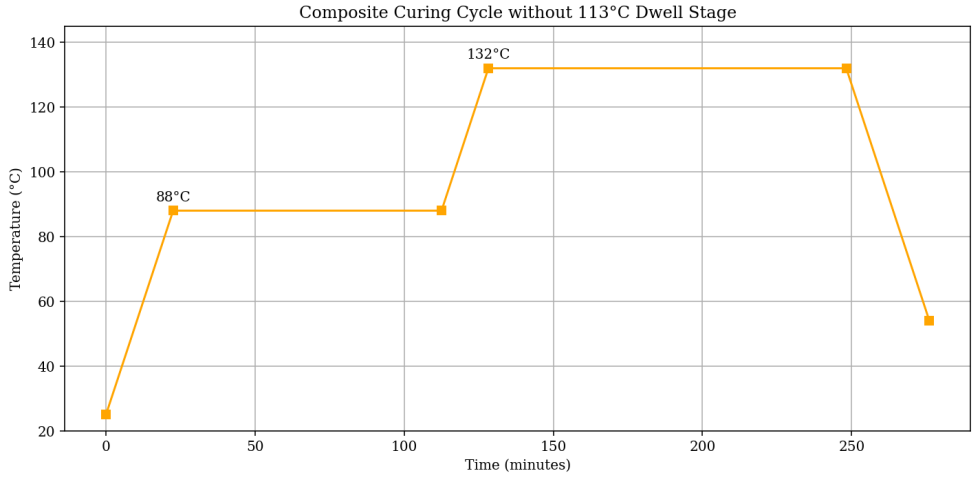

Figure 29: Curing Cycle as per Specifications

- Ramp to 88°C at 1.5°C/min. Hold for 90 minutes.
- Ramp to 132°C at 1.5°C/min. Hold for 120 minutes.
- Cool down to at minimum 54°C at 1.5°C/min.

The curing cycle chosen to improve the quality of this specific batch of material can be seen in Figure 30.

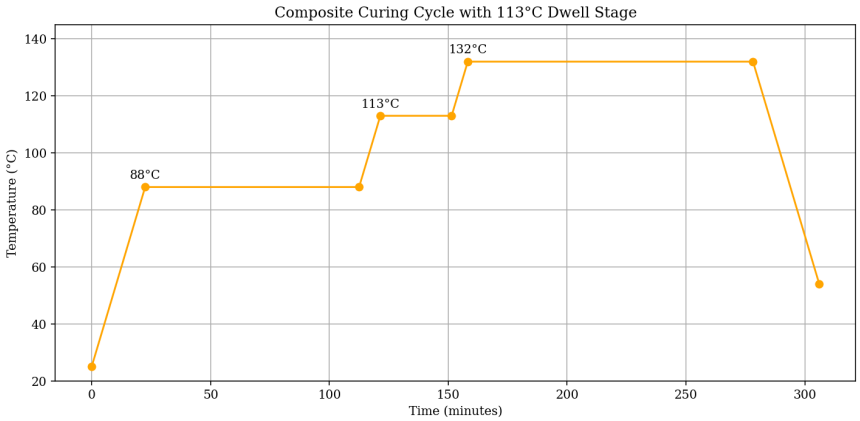

Figure 30: Alternative Curing Cycle with Added Dwell Stage

- Ramp to 88°C at 1.5°C/min. Hold for 90 minutes.
- Ramp to 113°C at 1.5°C/min. Hold for 30 minutes.
- Ramp to 132°C at 1.5°C/min. Hold for 120 minutes.
- Cool down to at minimum 54°C at 1.5°C/min.

7.4 Adhesive Material

The adhesive used is AF 163-2k structural adhesive film by 3M. The adhesive is epoxy based containing a glass fiber adhesive carrier, ensuring a more consistent adhesive thickness by reducing squeeze-out during the curing process. This is especially beneficial when curing under positive pressure.

7.4.1 Production

Prior to adhering, the adhesive is left to thaw sealed for 3 hours. Additionally, to ensure that the carbon adherend is dry it is oven dried at 40 °C during this time. The composite is lightly sanded using 400 grit sand paper. During sanding, light strokes are made in a criss-cross pattern. After sanding, the surface is cleaned with HYSO QD to remove contaminants and degrease the surface, followed by a final cleaning wipe using Isopropanol. After cleaning, the surface is activated using a T-JET Corona Plasma Etcher by TIGRES GmbH. The nozzle is placed 25 [mm] from the treated surface. The speed of etching is set to 10 [mm/s], with the step size in between passes set to 8 [mm]. Immediately after plasma etching, the adhesive film is placed on the treated composite surface. The film is pressed firmly and trapped air bubbles are carefully squeezed out using a plastic scraper. The time between etching and adhering should be minimized to keep the newly activated surface from reacting with the environment. As for the production of all specimens manufactured, time between these two steps was kept to less than 5 minutes.

It should be mentioned that partially through producing the final specimens, the corona plasma treatment system was disassembled, moved and reassembled. While the treatment settings were maintained, changes in nozzle distance to the surface and gas flow might have introduced slight variability in the bond performance in different specimen types.
Besides the adhesive film, reinforced Teflon foil is used as a pre-crack and is taped to the carbon adherend. This film has a thickness of 0.2 [mm], which is close to the adherend thickness of 0.24 [mm] after curing. It was therefore not needed to add further adhesive layer thickness control measures.

The carbon-adhesive-carbon stack was placed on an aluminium tool, cleaned and treated with release agent. The tool was covered with peel-ply. After placing the carbon-adhesive-carbon stack, peel-ply covered the entire stack once more. In the case of adhesive squeeze-out, the peel ply would still allow for easy removal of the cured part. Breather cloth was used to cover everything to provide for good pull of vacuum. The part was sealed with a vacuum bag and left under vacuum for 30 minutes prior to curing. This was done for the removal of air and to ensure good contact between the adhesive and composite. The vacuum also prevents the plates from moving and misalignment prior to curing of the adhesive.

The process of curing the adhesive can be found below. For AF163-2k adhesive, curing in the autoclave is recommended as the externally applied pressure improves the bonding between the adhesive and the adherend. The curing process can be found in Figure 31.

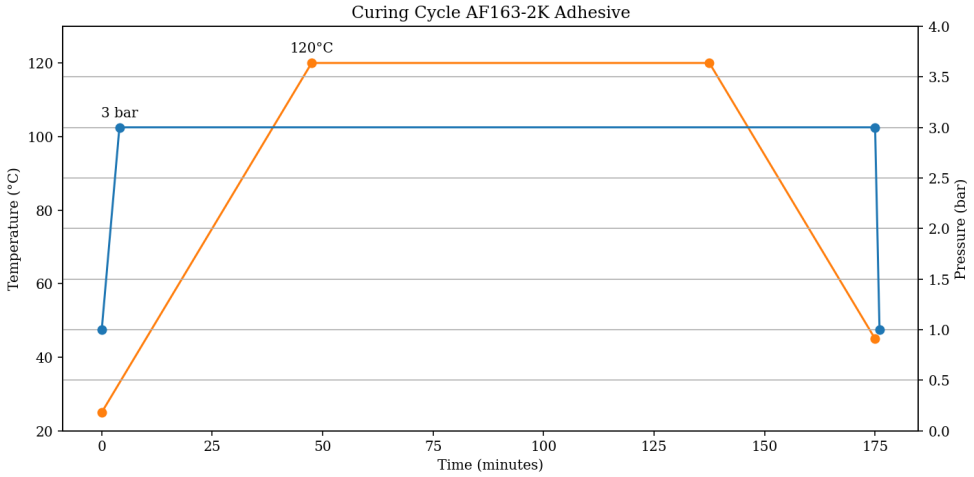

Figure 31: Curing Cycle used for Curing the Adhesive

- Ramp to 3 bar at 0.5 bar/min. Ramp to 120°C at 2°C/min. Hold for 120 minutes.
- When 3 bar is reached, vacuum is removed.
- Ramp down to 45°C at 2°C/min.
- Ramp pressure down to 1 bar at 0.5 bar/min.

7.5 Contamination

Multiple specimen types with or without different defects were fabricated. These defects types are defined using the following designations:

- **P**: Pristine Specimens, containing no artificially added defects in the bondline.
- **AC**: Specimens where adhesive protective film was left as an including over the entire width of the bondline.
- **RA-U**: Specimens where release agent was applied as a contamination over the entire width of the bondline. While plasma etched, the treated surface was uncovered.
- **RA-C**: Specimens where release agent applied identically to RA-U specimens. However, the treated surface was covered during plasma etching, providing no plasma surface treatment on the contaminated region.
- **RA-O**: Specimens were contaminated with release agent over a smaller, circular area.

Specimens including a piece of adhesive film represent the introduction of inclusions or the improper removal of protective films, which completely prevent a good bond from forming. It is expected that this type of defect should also be visible on C-Scan due to its inclusive nature.

By producing both RA-U as well as RA-C specimens, the effect of Corona Plasma Etching as a method of surface activation and cleaning can be studied. Additionally, both methods of introducing contamination made to see which produced a kissing bond type failure and which are detectable using traditional C-Scan methods. These specimens represent a contamination as a result of spillage or the result of working without clean gloves in between fabrication steps. As shown in past research, release agent can be used to create kissing bond type defects which should not be detectable on C-Scan [68].

The size of the rectangular defected area for all defects is an area 50 [mm] in length, covering the entire width of the specimen. If a kissing bond is present, complete failure of this part of the bond is to be expected. Prior to the defected area, a contamination free area of 25 [mm] in length is left for the crack to initiate and propagate to the defected area. The defect positioning and size is visualized in Figure 32. Defects are only introduced on one side of the adhesive, where the side with the defects is noted in order to be consistent during testing.

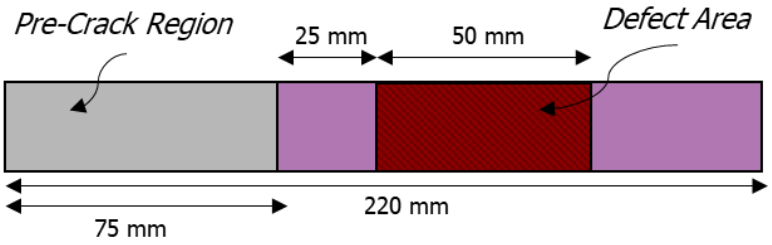

Figure 32: Defect positioning and size - full width

Additional specimens were produced with release agent as contaminants. This time however, the contamination was applied in a circular shape, leaving an uncontaminated area throughout the width. The shape and size of which can be found in Figure 33.

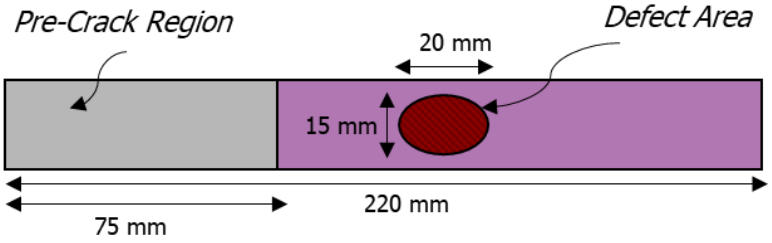

Figure 33: Defect positioning and size - circular

7.6 Production of Defects

Different types of defects were introduced in the bond-layer prior to curing. Each defect was positioned at the adhesive adherend interface. This was done to achieve bad adhesion at the contaminated regions, while still allowing good bonds to form outside the contaminated region. A total of

three specimen types are produced, being either pristine (no contamination), inclusive defect (film) or zero-volume disbond defect (release agent induced kissing bond).

7.6.1 Pristine and Adhesive Film defects (P & AC)

Both the pristine and adhesive film defects were produced from the same stack of material. The adhesive film was applied to a completely cleaned and surface treated composite. Prior to bonding the second composite plate, an area 50 [mm] x 105 [mm] of adhesive protective film was carefully cut with a razor. After removing the adhesive film, this pre-cut out area remained on the to be bonded surface. This can be seen in Figure 34, where the yellow protective film is kept on the adhesive surface. After which, the second plate of composite was adhered, leaving an area with and and area without adhesive film as added defect. From this stack, 3 specimens of each defect type could be manufactured.

Figure 34: Adhesive Carrier Film remaining on the adherend surface

7.6.2 P & AC C-Scan

The complete scan of the Pristine and AC specimens stack can be seen in Figure 35. As can be seen, there are two distinct areas. Figure 36 shows the pristine part which the P Specimens will be cut from. The area between x = 135 [mm] and x = 185 [mm] shows no visible difference in impedance to the surrounding area. In Figure 37, the inclusion of the adhesive film can be seen. The boundary is clearly visible, whereas the area contaminated with the film shows only a minor increase in impedance, evident by the slightly more yellow hue. Without the outline or consistent shape however, such inclusions might be difficult to point out using this method of C-Scan.

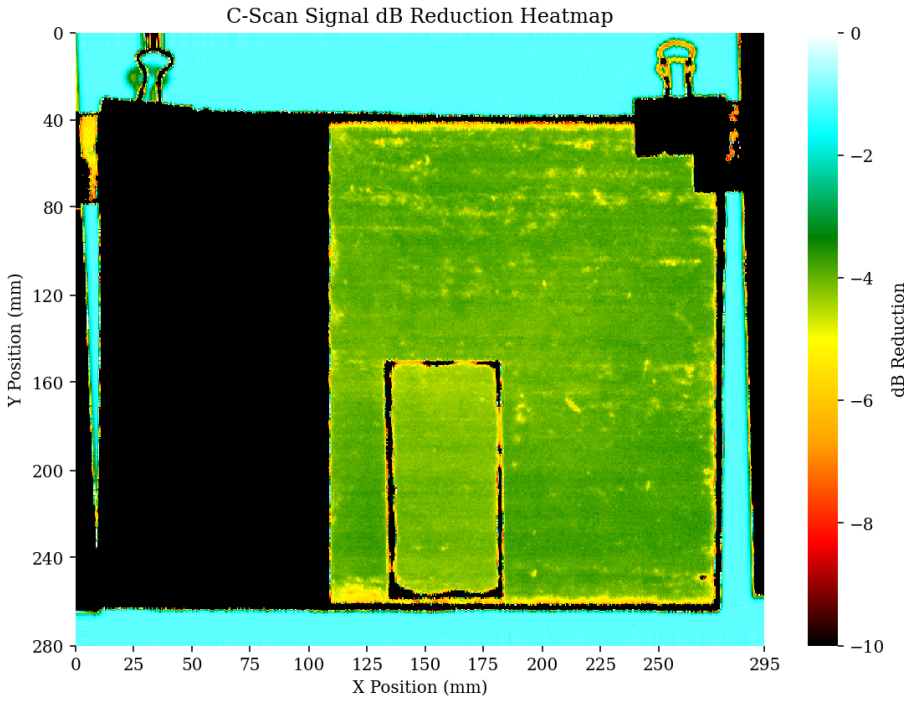

Figure 35: P & AC Specimen Stack C-Scan

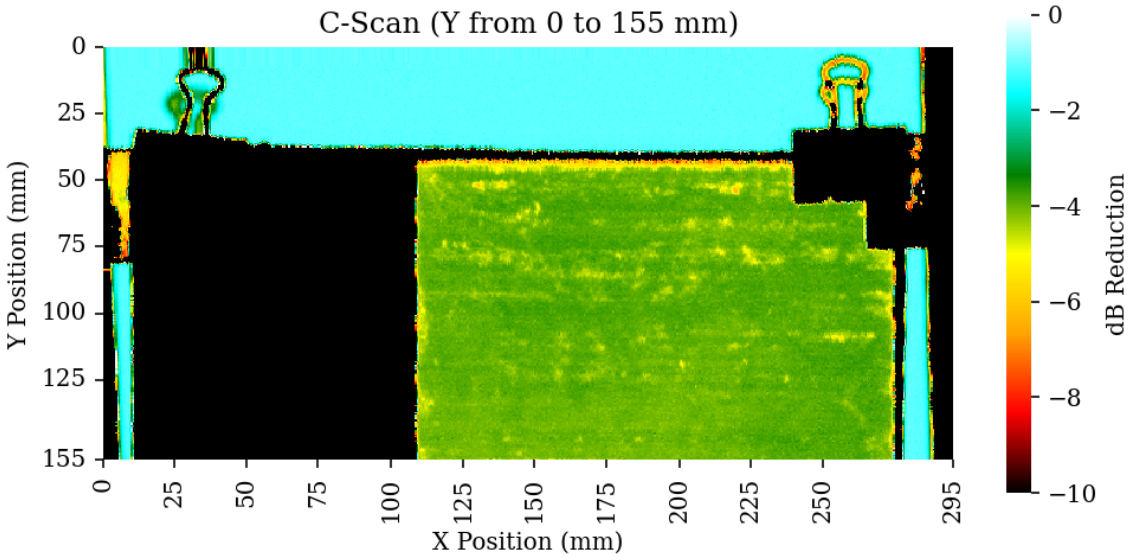

Figure 36: P Specimen Stack C-Scan

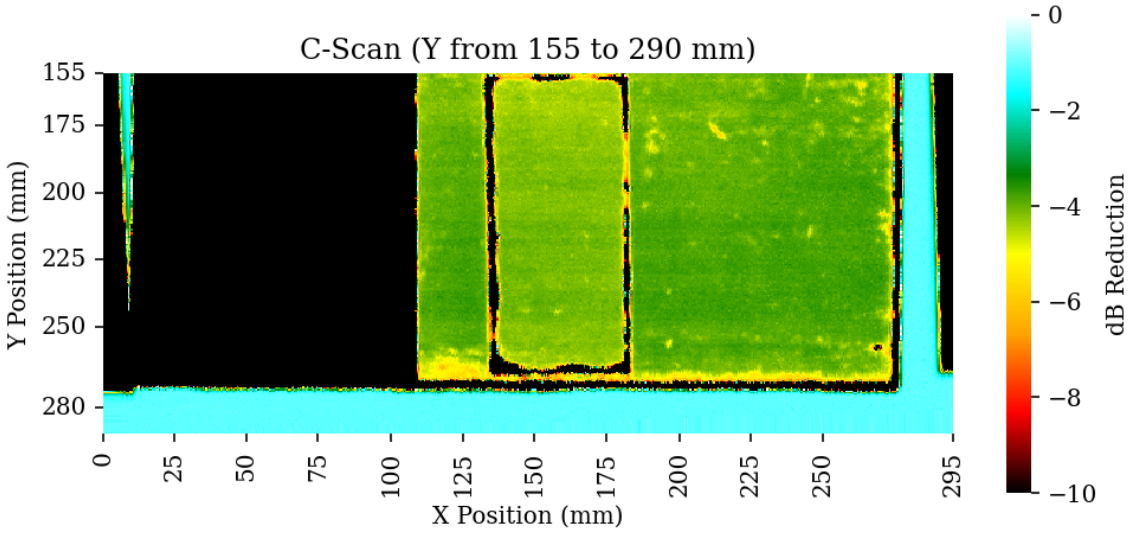

Figure 37: AC Specimen Stack C-Scan

After cutting, specimens were individually scanned to allow for a more direct comparison between defect types, as well as to visually confirm the expected contamination placement and the actual defect as per the C-Scan images. The individual specimen C-Scans can be found in Figure 38 and Figure 39.

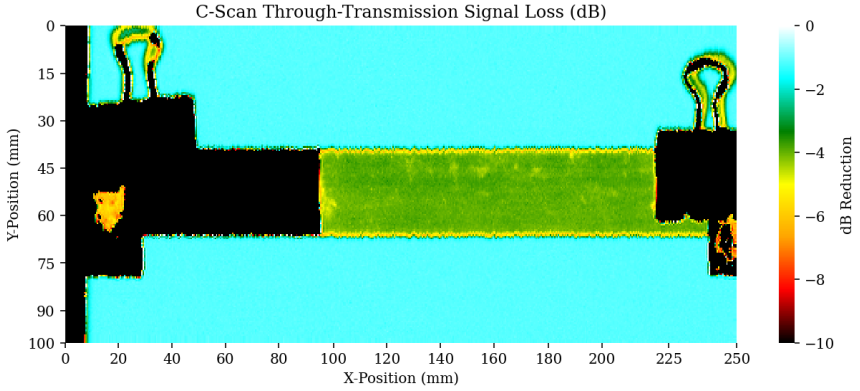

Figure 38: Singular P-Specimen C-Scan

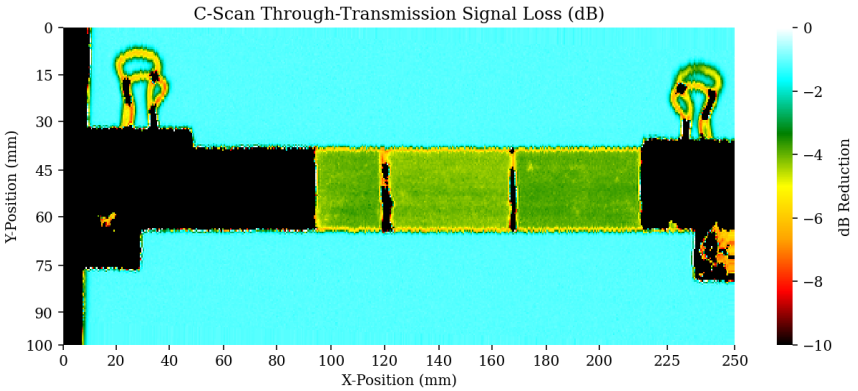

Figure 39: Singular AC Specimen C-Scan

7.6.3 Release Agent Contaminated Specimens (RA-U)

As for the specimens contaminated with Release Agent, the contamination was first applied on the composite prior to adhering. 6 layers of Marbocote 227-CEE release agent were applied, allowing for 15 minutes of drying time in between layers. This step was done after sanding and cleaning the surface, but prior to surface activation and cleaning using plasma surface treatment. A very light coat was applied in this process. Aluminium plates were used to act as a template for where the release agent would be applied, with weights used in order to keep the plates constrained and pressed down to minimize release agent spreading outside the designated contamination area.

After applying the release agent, the surface was plasma etched similar to the P and AC specimens. During plasma etching, half the area was covered using a Teflon sheet. This was done to only have half the contaminated area treated with plasma treatment, whereas the other contaminated area was shielded from this treatment. This resulted in 3 specimens treated with plasma treatment over the contaminated area and 3 without, allowing for a direct comparison showing the effects of corona plasma treatment on a surface contaminated with release agent. After surface treatment, the adhesive film was placed on the contaminated carbon plate. The stack was completed with a final, treated, uncontaminated plate on top.

7.6.4 RA C-Scan

It should be noted that while carbon plates were manufactured showing minimal defects, like shown in Figure 28, this level of quality could not consistently be replicated. Subsequent C-Scans might therefore show a more inconsistent finish, indicating some variation in material thickness, possibly from resin-rich areas due to the resin not flowing as well. For example, one of the carbon plate used for manufacturing the RA-Specimens shows the following C-Scan image which can be found in Figure 40.

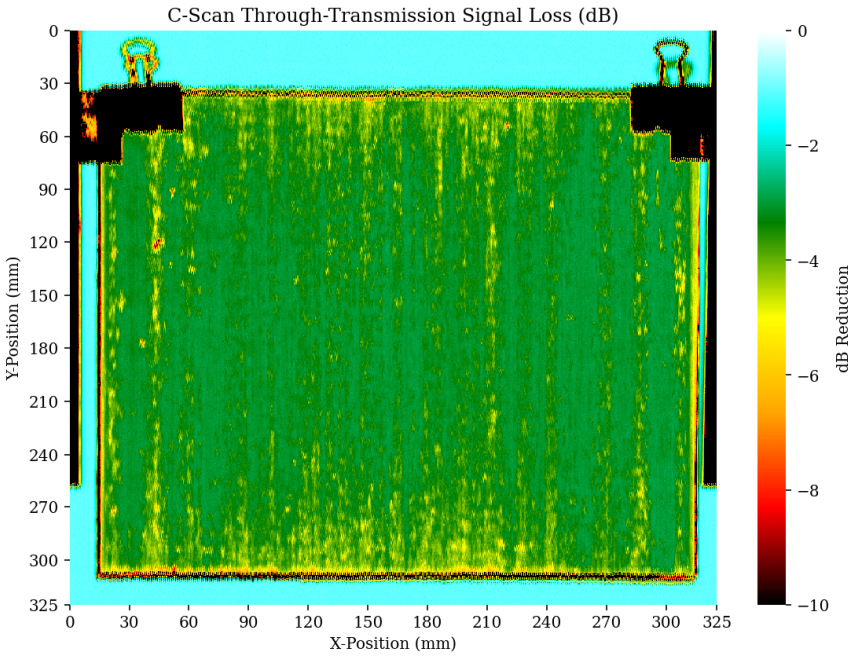

Figure 40: Carbon plate used for Release Agent (RA) Specimens

The complete C-Scan of the RA Specimens can be seen in Figure 41. As can be seen, there is a district difference between the two contaminated regions. The top area is the area covered during the surface preparation step. This area shows clear signs of contamination indicated by the higher impedance locally present where the release agent was applied. The contamination is more clearly outlined in Figure 42, where dotted lines help identify the contaminated region boundaries.

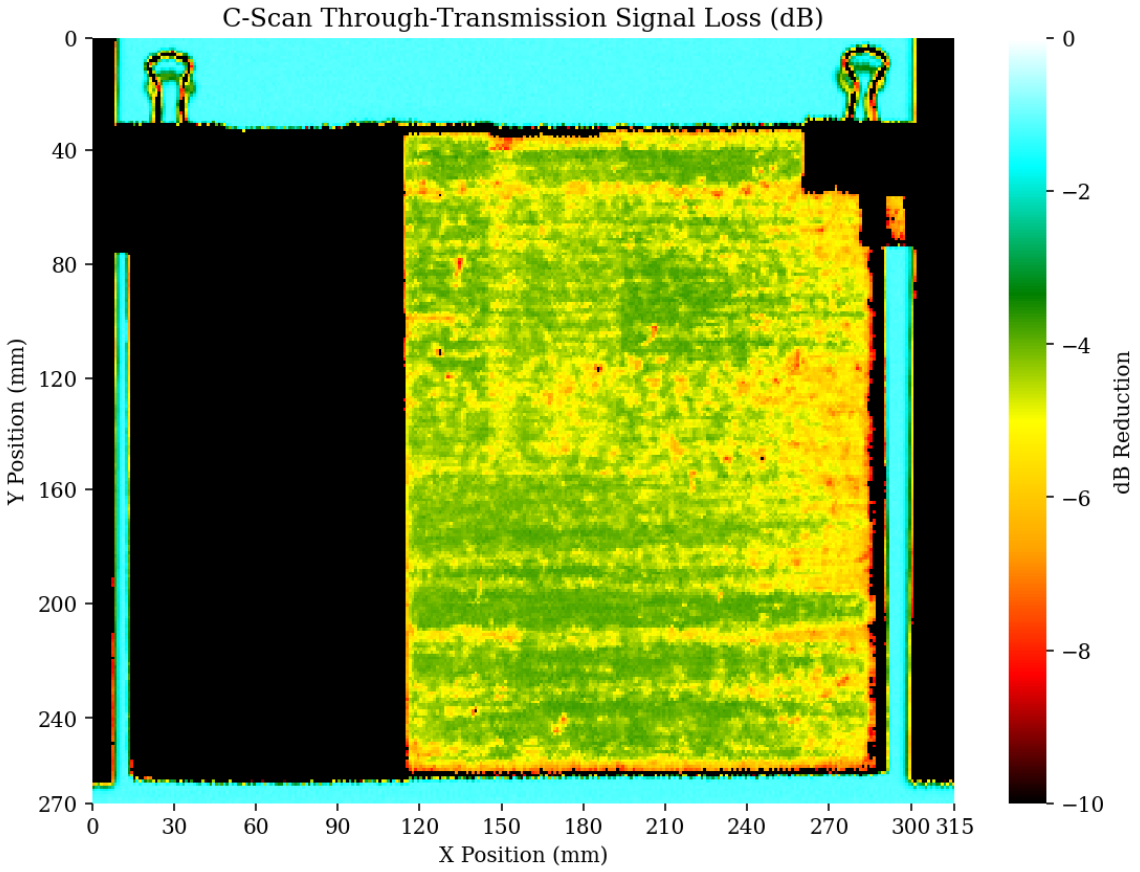

Figure 41: Release Agent Stack complete C-Scan

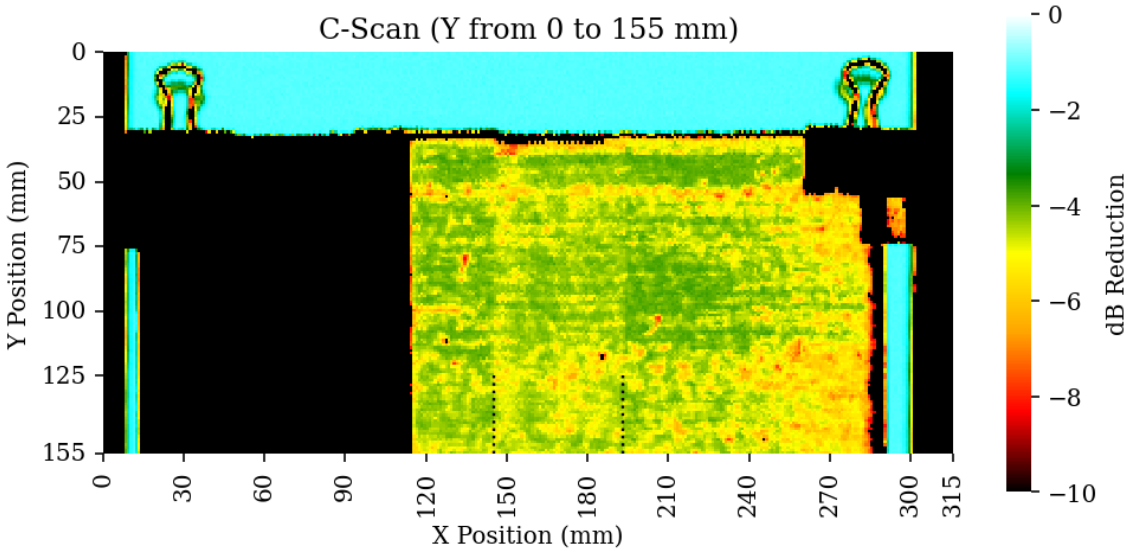

Figure 42: Release Agent Stack - Covered during Corona Plasma Treatment

In contrast, Figure 43 shows the area where the surface was surface treated after contamination was applied. No visible difference can be seen between the contaminated area and the surrounding area where no contamination was applied. This would indicate that Corona Plasma treatment is effective at breaking down the release agent, at least partially. However, the impact on the bonding strength of this area is to be determined during mechanical testing, as the release agent might still effect the local area despite being directly treated.

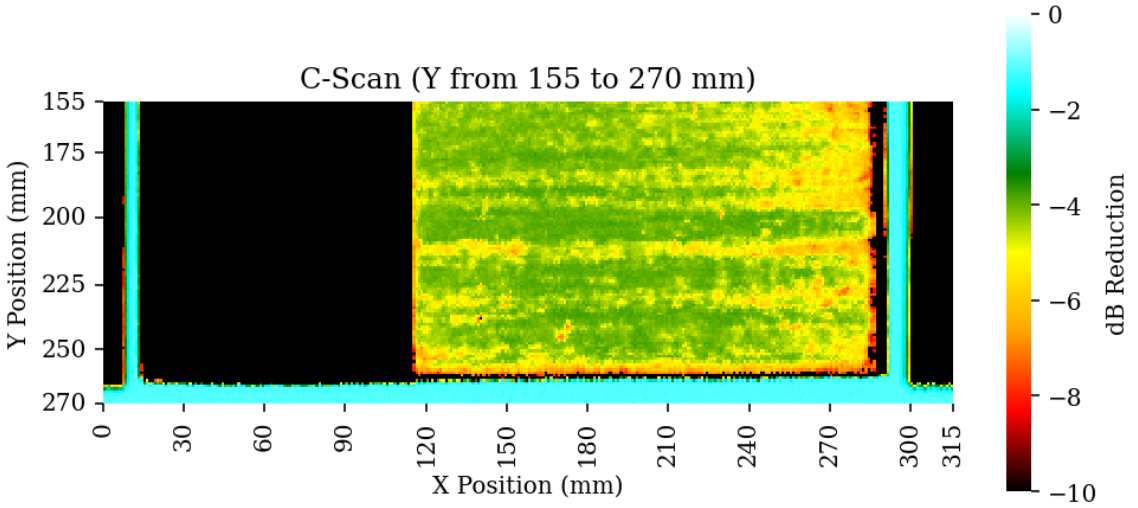

Figure 43: Release Agent Stack - Uncovered during Corona Plasma Treatment

The difference between individual specimens makes a clear distinction between the different defect types. The contaminated area can clearly be seen in Figure 44 compared to Figure 45.

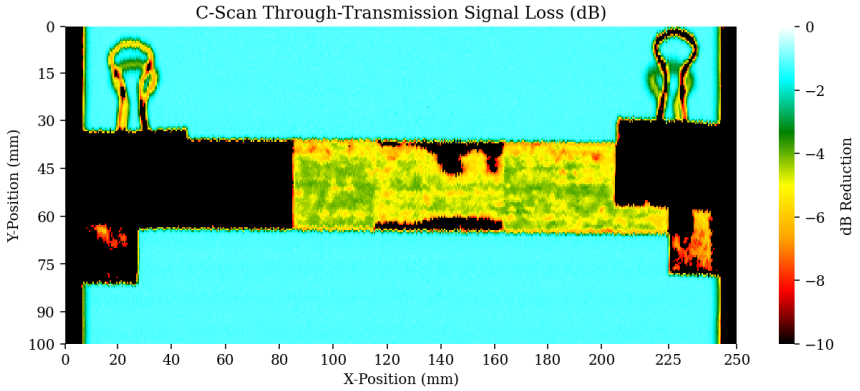

Figure 44: Singular RA-C Specimen C-Scan

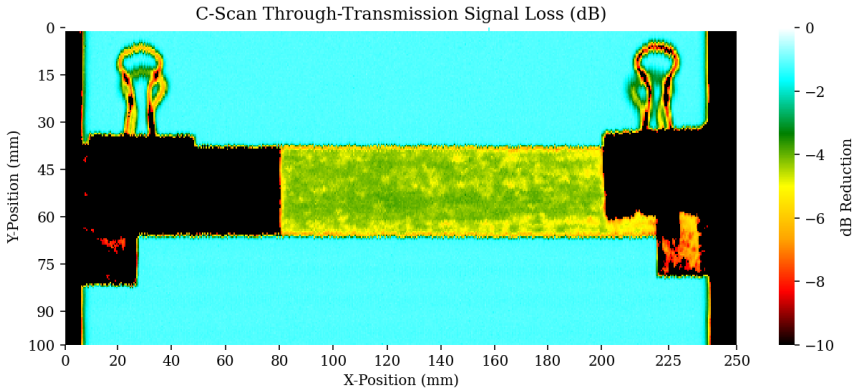

Figure 45: Singular RA-U Specimen C-Scan

Additionally, it seems that an operation between scanning the complete stack and scanning the individual specimens disturbed the RA-C contamination, as the black regions clearly indicate a disbond. This could originate from the clamping used in the cutting operation, or the cutting of the specimens themselves.

If the RA-Specimens fail through adhesion failure, it can be stated that kissing bonds were successfully introduced into these specimens. If the uncovered specimens show adhesion failure at the contaminated area, kissing bonds which are undetectable using C-Scan methods have been successfully replicated.

7.6.5 RA-O C-Scan

For the RA-O specimens, release agent was applied in a similar manner. However, due to manufacturing error an excess of release agent was applied, causing the contamination to spill over a larger area then intended. After the application of release agent to the adherend surface, the plasma surface treatment was applied similarly to the uncovered RA-Specimens. Additionally, these RA-O specimens were manufactured next to additional RA-U specimens in a rectangular shape, but these were not used. The complete and partial C-Scan from the RA-O stack can be found in Figure 46 and Figure 47 respectively.

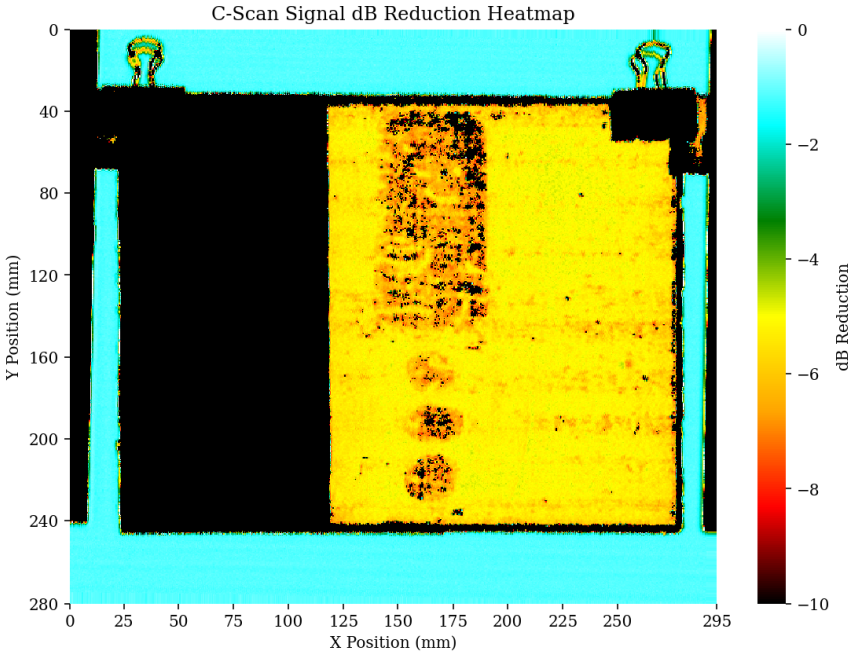

Figure 46: Release Agent Stack complete C-Scan - Circular

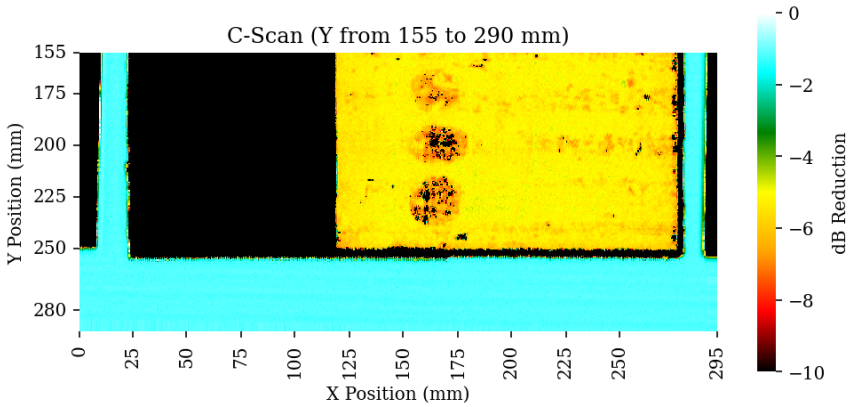

Figure 47: Release Agent Stack - Uncovered - Circular

As can be seen from the C-Scan, the contaminated region is clearly visible. This is even though the surface was also treated with plasma treatment, which in the case of RA-U Specimens resulted in the contamination being invisible from C-Scan. This is likely a result of excessive release agent being applied as a contamination as compared to the other RA-C and RA-U specimens described above. Of this stack, 3 RA-O specimens were manufactured. The remaining rectangular contamination was tested, but the results were not desirable and disregarded, when compared to the better produced RA-U specimens.

7.7 Specimen Final Preparation

After scanning the adhered plates, the plates are cut into final specimens. They are cut to their final length and width according to the specimen design Figure 22. Cutting is done using a Compcut ACS 600 cutter, using a diamond encrusted cutting wheel. After cutting, the thickness variation of the specimen was measured over the bonded length. The results of these thickness measurements can be found in Table 9. Here, measurements taken at defected areas are highlighted in yellow.

The variation in the specimen thickness is consistent, varying only 0.5 to 2 % over the bonded area length. This indicates that the adhesive carrier embedded in the adhesive film was sufficient enough in preventing excessive squeeze out. It also shows that the contaminated area does not yield a noticeable difference in specimen thickness. Differences between specimens of the same defect type can be noted. These are caused by squeeze out along the edges of the adhered stack, such as AC3 being close to the edge stack while AC1 is located in the middle, resulting in a reduced thickness for AC3.

After taking thickness measurements, load blocks are attached to the end of the pre-crack used for applying load to the specimen during the DCB test, in accordance with ASTM D5528-13 [5]. The sides of the specimens are painted and marked which will be used for tracking crack propagation throughout mechanical testing. Lastly, the surface where the defect was applied was carefully tracked and marked, to ensure the defect is consistently on the top adherend adhesive interface during testing.

Table 9: Thickness measurements of specimen over bonded area

Specimen	1	2	3	4	5	6	7	**Avg [mm]**	**SD [mm]**	**Deviation [%]**
P1	2.58	2.52	2.52	2.53	2.53	2.53	2.53	2.53	0.019	0.76
P2	2.65	2.59	2.58	2.58	2.57	2.57	2.57	2.59	0.027	1.03
P3	2.59	2.55	2.55	2.55	2.56	2.55	2.53	2.55	0.017	0.66
AC1	2.63	2.59	2.58	2.58	2.61	2.59	2.55	2.59	0.023	0.90
AC2	2.62	2.58	2.57	2.58	2.59	2.59	2.56	2.58	0.018	0.68
AC3	2.53	2.50	2.45	2.47	2.50	2.50	2.47	2.49	0.025	0.99
RA-C1	2.61	2.57	2.54	2.54	2.56	2.56	2.59	2.57	0.024	0.92
RA-C2	2.61	2.57	2.53	2.54	2.53	2.56	2.56	2.56	0.026	1.02
RA-C3	2.63	2.62	2.58	2.55	2.57	2.58	2.57	2.59	0.027	1.03
RA-U1	2.67	2.66	2.66	2.63	2.62	2.63	2.62	2.64	0.020	0.74
RA-U2	2.57	2.54	2.53	2.54	2.54	2.54	2.54	2.54	0.012	0.46
RA-U3	2.58	2.54	2.50	2.48	2.50	2.53	2.55	2.53	0.032	1.27
RA-O1	2.55	2.58	2.43	2.49	2.53	2.56	2.57	2.53	0.049	1.94
RA-O2	2.61	2.6	2.54	2.53	2.54	2.56	2.53	2.56	0.031	1.21
RA-O3	2.58	2.55	2.53	2.56	2.56	2.54	2.53	2.55	0.017	0.66

7.8 Summary

A range of adhesively bonded composite specimens was fabricated used for studying the detectability of kissing bonds using acoustic emission monitoring. Different defect types were included in order to simulate different adhesive bond defects, including pristine specimens, inclusion type defects and interface defects or kissing bonds.

All specimens were based on a unidirectional $[0]_8$ carbon fiber laminate bonded with AF163-2k epoxy based adhesive film. The composite material, being outdated and stored under unknown storage conditions, was subjected to extensive debulking stages and an alternative curing cycle to improve the quality of the product. Heated vacuum debulking and an additional dwell stage during vacuum curing were implemented to improve the quality of the carbon. These improvements were verified using ultrasonic C-Scans, performed after every production adjustment. Significant improvements in the quality of the carbon fiber material could be realized over numerous production iterations.

After the carbon fiber was deemed to be of sufficient quality, adhesive bonding was performed where five defect types were introduced:

- **Pristine (P):** Specimens with no intended defects introduced. Act as baseline specimens.
- **Adhesive Carrier Film (AC):** Specimens with a section of embedded protective film from the adhesive film between the adherend and adhesive interface. Represents inclusion-based defects.
- **Release Agent - Uncovered (RA-U):** Specimens contaminated with Marbocote 227-CEE release agent. Contamination of the adherend, left exposed during plasma treatment, intended to represent a kissing bond defect.

- **Release Agent - Covered (RA-C):** Similar to RA-U specimens, but the contamination was covered during plasma treatment to study the effectiveness of plasma treatment on release agent contamination.
- **Release Agent - Circular (RA-O):** Specimens contaminated with release agent, similarly prepared as RA-U specimens. Introduced to represent a partial kissing bond and to study the effect of disbond geometry and possible AE interaction.

Defect size and shape were controlled using pre-cut templates for contamination application. Surface preparation was done using corona plasma surface treatment to ensure good bonding outside the defective regions. Adhesive thickness showed minimal variability of less than 2%, indicating a consistent adhesive layer thickness with minimal squeeze out occurring during the autoclave curing process. Lastly, careful handling of specimens, material and tooling were adhered to throughout the production process in order to minimize unintended variations between specimens, as well as to avoid introducing unintended contamination.

C-Scan ultrasonic testing was used to verify the application of contamination. AC contamination was visible, which was expected due to its inclusive nature. RA-C specimens showed partially visible contamination, while RA-U specimens showed no contamination present. If the contamination still negatively effects the bonding, successful implementation of a kissing bond defect has been achieved. RA-O specimens showed the most visible defects of all release agent contamination types, despite being treated in the same manner as RA-U specimens with the use of corona plasma surface treatment. This was likely the result of excessive release agent being used during the application process.

Lastly, specimens were finalized by being cut to size according to ASTM D5528-13 standards. The specimens were C-Scanned once more which allowed for a direct comparison between defect types. The defect location was carefully marked to ensure consistent orientation of specimens during mechanical testing. The specimens were then painted and marked for tracking crack propagation while being tested.

The production process resulted in a final set of specimens with numerous defect types suitable for DCB testing to study the Acoustic signals emitted of a specimen subjected to Mode I loading. Mechanical testing of specimens will reveal the failure modes of these specimens and how this varies with the different introduced defects.

7.9 Discussion

While a sufficient number of specimens was successfully manufactured, there are several area's of limitations which were identified throughout the production process which should be considered for future reference.

Firstly, the condition of the supplied prepreg material raised varying issues. While extensive debulking and adjusted curing cycles improved upon the quality, the results achieved were not consistent for manufacturing multiple batches of specimens through different production runs. Additionally, while the quality was sufficient enough for obtaining good quality C-Scans, it remains to be proven if the production improvements resulted in a strong enough composite material. Lastly, implementing improvements and the iterative nature of trying to achieve a higher quality material took an excessive amount of time. The lengthened debulking stages also greatly increased the time between

iterations and the production production time of specimens.

Due to the presence of defects in the composite material in early production runs, adherend panels were manufactured in smaller batches instead of large singular panels. This approach improved individual panel quality, as a smaller panel could be made of higher quality. However, this possibly introduced variability in the material properties of the carbon material itself between production batches.
Using a better quality prepreg material would have been preferable and likely resulted in a more consistent quality composite. This would have required less production iterations and reduced delays experienced in the manufacturing process. A different composite prepreg (M30SC/DT120) was used during this research as an alternative material. Specimens made using this material were manufactured and tested, but improvements in the initial material made the switch to a new material no longer a necessity.

UV/Ozone treatment was used in the initial stages of fabricating specimens. These specimens however resulted in the adherend delaminating at the adhesive interface. It was concluded that with the carbon material available, UV/Ozone treatment degraded the material such that it would delaminate before the adhesive could fail. Hot atmospheric plasma surface treatment was attempted, but resulted in similar failure. Corona plasma surface treatment was more effective in producing specimens suitable for testing. However, given a different carbon fiber material, UV/Ozone treatment can be more applicable instead. This method is faster, results in a more consistent treatment of the surface and is shown to introduce cohesive failure in bonded specimens in similar research [68] [41].

RA-O contamination was challenging to introduce in a consistent size and amount of liquid release agent. Liquid release agent is prone to spreading on the surface when applied, especially since the surface has been treated which greatly increases wettability. A more consistent method of application can be used to reduce uncertainties from applying by hand. The liquid could for example be measured to ensure a consistent amount is being applied. Additionally, spraying the liquid with a fine mist might reduce excessive use, which leads to more severe contamination.

While RA-U specimens were contaminated using release agent, the contamination could not be detected using traditional C-Scan measurements. If adhesion failure occurs during testing, kissing bonds have been successfully recreated in this set of specimens. However, if these specimens do not show reduction of adhesion, different methods of surface preparation or defect types should be considered instead. In that case, corona plasma surface treatment is proven to reduce or remove the adverse effects of unintended contamination of release agent on a bonded surface.

While the used production process resulted in sufficient specimen quality to meet the objectives of the study, future efforts should be made to improve material quality and to further refine the introduction of artificial defects. Lastly, surface treatment should be further refined to improve repeatability of the coming experiments.

8 Mechanical Tests

Double Cantilever Beam (DCB) tests were conducted to subject the specimens to Mode-I fracture. The purpose of the mechanical tests is to obtain mechanical data used for comparison of specimens, in order to assess fracture behavior of the adhesive bondline. Additionally, mechanical testing would be used to verify if the intentionally introduced kissing bond defects were introduced successfully using the applied contamination, leading to adhesion failure at the adherend adhesive interface.

8.1 Test Setup and Method

The tests were performed in accordance with ASTM D5528-13 [5], using displacement controlled test speed of 4mm/min of crosshead displacement. All testing was performed on a 10 kN Zwick test bench, using a plate mounted 1 kN loadcell. A digital camera was used to monitor crack growth of the specimen, taking images every 5 seconds during testing.

Load blocks were attached to the ends of the specimen, being carefully constrained to ensure loading is applied consistently to not subject the specimens to torsion under static tension testing conditions. The specimens were painted and marked in order to track the crack tip using the captured images. These markings were also used to identify when the crack length reached 100 [mm], after which the test was manually ended. After ending the test, the specimen was returned to its starting position. During this unloading of the specimen, no images or acoustic data was captured. A single acoustic sensor was used to capture acoustic data, which was positioned 20 [mm] from the end of the specimen, as can be seen in Figure 48.

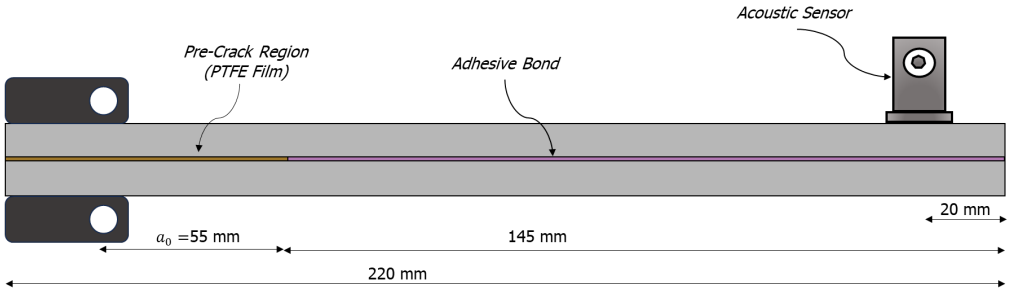

Figure 48: Specimen Geometry with Sensor Placement

The load and displacement measured by the test-bench were parametrically output to the camera capture software and Acoustic measurement system, to directly link mechanical loads subjected to the specimen to measured events.

Not all specimens testing will be discussed in the coming results. Excluded will be the Release Agent Covered (RA-C) and Release Agent Square (R). This is because RA-C is identical in shape and contamination as RA-U, however invisible on C-Scan as discussed in Chapter 7. R was much more visible and manufacturing error meant that a much larger area was affected. Because RA-U is a clear kissing bond and the specimens failed as intended, these are the specimens to be analyzed.

Additional specimens containing no defects were tested prior to the production of the final batch of specimens. Pristine Specimens P4 and P5 showed clean cohesive failure like the other pristine specimens. They were monitored using AE and the crack propagation was tracked using captured images. However, no C-Scans were taken and no thickness measurements were done for these specimens as they were intended for practicing the testing of the final specimens. However, they showed clean, cohesive failure identical to the other pristine specimens. Therefore, these specimens are still included to capture a "baseline" force-displacement curve for a sample containing no defects. Additionally, their acoustic data will be used in order to study cohesive failure. Since crack propagation rate was captured, they are also included from the G_{Ic} comparison.

8.2 Data Processing

The DCB tests resulted in force-displacement curves, where force [N] and cross-head displacement [mm] of the static tests were sampled at a frequency of 10 [Hz]. Using the images captured by the digital camera, crack length can be measured and directly linked to the load and displacement data. The crack length is visually measured at intervals of 5 seconds as per the camera capture rate.

8.2.1 Local Fracture Toughness G_{Ic}

To quantify the fracture resistance of the adhesive bond under Mode I loading conditions, the strain energy release rate G_{Ic} was computed using Modified Beam Theory (MBT), as specified by ASTM D5528-13 [5]. This method assumes linear elastic behavior and is applicable for unidirectional carbon fiber composites when crack growth is present along the fiber direction. Using force-displacement data, along with measured crack lengths of the adhesive bond at each location, the mode I fracture toughness G_{Ic} of the bond can be computed.

This method of calculating G_{Ic} is particularly used for pristine specimens, where crack progression is expected to be smooth and continuous. This allows for local energy release rates $G_{1c}(a)$ to be computed using the image-based crack monitoring at each point in the crack propagation. Local in this instance, referring to the fact that G_{1c} is computed at each location of the crack growth path.

A region of reduced G_{Ic} indicates a reduction in resistance to fracture. Bondlines defects, such as kissing bonds, can create rapid decreases, reducing the G_{Ic} to effectively zero over the contaminated area. Crack growth in defective specimens can also be highly discontinuous, caused by periods of stagnation in crack propagation following a period of rapid crack growth due to the presence of defects.

Under such conditions, using local G_{Ic} values is not applicable. Due to large variations in the failures of the specimens, local G_{Ic} comparisons can not be made directly as the conditions for MBT are no longer valid. Computed G_{Ic} values for these specimens depend on the test duration and number of crack propagation observed, resulting in non-replicable results among the different specimens.

The local strain energy release rate G_{Ic} is calculated at each point of the measured crack front using Equation 1.

$$G_{IC}\left(a_i\right) = \frac{3P_i\delta_i}{2b\left(a_i + \Delta\right)} \cdot F_i \tag{1}$$

where:

- P is the applied load (N)
- δ is the cross-head displacement [mm]
- b is the specimen width [mm]
- a is the crack length as measured from the load line [mm]
- Δ is a crack correction factor
- F is a correction factor for large displacements

Here, Δ is taken to be 2mm approximately. Large displacement correction F is applied according to Annex A1 of the ASTM 5528-13 standard [5]. It accounts for large displacements due to flexible adherends causing excessive bending. The correction factor is computed using Equation 2:

$$F = 1 - \frac{3}{10}\left(\frac{\delta}{a}\right)^2 \tag{2}$$

For each pristine specimen, the applied load and crosshead displacement where recorded and matched with optical crack tracking. Crack length was determined manually from these images. All force displacement data were measured directly from the load cell and crosshead encoder of the Zwick test frame.

As the start of the adhesive layer did not start perfectly aligned with the markings made on the specimen, a crack length correction distance $a_{corrected}$ was introduced to account for this. This ensures the force displacement data was accurately matched to the onset of crack growth monitored through the images.

The resulting G_{Ic} values were computed at each interval of imaging using the equations above and are plotted against the corrected crack length. This provides a direct comparison between the local fracture resistance as function of crack length, which can be directly compared to the fracture surface of the specimens after testing.

To see how much each defect impacts the bond strength, G_{Ic} is computed throughout the test-duration for pristine specimens. The fracture toughness is plotted and compared to crack length, such that a local drop in G_{Ic} indicates that the crack advanced with less resistance, suggestion a region of reduced local fracture toughness. This can be due to a transition from cohesive to adhesion failure, loss of adhesion due to a kissing bond or rapid crack growth. Each image captured during the test gives the actual crack length a. Given that the independently measured mechanical data can be linked to each crack length interval, each data point of G_{Ic} represents the mechanical state of the bond after an interval of crack growth.

Critically, to compute the local fracture toughness and quantify the effects of local defects, the crack must be contained to either the bond layer or the adhesive adherend interface. Some specimens tested showed other failure modes besides failure in the bond layer, such as inter-laminar shear failure and delamination in the adherend itself.

8.2.2 Global Effective Fracture Toughness $G_{\mathbf{eff}}$

An effective fracture energy G_{eff} is computed directly using the force-displacement data. It represents the total energy required per unit area for crack propagation. This metric is used for consistent comparison of mechanical performance for specimens containing both pristine and defective bonds.

The G_{eff} is obtained through integrating the force-displacement curve up to the point of final crack growth. The elastic unloading of the specimen was truncated from the data, as elastic recovery of the adherends does not contribute to the crack propagation. Additionally, defective specimens can result in catastrophic failure, not allowing for an unloading of the specimen to take place.

$$G_{eff} = \frac{U}{b \cdot \Delta a} \tag{3}$$

- U: Area under Force-Displacement curve [N $\cdot$ mm]
- b: Specimen width [mm]
- Δa: Adhesive crack length [mm]

It should be noted that ASTM D5528-13 does not recommend using area under the curve estimations to compute G_{Ic} at distinct crack lengths. However, this metric can still provide insights into the global fracture performance of defected joints. In short:

- G_{Ic}**:** Calculated to study resistance to crack propagation in pristine specimens. G_{Ic} is also computed for defective specimens, but only for analyzing the onset of it's reduction, indicating points of failure.
- G_{eff}**:** Calculated for all specimens as a method of comparison of fracture resistance of pristine and contaminated specimens.

8.3 Mechanical Test Results

Mechanical testing revealed varying results when defects in the material were introduced. Early delaminations were also observed, showing a possible reduction in the composite's inter-laminar shear strength which prevented complete cohesive failure of the bond, which is preferred.

8.3.1 Pristine Specimens (P)

The Pristine specimens failed almost completely cohesively, indicating good bonding between the adhesive and adherend, which means the steps taken with regards to surface preparation were effective. The load displacement curves showed similar trajectories showing gradual crack propagation, as can be seen in Figure 49. The corresponding fracture surfaces are shown below in Figure 50 and Figure 51.

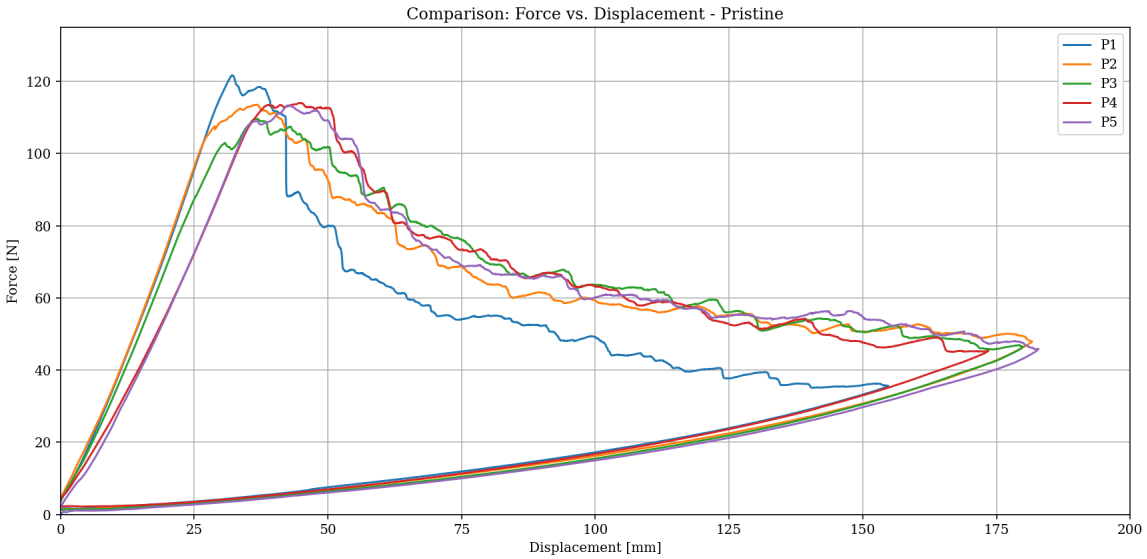

Figure 49: Force-Displacement Curve - All Pristine Specimens

Cohesive failure was the predominant failure mode, indicated by the pink coloration of the fracture surface. While cohesive failure was the dominant failure mode, some delamination did occur in small regions, most notably in specimen P1, indicated by the black streaks of fibers running along the specimen in Figure 50a. This can also be seen in the force-displacement curve in Figure 49, as only P1 shows an initial sharp drop at approximately 40 [mm] crosshead displacement, indicating rapid crack growth opposed instead of gradual adhesive degradation. The difference can clearly be observed when considering the fracture surface of P3, shown in Figure 50c. Here, the more dominant cohesive failure results in a more gradual degradation in the force-displacement curve.

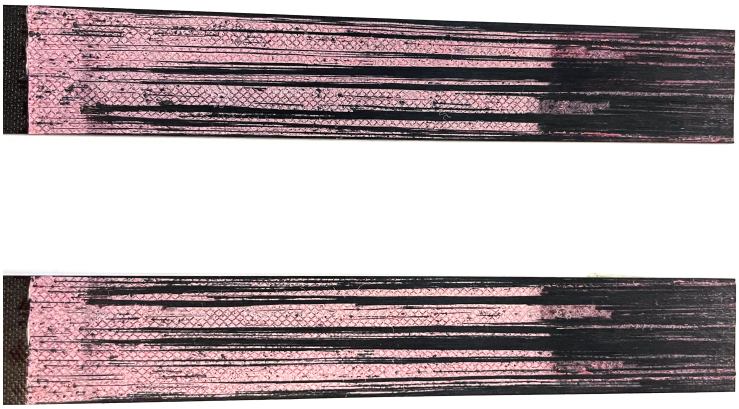

(a) P1 fracture surface

(b) P2 fracture surface

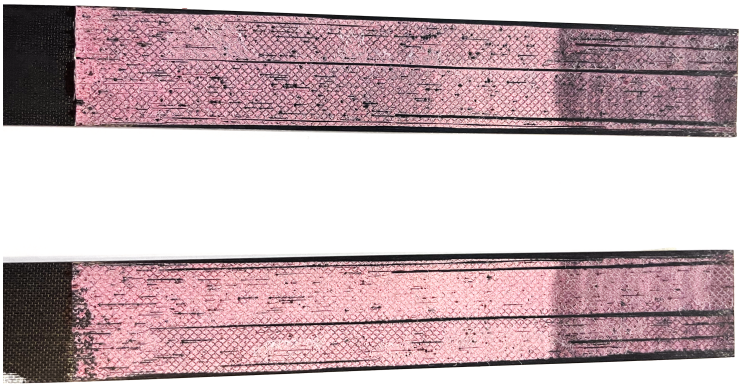

(c) P3 fracture surface

Figure 50: Fracture surfaces of pristine specimens: (a) P1, (b) P2, (c) P3

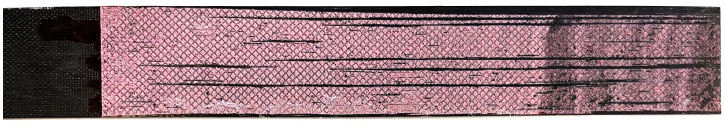

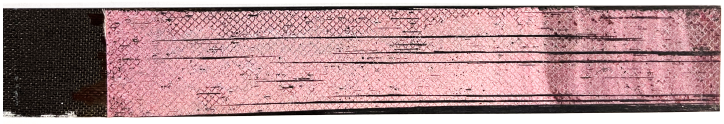

(a) P4 fracture surface

(b) P5 fracture surface

Figure 51: Fracture surfaces of pristine specimens: (d) P4, (e) P5

In order to compare the effects of defects on the bondline strength, force displacement curves of defective specimens will be compared to a baseline set by pristine specimens. For this, a baseline must be established representing a bonded joint with no defects. Plotted below in Figure 52 are the pristine specimens plotted once more in a single curve, along with the average force of these forces and an uncertainty region of one standard deviation to signify the variability of results. Due to the delaminations present in P1, it is excluded from this baseline comparison. However, the mechanical data from P1 will be used to study the impact of the delaminations on the G_{1c} of the specimen.

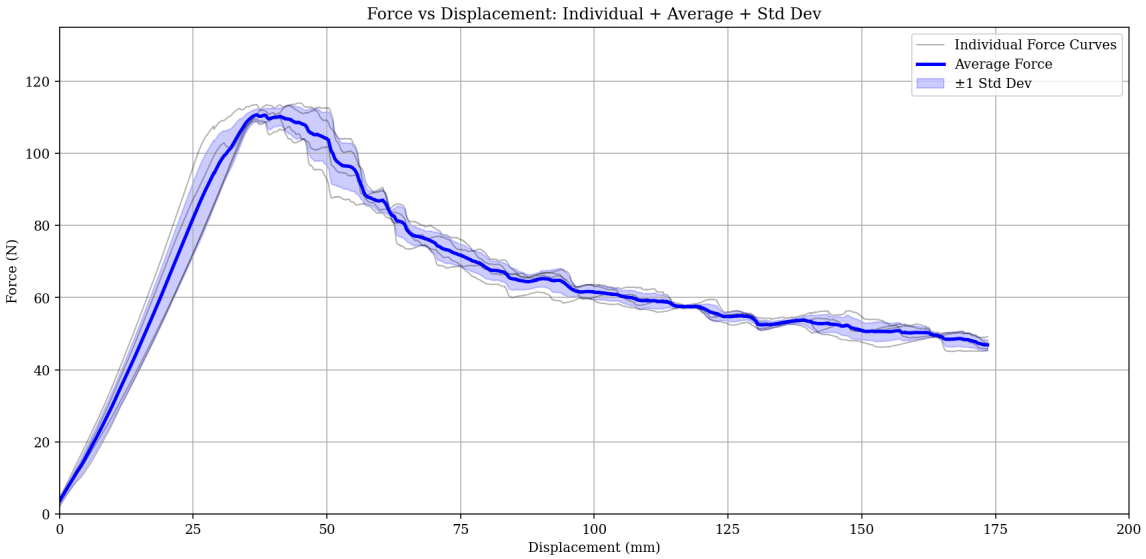

Figure 52: Baseline Pristine Average Load Displacement curve

In order to obtain an estimation of the local Fracture Toughness G_{Ic}, the crack front was measured using the images captured during testing. An example of the measured crack-length of specimen P1 can be found in Figure 53.

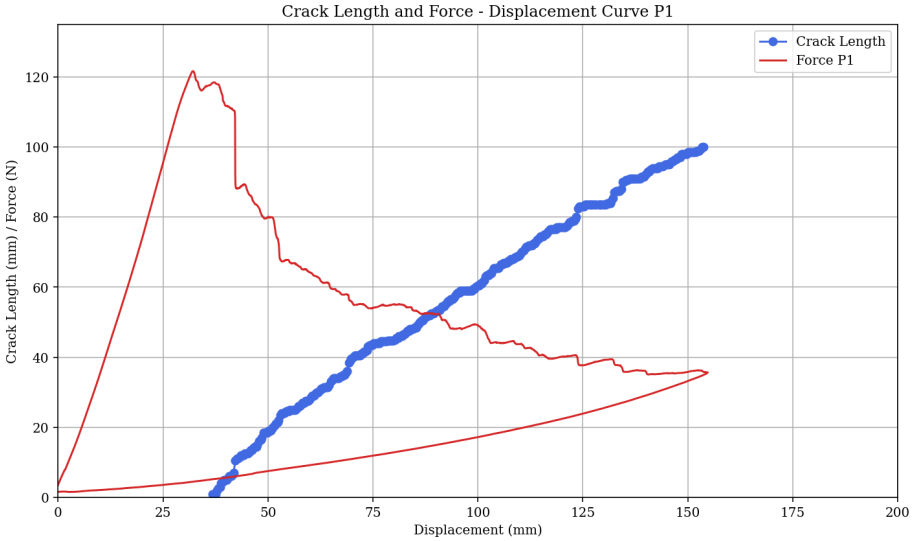

Figure 53: Crack Length vs. Displacement with Force-Displacement Curve for Specimen P1

What can be observed is that the measured crack length starts to propagate visibly after the load is near maximum load before reducing. This indicates failure of the bond and crack propagation

before initial crack growth was first measured. Additionally, an increase in crack length can be seen coinciding with drops in the force-displacement curve. This can be seen near a crosshead displacement of 40 [mm] for P1, where the delamination results in a jump in crack length.

Similarly, the crack progression plots for the remaining pristine specimens can be found in Figure 54 and Figure 54.

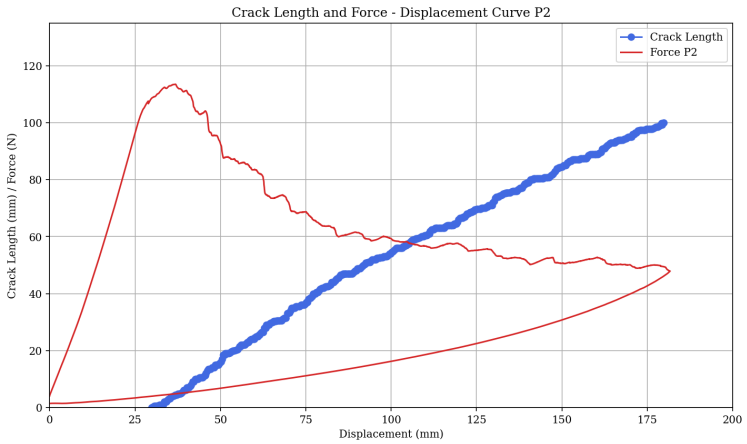

(a) Crack Length vs. Displacement with Force-Displacement Curve - P2

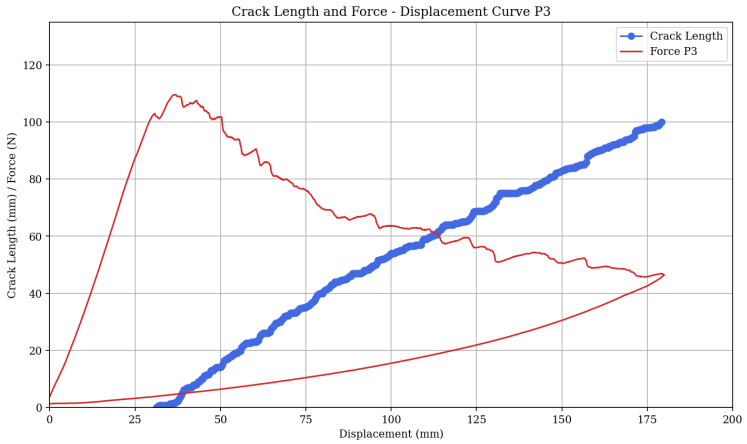

(b) Crack Length vs. Displacement with Force-Displacement Curve - P3

Figure 54: Comparison of Crack Length and Force-Displacement Curves for specimens P2 to P5 (Part 1)

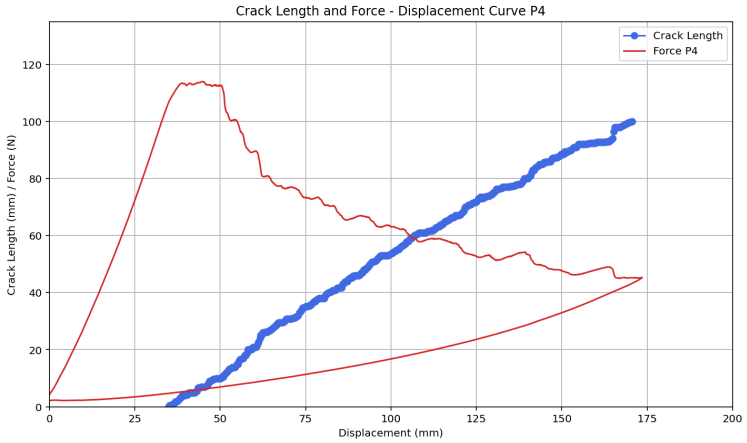

(c) Crack Length vs. Displacement with Force-Displacement Curve - P4

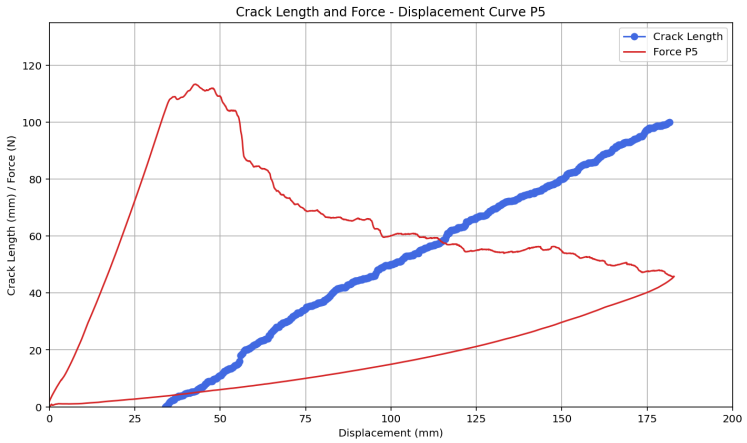

(d) Crack Length vs. Displacement with Force-Displacement Curve - P5

Figure 54: Comparison of Crack Length and Force-Displacement Curves for specimens P2 to P5 (continued)

As can be seen, crack growth for the pristine specimens is smooth and continuous, which allows for the calculation of the fracture toughness throughout the entire length of the bonded region. Using this measured crack length, combined with Equation 1, the local $G_{1c}(a)$ was computed. The result of Pristine specimens can be found in Figure 55 and Figure 56. Once more, each specimen is seen to have a gradually decreasing $G_{1c}(a)$. Figure 55a shows a rapid decrease at the point of delamination as visible on the fracture surface.

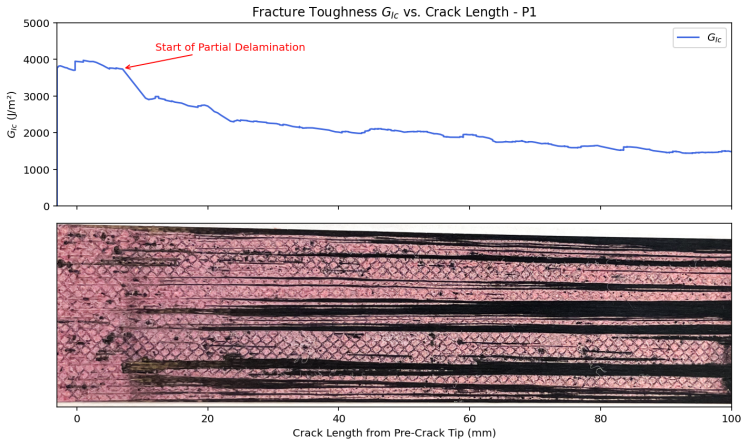

(a) G_{Ic} plotted over crack length for specimen P1

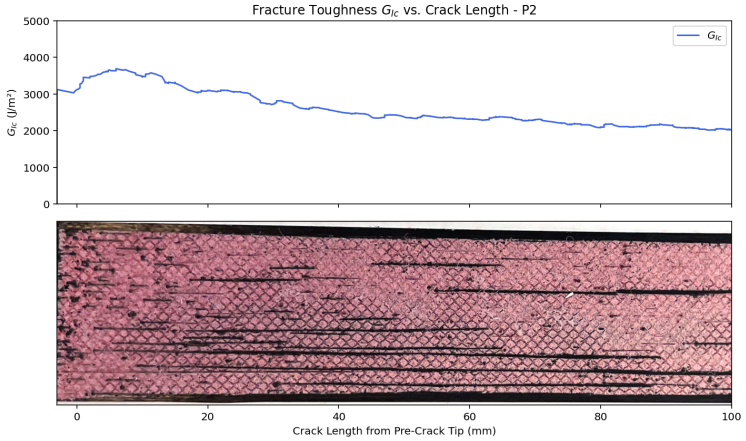

(b) G_{Ic} plotted over crack length for specimen P2

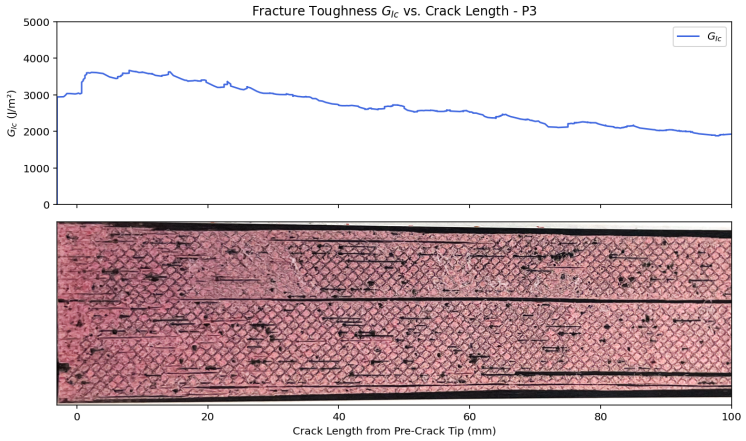

(c) G_{Ic} plotted over crack length for specimen P3

Figure 55: Mode I fracture toughness (G_{Ic}) as a function of crack length for pristine specimens: (a) P1, (b) P2, (c) P3.

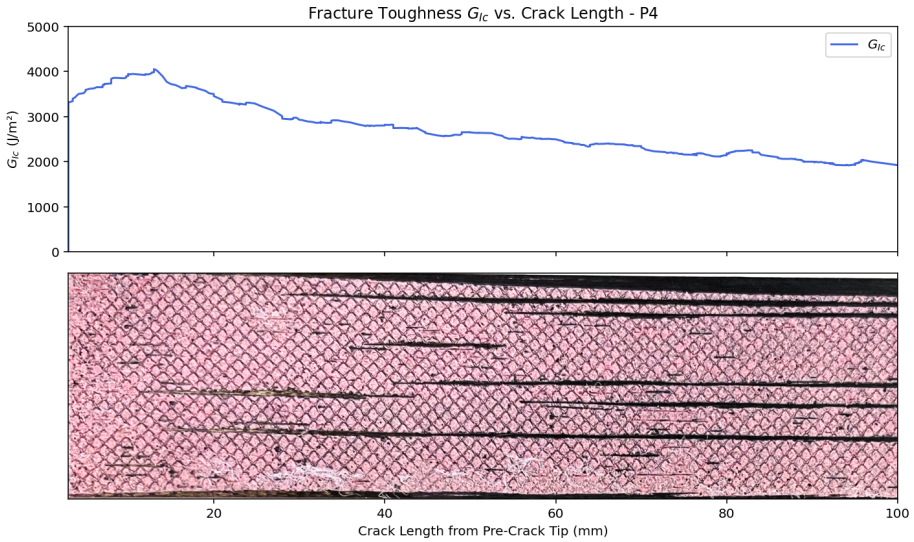

(d) G_{Ic} plotted over crack length for specimen P4

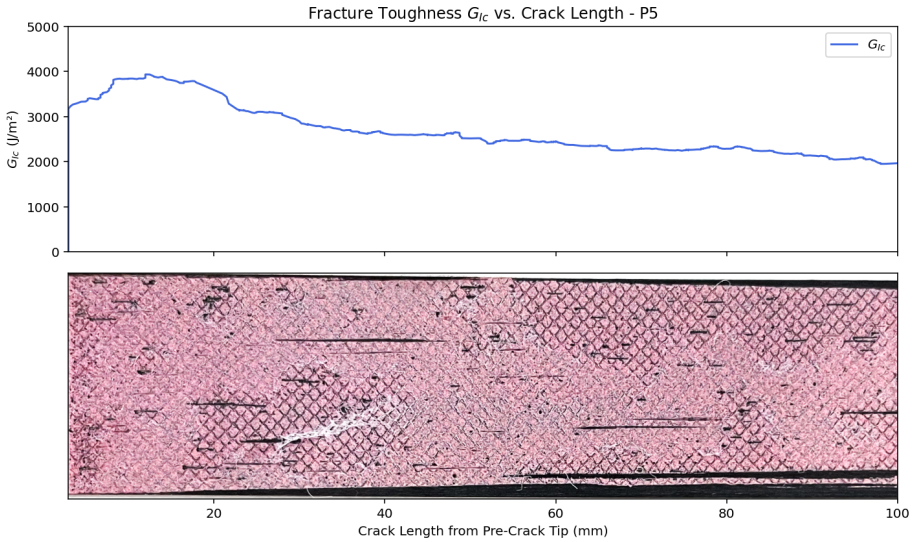

(e) G_{Ic} plotted over crack length for specimen P5

Figure 56: Mode I Fracture Toughness (G_{Ic}) as a function of crack length for pristine specimens: (d) P4, (e) P5.

8.3.2 Adhesive Film Carrier Specimens (AC)

Similarly, the specimens containing adhesive film carrier defects were tested. The force displacement curves and fracture surfaces of the specimens containing an adhesive film defect are shown below in Figure 57 and Figure 58 respectively. The average force-displacement of the pristine specimens are overlayed allowing for a direct comparison.

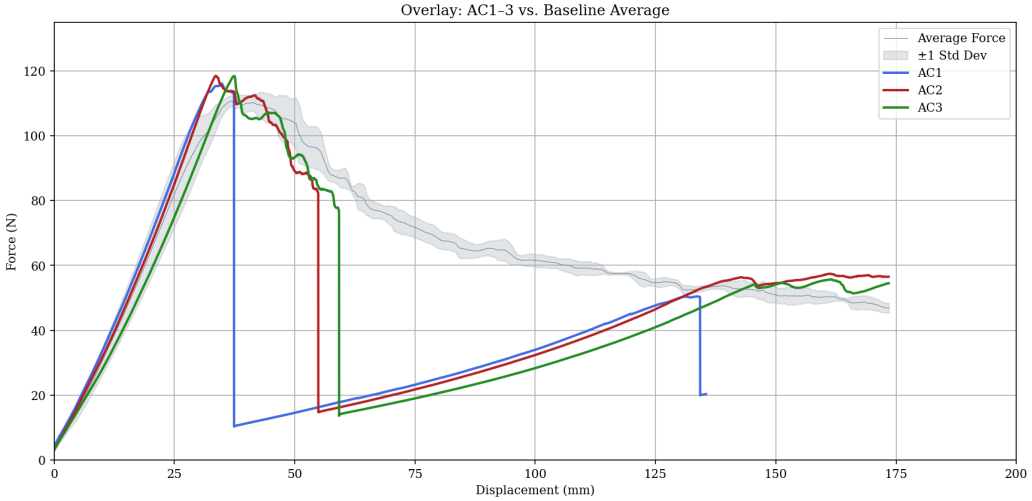

Figure 57: Force-Displacement Curves AC-Specimens

(a) Fracture surface of specimen AC1

(b) Fracture surface of specimen AC2

(c) Fracture surface of specimen AC3

Figure 58: Post-test fracture surfaces of artificially contaminated specimens: (a) AC1, (b) AC2, and (c) AC3.

As can be seen from the fracture surfaces, specimen AC1 shows a delamination early in the crack propagation path, taking up almost half the specimen's width. This delamination can also clearly be seen in the force displacement curve for this specimen, as a large decrease in load is observed at this point of the test at a crosshead displacement of 38 [mm]. This failure is also seen occurring much sooner compared to AC2 and AC3, which started with gradual cohesive failure, as can be seen in the force displacement curve as well as the fracture surface. When these specimens reached the adhesive film, zero adhesive capacity was observed, as expected. The crack propagated instantly over the entire length of the included defect, resulting in a large drop in load. For AC2 and AC3, this point was at approximately 55 to 60 [mm] crosshead displacement.

The gradual load increase after reaching the contamination is resulting from the specimen being loaded until the cohesive strength at the remaining adhered part at the end is reached. Once this point is reached at approximately 145 [mm] crosshead displacement for all specimens, gradual cohesive failure is continued. For specimen AC1 however, delaminations occurred throughout the entire length of the specimen, causing early and rapid failure around 135 [mm] crosshead displacement, shortly after a small region of cohesive failure, ending the test early.

Due to the unexpected failure of AC1, it will be excluded from further mechanical analysis comparison between AC and P specimens. It's local G_{1c} over the crack length will be computed to study the exact point of failure. The crack length growth curves used for estimating G_{Ic} are shown in Figure 59. The local G_{Ic} over the crack length for all 3 AC-Specimens can be found below in Figure 60.

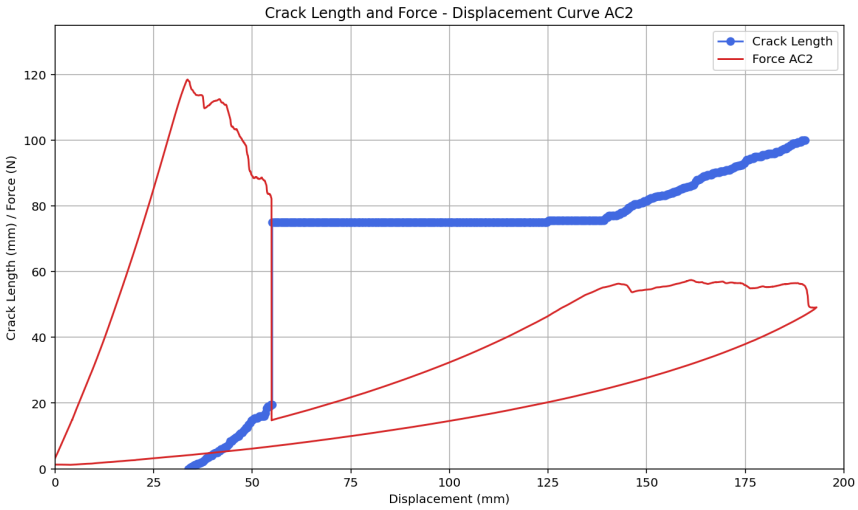

(a) Crack Length and Force-Displacement Curve – AC2

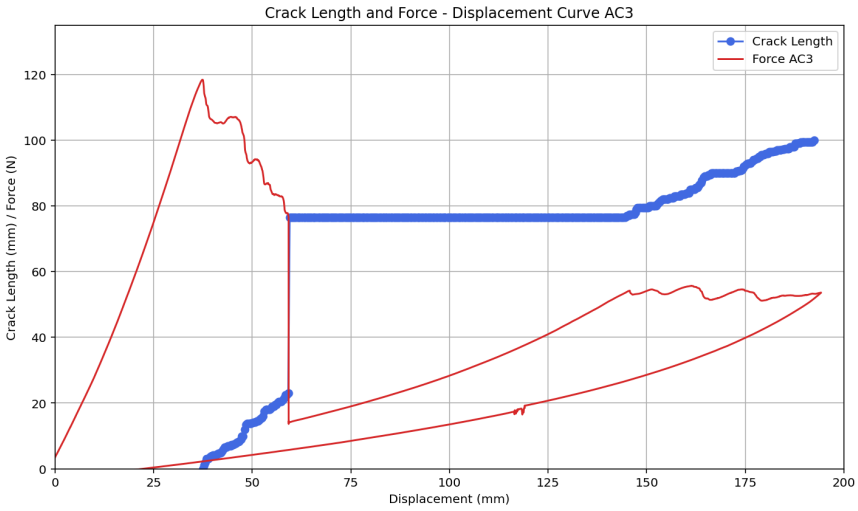

(b) Crack Length and Force-Displacement Curve – AC3

Figure 59: Comparison of Crack Length and Force-Displacement Curves for AC2 and AC3

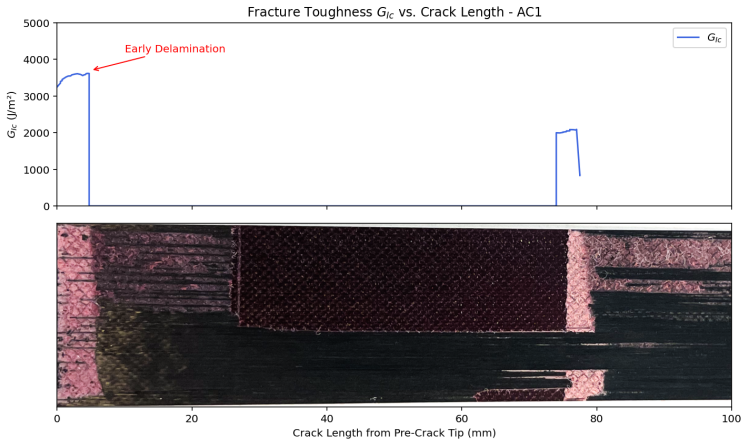

(a) G_{Ic} plotted over crack length distance – AC1

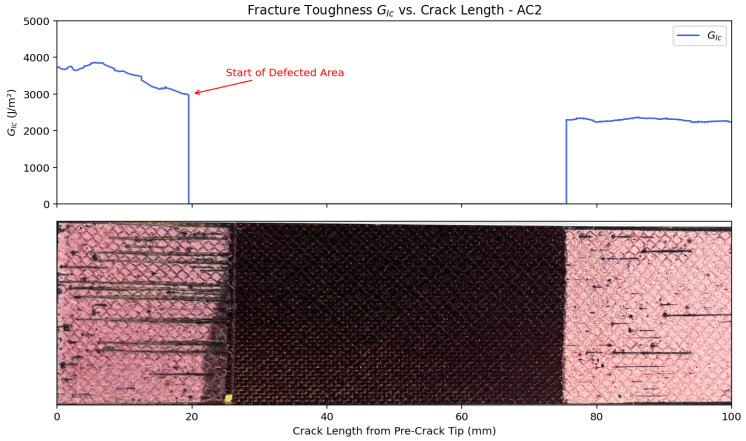

(b) G_{Ic} plotted over crack length distance – AC2

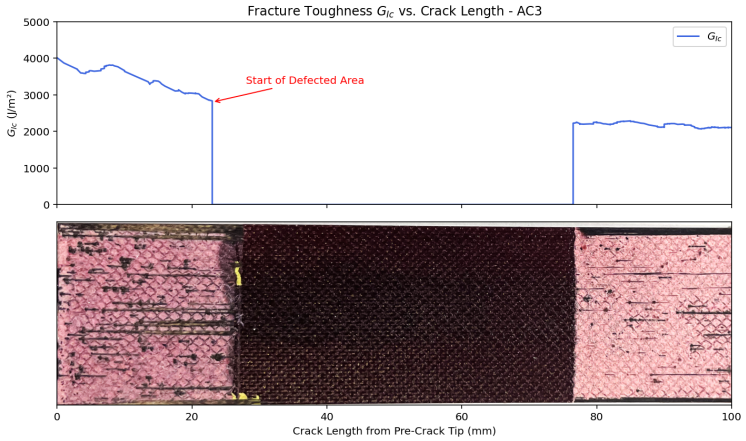

(c) G_{Ic} plotted over crack length distance – AC3

Figure 60: Fracture Toughness G_{Ic} versus crack length for artificially contaminated specimens: (a) AC1, (b) AC2, and (c) AC3.

The local G_{1c} of AC2 and AC3 starts at approximately the same value as per the baseline set by the Pristine specimens. When the crack front reaches the defected area, no adhesion occurs, meaning the G_{1c} effectively becomes zero over the length of the defect. Only when the end of the defected area is reached is the remaining crack front loaded again. When a certain load is reached that exceeds the local G_{1c} at this point, crack growth continues.

In order to have an estimate for the total fracture resistance for the entire bondline, G_{eff} is computed from the area below the force-displacement curve. This is done for all defective specimens, where their respective values will be compared in the subsection 8.4.

8.3.3 Release Agent Specimens (RA)

As previously described in section 7, several batches of specimens contaminated with release agent were tested. The first set contained rectangular release agent contamination of the same size as the adhesive film described above.

Release Agent (Uncovered Plasma Treatment)

The force-displacement curve and fracture surfaces of these specimens can be found in Figure 61 and Figure 62. First, it can be noted from the force-displacement curve that these specimens have an increased stiffness, as well as a higher maximum load before onset of failure. The reason of which is further discussed in the discussion.

As can be seen on the fracture surfaces of these specimens, mixed failure was observed. Both delamination and cohesive failure are present at uncontaminated areas of the fracture surface. This is noteworthy, as when a specimen delaminates, the behavior observed in the force displacement data is identical to adhesion failure as a result from contamination. As delamination occurs, it propagates rapidly in the adherend material, causing a load drop like adhesion failure.

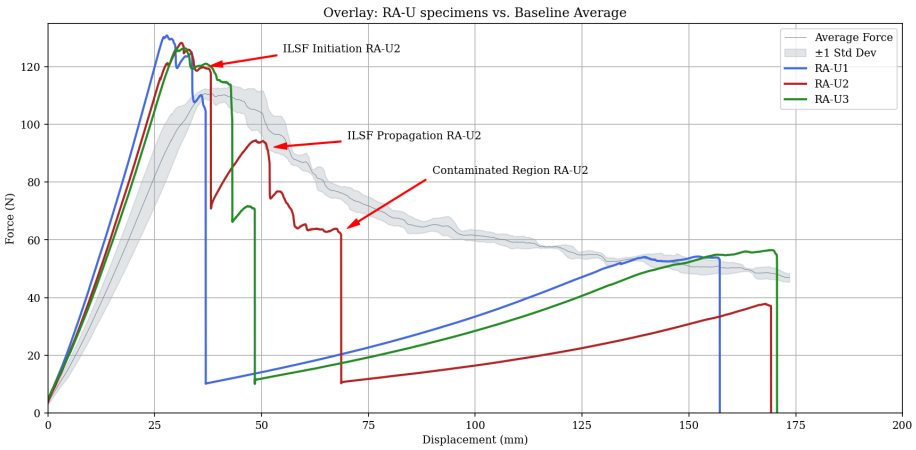

Figure 61: Force-Displacement curves of RA-U Specimens compared to Pristine Specimens

(a) Fracture surface of specimen RA-U1

(b) Fracture surface of specimen RA-U2

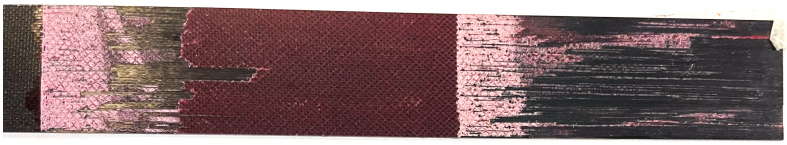

(c) Fracture surface of specimen RA-U3

Figure 62: Post-test fracture surfaces of RA-U specimens: (a) RA-U1, (b) RA-U2, and (c) RA-U3.

Specimen RA-U1 shows cohesive failure at the beginning of the crack growth, followed by early failure before the detective area is reached. This can be noted in the force displacement curve, as RA-U1 shows early failure when compared to the other specimens. Specimen RA-U2 does show majority cohesive failure before reaching the contaminated area. This can also be seen in the force displacement curves, where specimen RA-U2 shows gradual degradation of the bond before reaching a sharp load drop indicating rapid delamination or complete bond failure. RA-U3 experienced a similar failure as RA-U2. The cause of early delaminations occurring in these specimens, will be further analyzed in the discussion.

Specimen RA-U2 and RA-U3 also showed interlaminar shear failure at different points during the test. These failures can be seen in Figure 63. These interlaminar failures originated rapidly, then steadily grew up to a certain point. When not propagating, crack growth continued in the adhesive interface or adhesive layer. These failures are still noteworthy as they affect the results in the force displacement curve and fracture toughness. The instances of when ILSF occurred for specimen RA-U2 are highlighted in Figure 61.

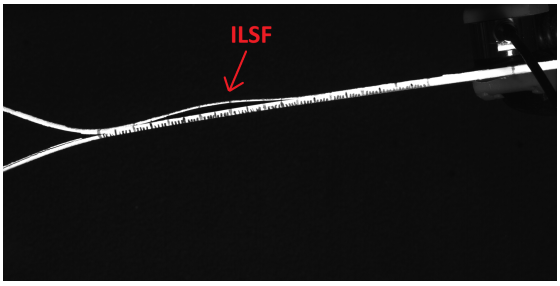

(a) Inter-Laminar Failure RA-U2. Occurring at Crosshead-displacement 38 [mm]

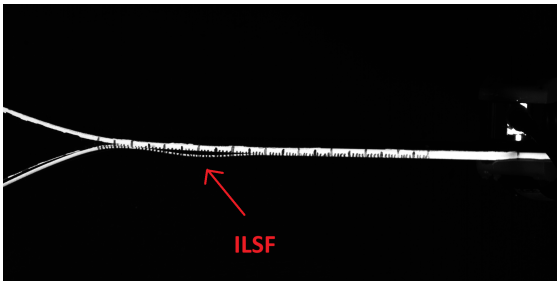

(b) Inter-Laminar Failure RA-U3. Occurring at Crosshead-displacement 43 [mm]

Figure 63: Inter-Laminar Shear Failure events for RA-U2 and RA-U3, highlighted in red

The crack length throughout the testing duration was measured and can be seen in Figure 64. The Fracture Toughness G_{1c} over the specimen length can be found in Figure 65.

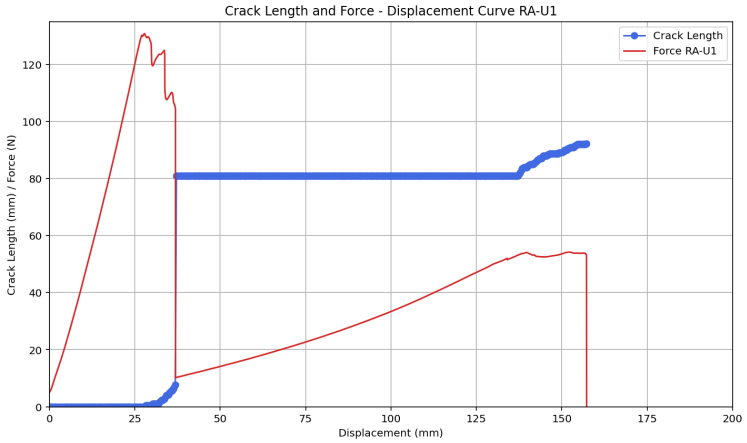

(a) Crack Length and Force-Displacement Curve – RA-U1

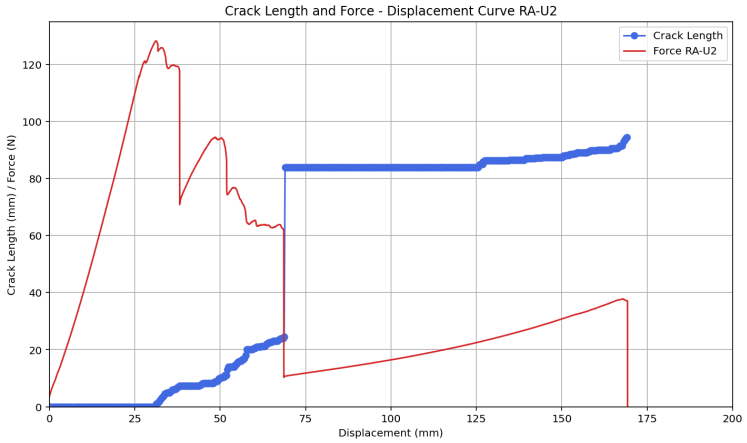

(b) Crack Length and Force-Displacement Curve – RA-U2

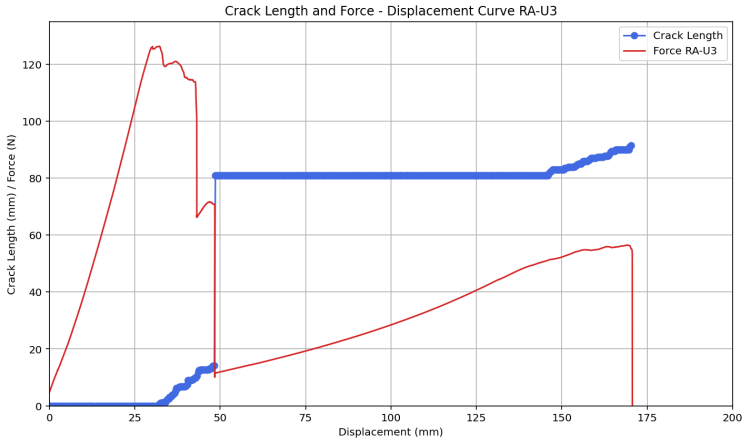

(c) Crack Length and Force-Displacement Curve – RA-U3

Figure 64: Crack length and force-displacement behavior of RA-U specimens: (a) RA-U1, (b) RA-U2, (c) RA-U3.

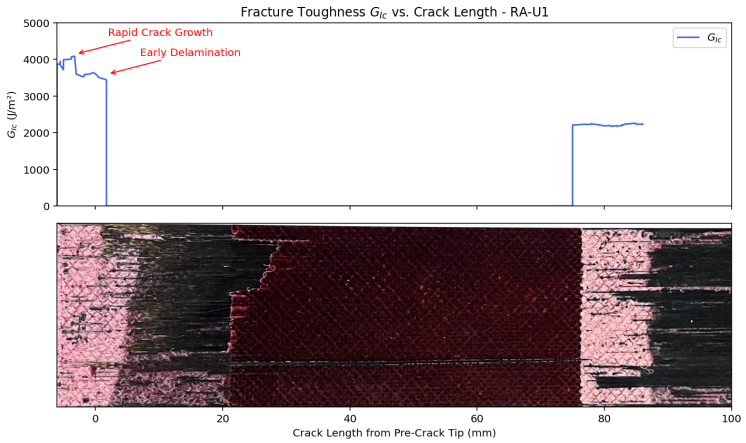

(a) G_{Ic} plotted over crack length distance – RA-U1

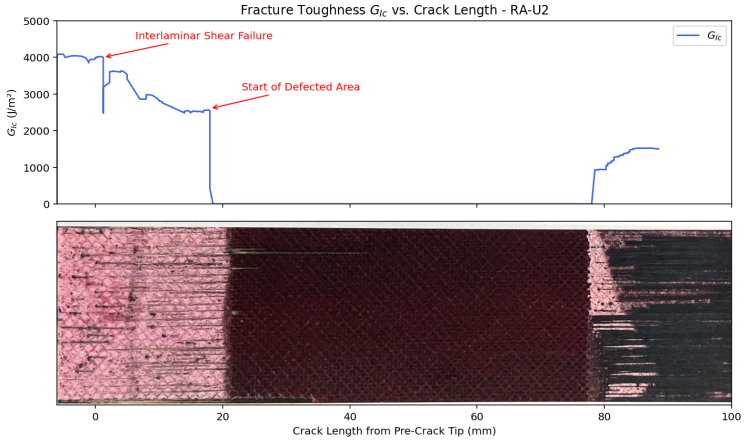

(b) G_{Ic} plotted over crack length distance – RA-U2

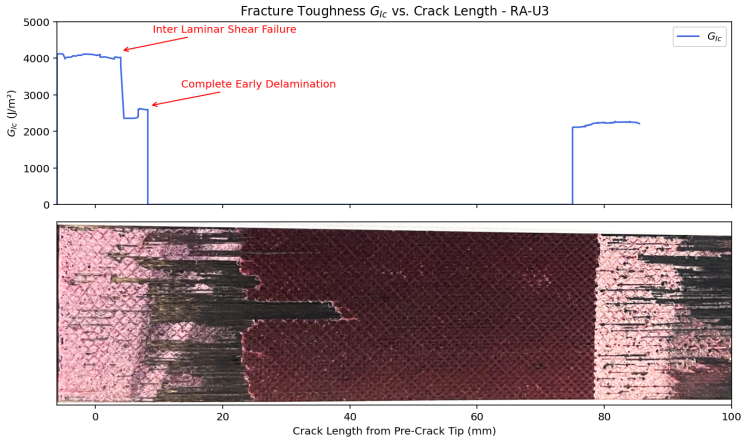

(c) G_{Ic} plotted over crack length distance – RA-U3

Figure 65: Mode I Fracture Toughness (G_{Ic}) plotted over crack length for RA-U specimens: (a) RA-U1, (b) RA-U2, (c) RA-U3.

For Specimen RA-U1, the first minor drop in load can be correlated to the partial delamination occurring at this crack length distance. For RA-U2 and RA-U3, this load drop coincides with the point of Inter Laminar Shear Failure (ILSF) shown in Figure 63. After load is increased and crack growth continues towards the end of the contamination, G_{1c} values increase. However, in the case for RA-U2, this is partially due to the inter laminar disbonds growing in the carbon adherend alongside the adherend adhesive interface. Therefore, a substantial part of the energy required to grow the bondline is propagating this failure. The inter-laminar shear failure region for RA-U3 was no longer growing at this stage, so the remaining G_{1c} for RA-U1 and RA-U3 are representative of the remaining bondline strength.

Release Agent - Circular

As previously mentioned in section 7, excessive release agent during manufacturing resulted in a larger contaminated area than intended. As can be seen on the fracture surfaces of these specimens, these indeed resulted in early adhesion failure and a more uneven disbonded area. The fracture surfaces for circular release agent kissing bonds show larger contaminated areas than intended, as can be seen in Figure 67. However, clear cohesive failure prior to reaching the contaminated region can be observed, especially for specimen O1, as can be seen Figure 67a. The force-displacement curves for these specimens can be found in Figure 66.

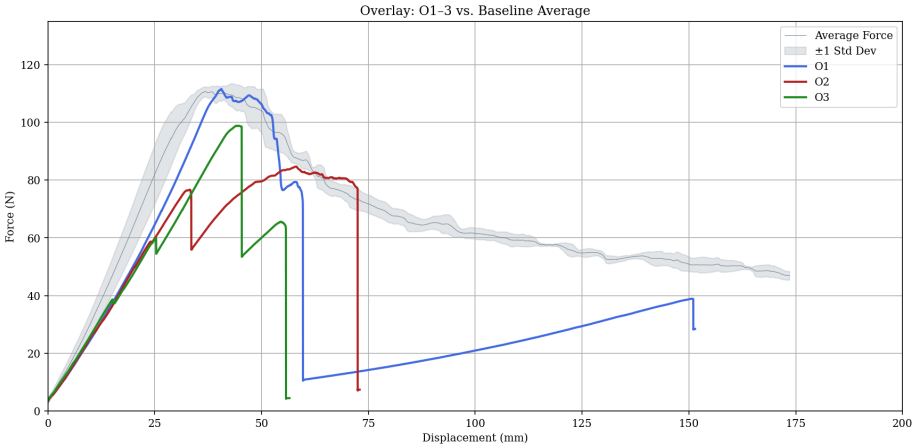

Figure 66: Force-Displacement curves of RA-C Specimens compared to Pristine Specimens

(a) Fracture surface of specimen O1

(b) Fracture surface of specimen O2

(c) Fracture surface of specimen O3

Figure 67: Post-test fracture surfaces of O-series specimens: (a) O1, (b) O2, and (c) O3.

Both O2 and O3 showed early failure. There was no onset of cohesive failure at the start of the bondline and both specimens did not reach the expected maximum applied load before onset of crack initiation. Due to the fact that O1 has the most representative failure, it will be used for further analysis of G_{1c}. The result of which can be found in Figure 68.

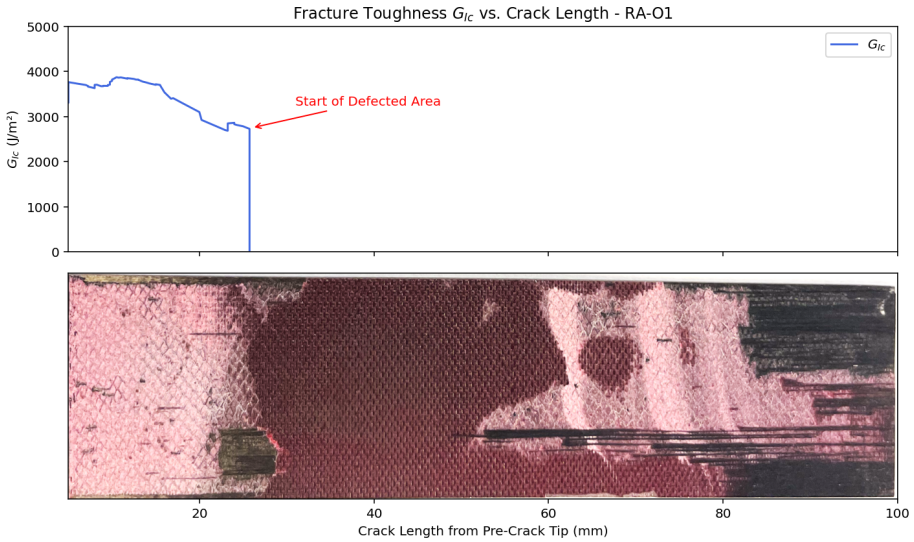

Figure 68: G_{Ic} plotted over crack length distance – RA-O1

As can be seen, adhesion failure occurs at approximately 25 [mm] crack length, which is the expected region where the defect starts. Even though cohesive failure fracture surfaces are noticeable from 60 [mm] crack length, crack growth was not consistent enough to attribute this region with an accurate value for G_{1c}.

8.4 Comparison of Results

Comparing the local fracture toughness G_{1c} allows for the estimation of bond strength for pristine specimens or pristine regions of defective specimens, and will offer further understanding on the different failure modes experienced for the defective specimens. The global effective fracture toughness will be used to compare overall bond integrity for all specimens.

8.4.1 Local Fracture Toughness G_{1c} Comparison

Pristine vs. AC Specimens

Below, the local fracture toughness G_{1c} of both the P and AC-Specimens can be found in Figure 69. As can be seen, before reaching the adhesive film inclusion, the adhesive film carrier specimens align closely in terms of local fracture toughness to the pristine. It can also clearly be seen that P1, due to partial delamination after around 5 [mm] crosshead displacement shows a similar trajectory, but with its entire line shifted down a bit. This is directly related to the reduced force needed to break

the bondline, as partial delamination requires less force to continue crack propagation.

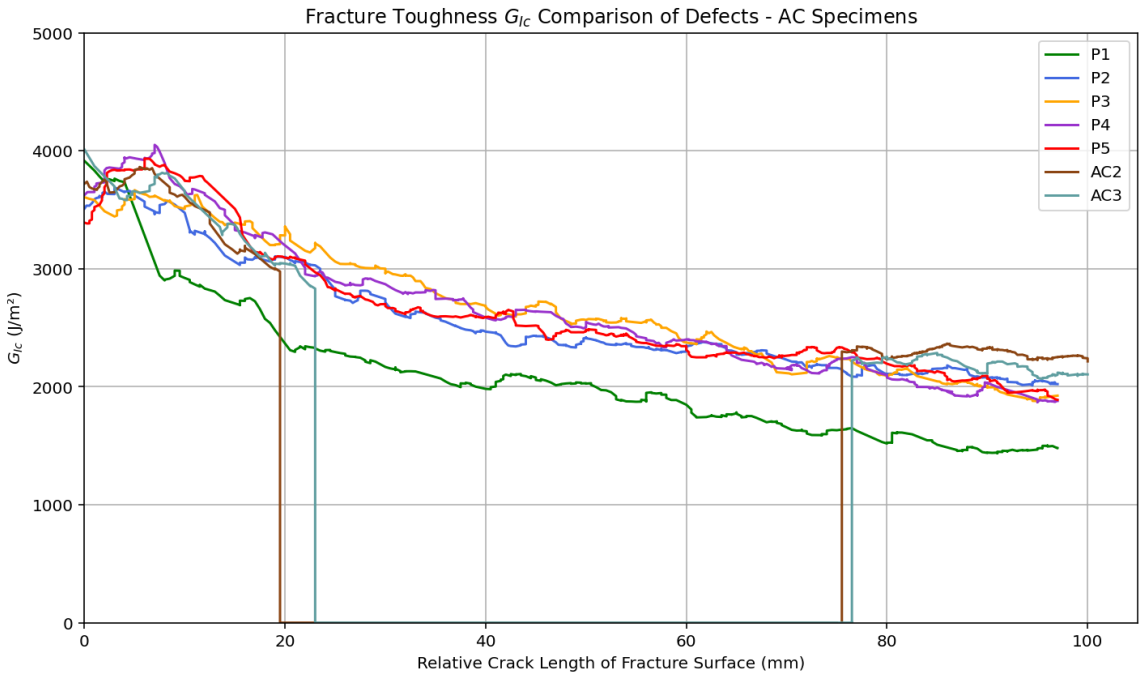

Figure 69: Comparison between P & AC Specimens - G_{1c}

Pristine vs. RA Specimens
Similarly, the RA Specimens have been plotted in Figure 70. To keep the figure legible, only P3 is plotted to represent an average pristine specimen. As can be seen, RA-U2 and RA-O1 failed at approximately the same point in the crack length, causing the G_{1c} to drop. These were the two specimens that did not experience early delamination prior to reaching the defective area, which was the case for RA-U2 and RA-U3. Prior to failure, each specimen starts at approximately the same fracture toughness as the pristine specimens, showing that the added contamination did not effect the onset of crack propagation itself for these specimens.

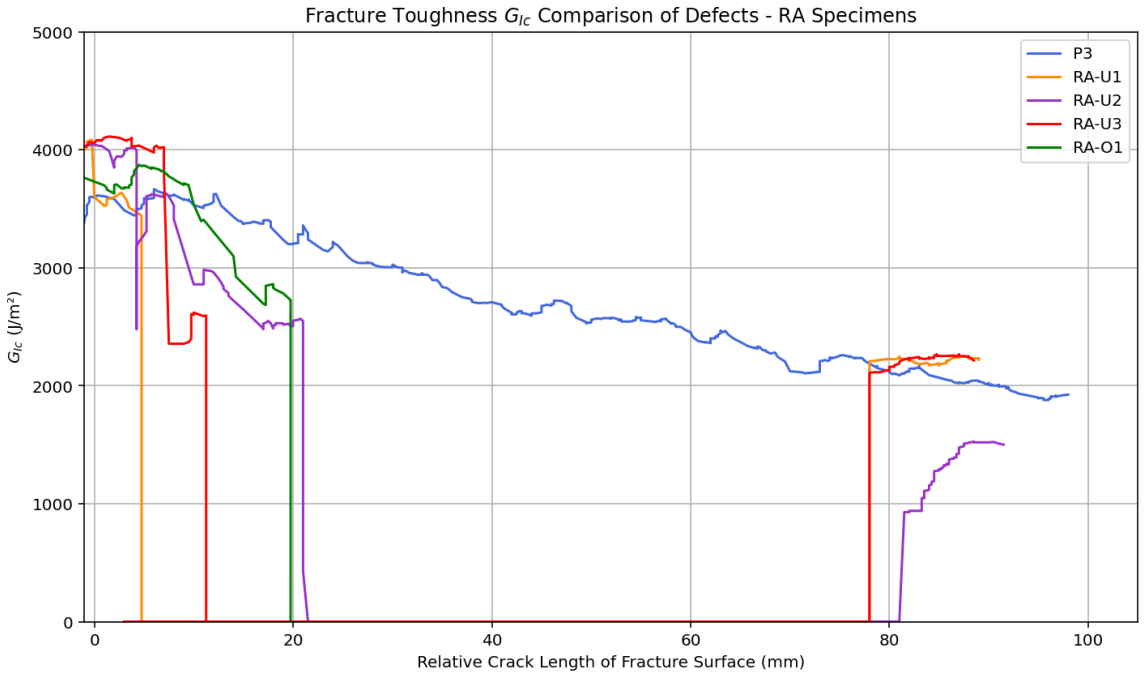

Figure 70: Comparison between P & RA Specimens - G_{1c}

8.4.2 Global Effective Fracture Toughness G_{eff} Comparison

In Table 10, the global effective fracture toughness of the different specimens can be found.

Table 10: Global Effective Fracture Toughness G_{eff} for different Specimens

Specimen	G_{eff} **[J/m²]**
P1	3514.05
P2	4673.54
P3	4718.40
P4	4468.92
P5	4665.61
AC1	2103.06
AC2	3937.91
AC3	3806.61
RA-U1	2754.16
RA-U2	2983.49
RA-U3	3180.69
RA-O1	2483.42

As can be seen, G_{eff} is consistent for the pristine specimens, besides P1 being lower. This was expected due to partial delamination failure. Overall, damage present in the adhesive layer reduces Effective Fracture Toughness. AC samples show a smaller reduction when compared to RA-U samples, but this can be attributed to the different failure modes present in these samples such as

interlaminar shear failure, as well as delamination present in the bond interface similar to P1.

The differences in G_{eff} between pristine and contaminated specimens are directly compared in Table 11. In this comparison, P1 is excluded due to aforementioned reasons to get an accurate Effective Fracture Toughness for a specimen failing cohesively. Negative percentages indicate the reduction in toughness compared to pristine specimens.

Specimen	G_{eff} [J/m^2]	% Difference from P
$P_{average}$ (P2-P5)	4408.10	0.00%
AC1	2103.06	-52.29%
AC2	3937.91	-10.67%
AC3	3806.61	-13.65%
RA-U1	2754.16	-37.52%
RA-U2	2983.49	-32.32%
RA-U3	3180.69	-27.84%
RA-O1	2483.42	-43.66%

Table 11: Comparison of G_{eff} values of specimens to average of P2 - P5.

In this comparison, all RA specimens showed significant reductions when compared to AC2 and AC3. However, this is likely due to more delaminations occurring for the RA specimen type rather than the difference in the type of contamination. This is reinforced by the fact that AC1 showed the biggest reduction of all specimen types due to onset of delamination.

The reduction of G_{eff} will be compared to the acoustic analysis of the different specimen types, to determine if effective fracture toughness can be related to acoustic energy measured during testing.

These results also show the effectiveness of release agent as a contamination. For the Force-Displacement data, fracture surface and fracture toughness analysis, it can be confidently stated that kissing bonds, undetectable using traditional C-Scan methods have been successfully introduced in the RA-U specimens.

8.5 Discussion

The mechanical testing of these adhesively bonded specimens has revealed insights on the fracture behavior of specimens containing different contamination types. The cohesive failure present in pristine specimens indicates that surface preparation and bonding of the samples was done effectively This resulted in an average effective fracture toughness of 4408 [J/m2] for pristine specimens showing the most cohesive failure. The mechanical data of these specimens will provide as a baseline used for the evaluation of the contaminated specimen types.

Specimens containing inclusive defects (AC) and release agent contamination (RA) showed significant reductions in fracture toughness. Both defect types showed regions of zero adhesion, corresponding to drop in loads and zero local G_{Ic}. RA specimens, intended to simulate kissing bond defects, showed mixed failure. These included delamination, interlaminar shear failure and adhesion failure.

Unintended failure modes likely resulted from inconsistent quality of the carbon composite, variability in preparation of the surface and introduction of the contamination. For example RA-O showed more adhesion failure, likely due to the excess of release agent applied in this production batch. Delaminations likely occurred due to insufficient composite quality and inconsistencies in the corona plasma treatment in particular, as previously described in section 7.

Both adhesion failure and delamination at the adherend adhesive interface show identical behavior in the force-displacement and fracture toughness data. Both failure modes result in rapid drop in measured load and calculated G_{Ic}. Images of the fracture surface are compared to this data, to distinguish between the two failure modes and their onset.

RA-U specimens show an increased stiffness and peak load before crack initiation. This can be the result of this batch of carbon having different properties due to uncertainties in the production process. A second origin could be the variability in pre-crack length due to inconsistent placement of the adhesive film.

It can be noticed that the local fracture toughness $G_{1c}(a)$ of RA-U3 increases before the contaminated region has ended in Figure 65c. This was caused by the crack tip being further than visually measured by the markings on the side of the specimen. It is suspected that white paint applied as a base for these markets was applied too thick, leading to the exact crack tip location being less visible.

Despite the limitations and variations of the results, the mechanical testing has resulted in a solid understanding of the failure modes of these specimens as a results of contamination, alongside local G_{Ic} and global G_{eff} fracture toughness metrics which can be used for the direct comparison between specimen defect types. In future research, refinements in the specimen production quality and surface treatment process can reduce delamination and interlaminar shear failure from occurring. This allows for more straightforward approach in analyzing the effects of contamination on adhesion properties.
Furthermore, more precise measurement techniques such as digital image correlation could be used to more accurately measure the crack growth. This could reduce the uncertainty of localizing onset of different failure modes.

9 Acoustic Results

The purpose of the AE testing done during testing is to monitor damage initiation, propagation and distinction between different failure modes. An attempt is made for to detect of badly bonded regions using wave transforms to confirm previous findings in literature [68]. In this chapter, AE signal data captured from tested pristine and defective specimens are compared.

9.1 Test Setup

Testing was conducted using an AMSY-6 (Vallen Systeme), 8 channel Acoustic Measurement System. A single Vallen VS900-M piezoelectric sensor was used. This sensor has a resonance sensitivity at 190 kHz and 350 [kHz]. The signal captured by the sensor was output through an external 34 [dB] AEP5 pre-amplifier. Parametric inputs from the testing machine allowed for data synchronization between the AE data and the load displacement values of the mechanical test. The parameters used in the AE acquisition can be found in Table 12.

Table 12: Acquisition parameters for AE measurements.

Acoustic Data Parameter	**Value**
Acoustic parameters sample rate	10 MHz
Acoustic transient waveforms sample rate	2 MHz
Threshold	40 dB
Digital band-pass filter	25-850 kHz
Pre-trigger time	200 μs
Post duration time	600 μs
Rearm time	400 μs
Duration discrimination time	400 μs

9.2 Data Processing

As described in section 4, there are several measurable metrics that describe an AE signal. Each measured signal crossing a set amplitude threshold will have all its properties measured and recorded. A digital filter of 40 dB is chosen to filter out any noise from the environment or disturbances. A Band-pass filter is used in the 25-850 [kHz] range, as this is the range where signals from similar tests are found [41] [68]. For the purposes of studying bondline failure, the signal energy, amplitude, peak frequency and hits are of most importance. Signal duration and arrival time aid in measuring crack propagation, but this would require multiple sensors and was done using visual crack monitoring instead. Crack propagation measurements would also require additional sensors to be used, so arrival time is of little use to this test. For each measured signal, the corresponding force and displacement measured by the mechanical test bench is are measured at a rate of 10 [Hz]. These force-displacement values are related to acoustic measurements as a parametric input.

9.3 Data Analysis

For analyzing the acoustic signatures per specimen type, certain specimens have been selected for more thorough analysis regarding acoustic hits and energy. These specimens are chosen for their distinct failure modes and to study different failure modes for identical specimens. Additionally, defective specimens will be compared to their pristine counterpart to highlight the effects of artificial defects on the acoustic characteristics.

9.3.1 Pristine Specimens

Of the Pristine Specimens, P2 showed mostly cohesive failure on it's fracture surface, with minimal delamination. It therefore acts as a baseline to identify acoustic characteristics that align with cohesive failure of the bondline.

In Figure 71, every signal measured is plotted as a function of peak amplitude [dB] and Crosshead Displacement [mm]. This visualizes all signals captured throughout the mechanical test and their respective amplitude.

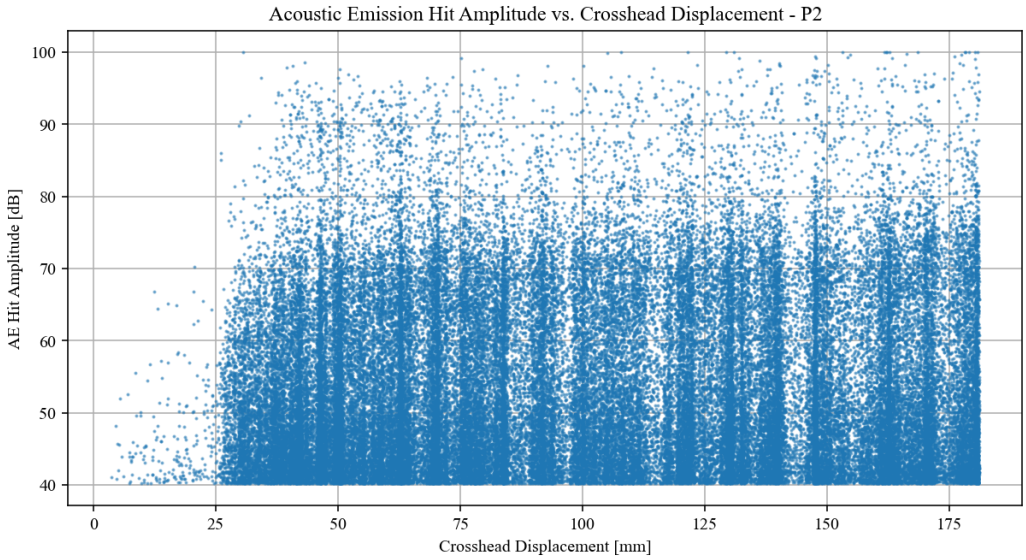

Figure 71: All Acoustic hits captured during testing - P2

It can be seen that until a certain point, there are virtually no acoustic signals recorded. The signals that are recorded likely originate from the carbon or adhesive settling, or minor cracks or voids present in either the adhesive or adherend cracking. The large increase in signals at approximately 25 [mm] is due to a crack originating in the adhesive layer and propagating. By overlaying the force-displacement curve, it can be seen that this point coincides with the point of maximum load, where crack initiation occurs, as can be seen in Figure 72.

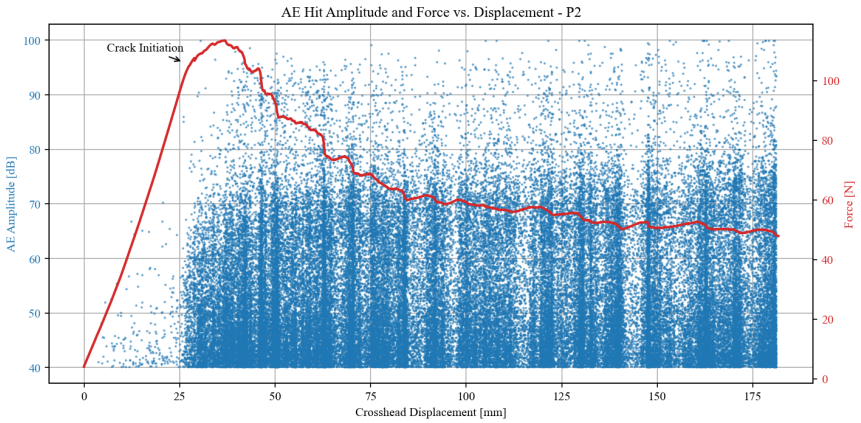

Figure 72: Increase in hits at point near maximum load

From these plots, it can be noticed that acoustic signals seem to arrive in periodic bands. When looking at Figure 72, a large increase in hits coincides with a drop in measured force. This reduction in load is as a result of a crack propagation. This means that when crack growth occurs more quickly, a burst of signals is released and detected. After crack propagation, it takes time for the specimen to be loaded again to a point where the load is sufficient enough such that crack growth can resume, resulting in minimal signals being emitted during this time. Hit burst can be seen highlighted in Figure 73.

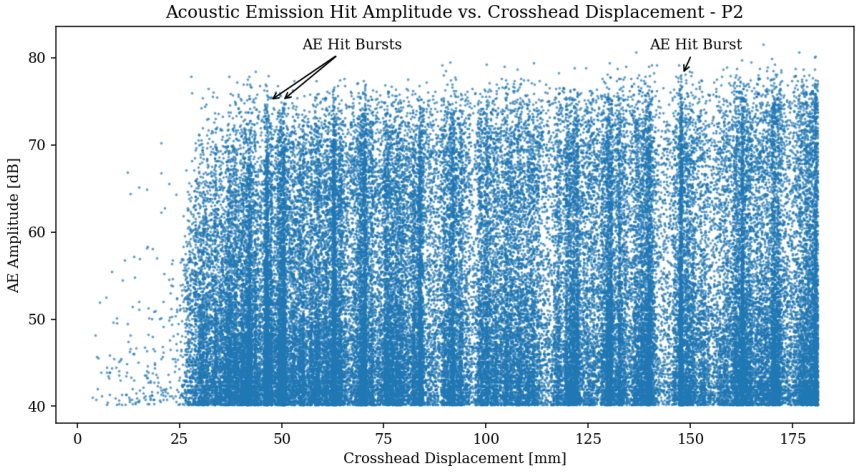

Figure 73: All Acoustic hits captured during testing - P2 - Highlighted AE Hit Bursts

Cumulative hits can give an indication of damage progression over the entire bondline based on minimal acoustic data. As can be seen, every drop in load, related to crack growth, coincides with an increase in total cumulative hits. One such instance is highlighted in Figure 74.

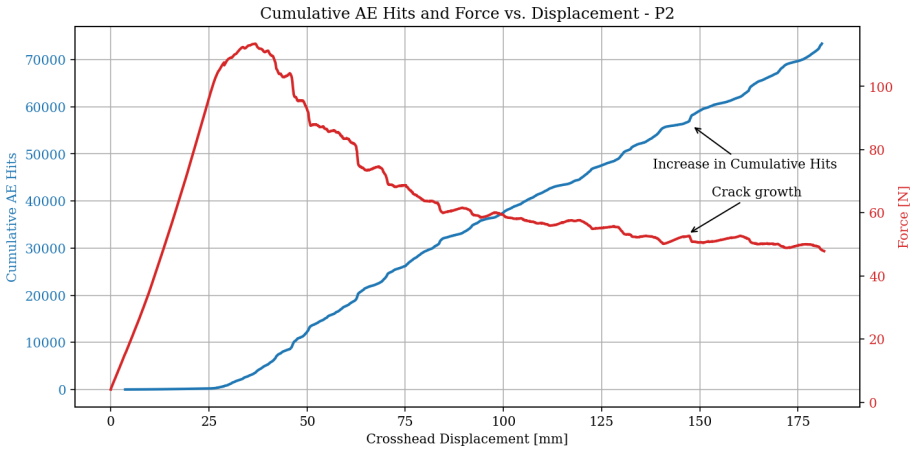

Figure 74: Total cumulative hits measured compared to force - P2

Next to amount of signal hits hits, cumulative energy is also computed. The energy of acoustic hits is measured in "energy units" or [eu], where 1 [eu] equates to $10^{-18}[J]$. The cumulative energy value will be used to compare the acoustic signature of signals and their respective G_{eff} computed in section 8. For P2, the cumulative energy can be found in Figure 75. As can be seen, cumulative energy rises steadily as the bond progressively fails.

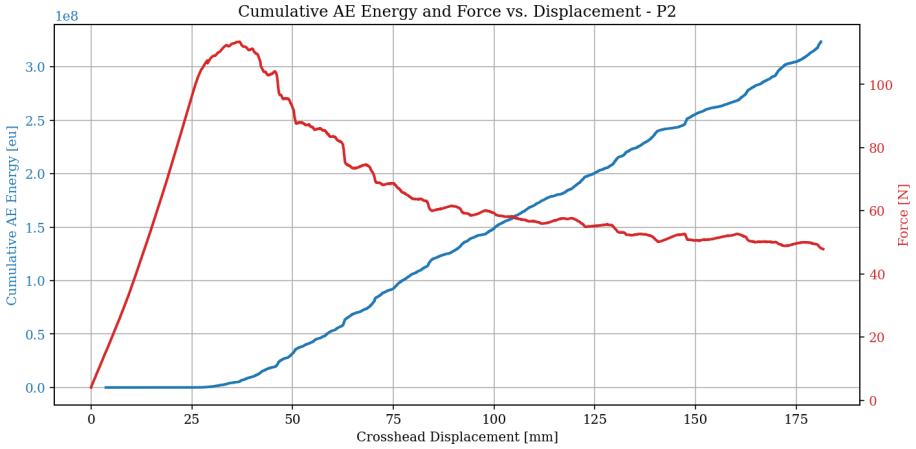

Figure 75: Total cumulative energy measured compared to force

Specimen P1 partially delaminated during testing. Therefore, specimen P1 and P2 are compared to study the variations in acoustic results as a result of this mixed failure mode. First, hit measurements of specimen P1 can be found in Figure 76.

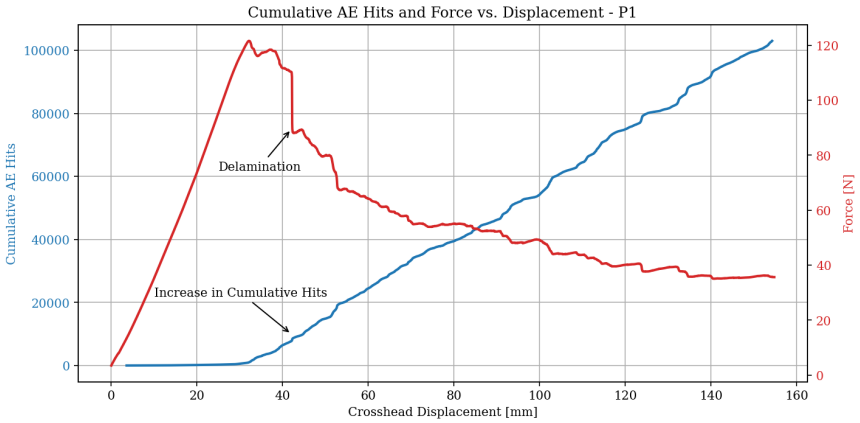

Figure 77: Cumulative Hits - P1

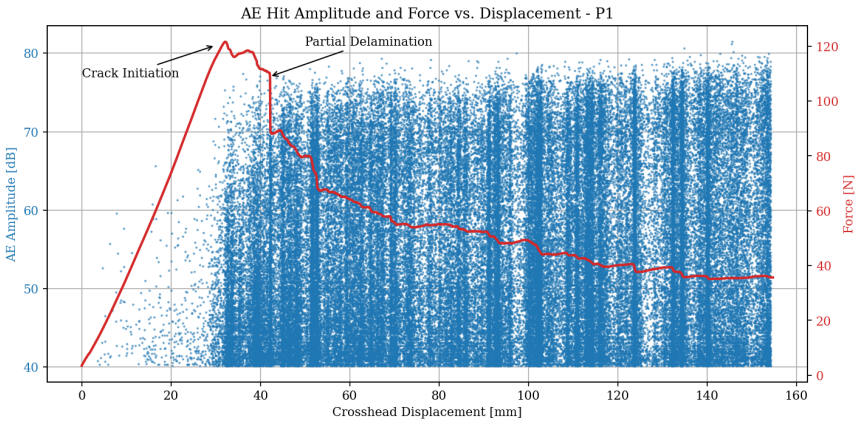

Figure 76: Hits detected during testing - P1

As can be seen, after a large drop in load at 42 [mm] crosshead displacement, coincides with a burst in hits. The impact of partial delamination on cumulative hits can be seen in Figure 77.

As can be seen, P1 starts with a similar trajectory. The delamination does show an increase in hits, but it seems to be minimal in its magnitude. The total amount of hits over the entire test duration however is noticeably higher. The cumulative hits and cumulative energy of P1 is directly compared to the other pristine specimens, which did not experience significant delaminations. The results of which can be found in Figure 78 and Figure 79.

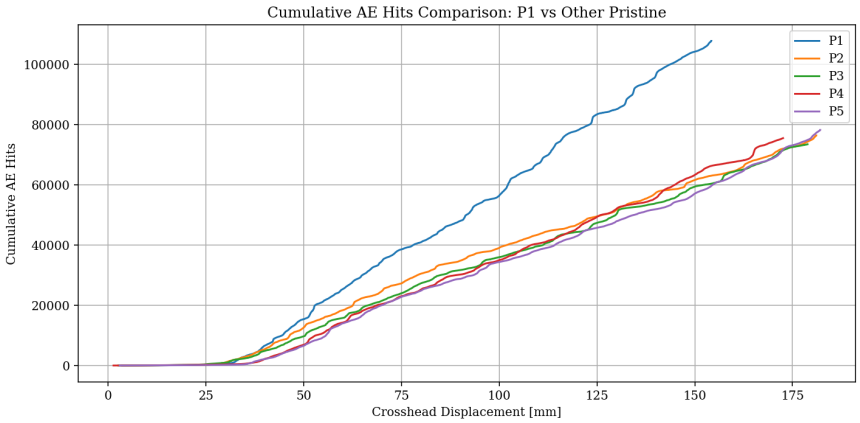

Figure 78: Cumulative hits comparison between partially delaminated specimen (P1) and cohesively failed specimens (P2-P5)

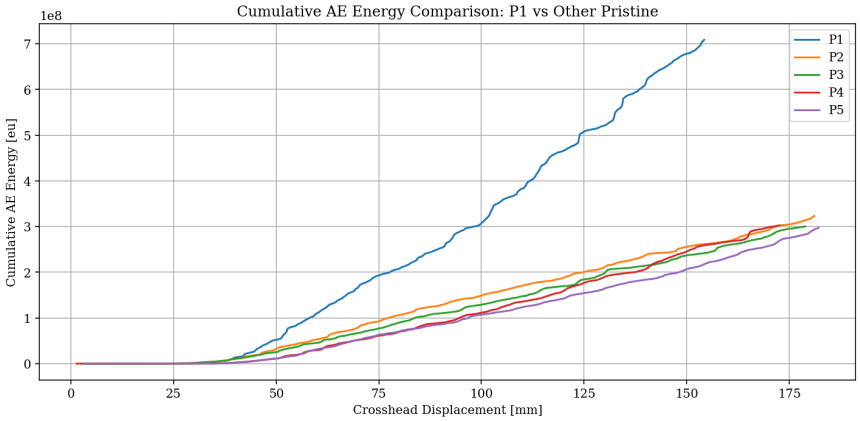

Figure 79: Cumulative energy comparison between partially delaminated specimen (P1) and cohesively failed specimens (P2-P5)

Here, clear differences between cohesive failure and delamination can be seen. P1 aligns closely with the other pristine specimens, up to the point where delaminations occur. This was shown to occur at approximately 40 [mm] crosshead displacement as per Figure 49. It can be noted that partial delamination results in a large increase in both cumulative hits as well as cumulative energy.

What also can be noted, is the close correlation of the other pristine specimens in terms of hits and energy. When cohesive failure is the dominant failure mode, total cumulative AE hits and energy measured shows little deviation from the mean, as can be seen in Figure 80 and Figure 81.

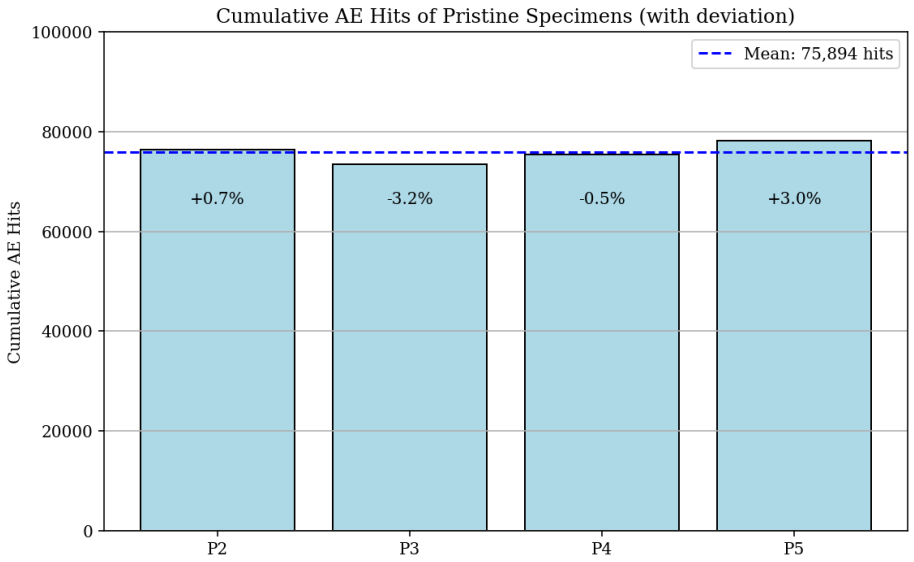

Figure 80: Deviation in cumulative hits - pristine specimens (cohesive failure)

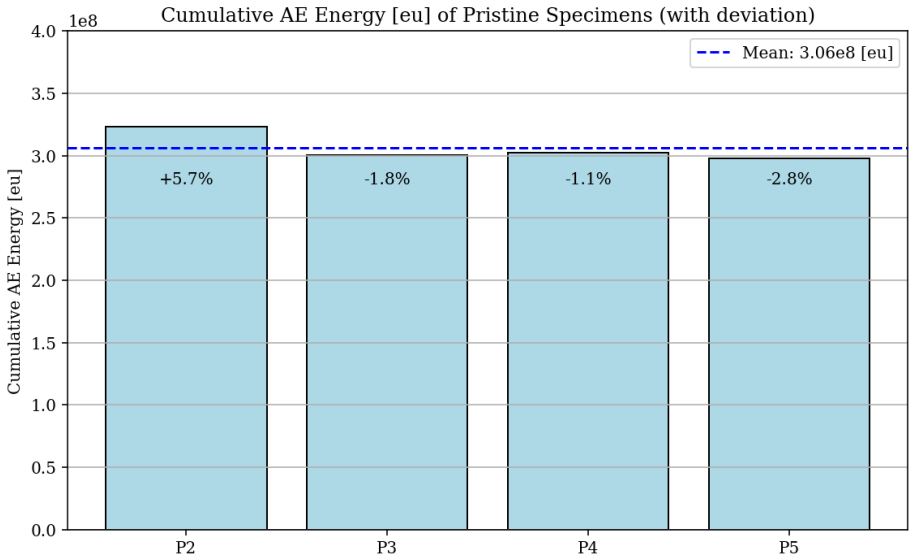

Figure 81: Deviation in cumulative acoustic energy - pristine specimens (cohesive failure)

When compared to the mean amount of cumulative hits and energy, P1 showed 42% more hits and 132% more acoustic energy measured when compared to the other pristine specimens which showed a more dominant cohesive failure mode.

9.3.2 Defected specimens

AC Specimens

AC2 is analyzed to show the effect on acoustic hits and their respective energy when an inclusion in the bondline is introduced, causing adhesion failure over the contaminated area.

Acoustic Hits
The total number of hits monitored from testing AC2 have been shown in Figure 82.

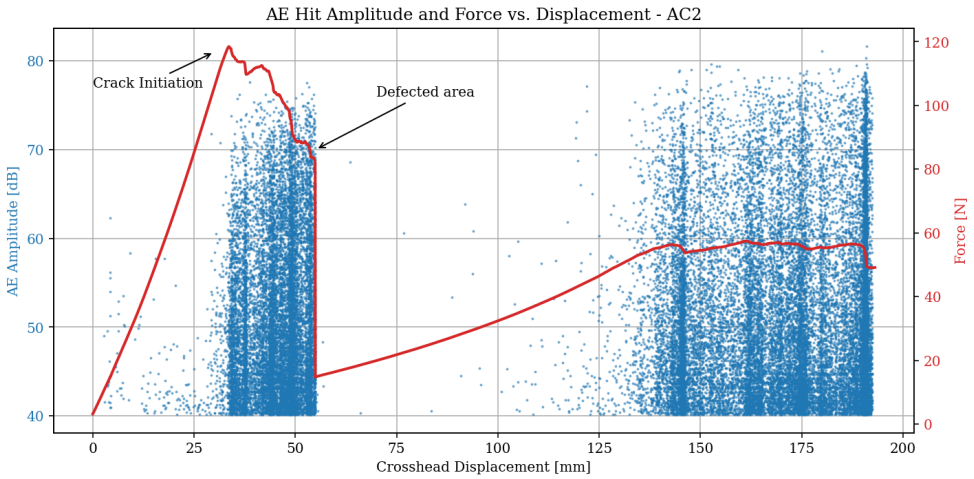

Figure 82: Hits detected during testing - AC2

As can be seen similar to the pristine specimens, few signals originate during the initial loading stage of the specimen. Only when the load is critical enough to initiate crack propagation and growth, do the number of acoustic hits increase. When the crack reaches the contamination at approximately 55 [mm] crosshead displacement, rapid failure occurs, after which almost no hits are detected. Only after the load reaches point where crack growth can resume do the number of hits increase. This period with very few hits detected can be visualized by considering the cumulative hits and cumulative energy, shown in Figure 83 and Figure 84 respectively.

Figure 83: Total cumulative hits measured compared to force - AC2

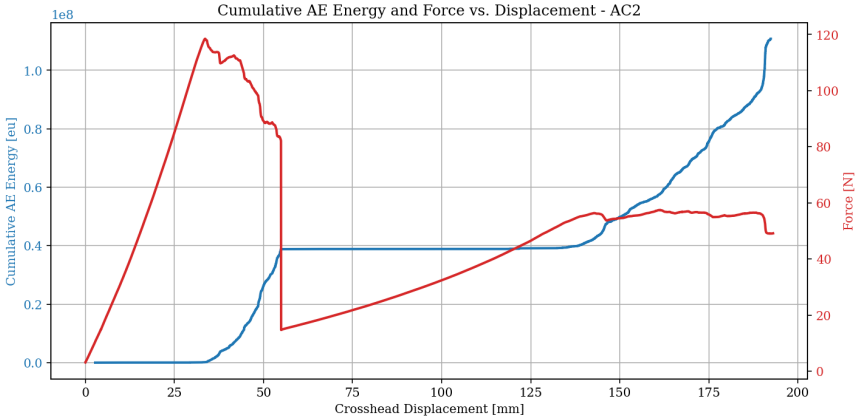

Figure 84: Total cumulative energy measured compared to force - AC2

In Figure 85 and Figure 86, cumulative hits and energy are plotted for all AC specimens. AC2 and AC3 closely resemble each other in their AE signatures, where AC3 has higher respective values due to it having a slightly longer crack growth period prior to adhesion failure at the defect region. Specimen AC1 failed prior to reaching the contaminated surface and thus shows much less activity in both comparisons.

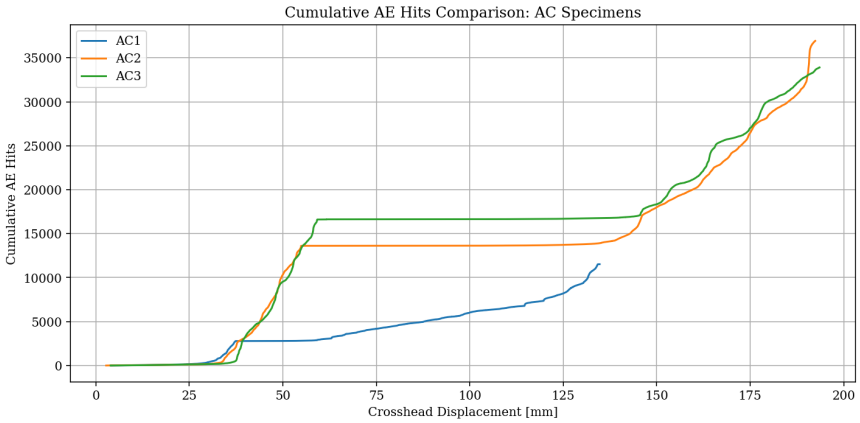

Figure 85: Cumulative hits comparison between AC specimens

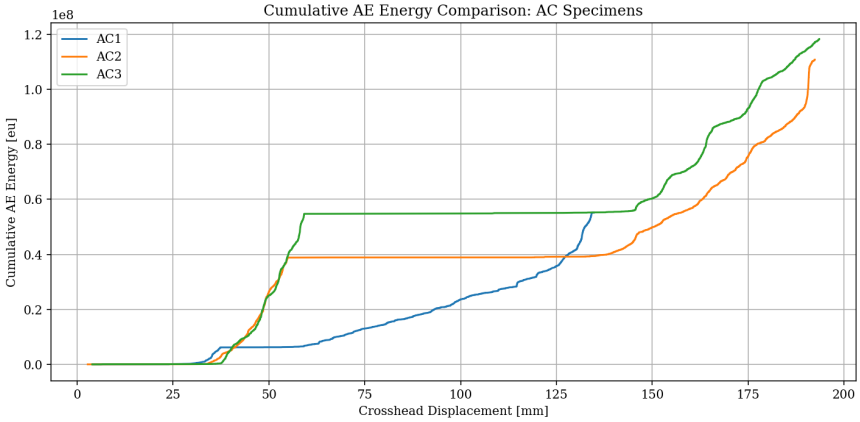

Figure 86: Cumulative energy comparison between AC specimens

RA-U Specimens

RA-U2 is analyzed first, as it had the cleanest cohesive failure. This specimen did however encounter inter laminar shear failure, an effect that can be seen in Figure 87.

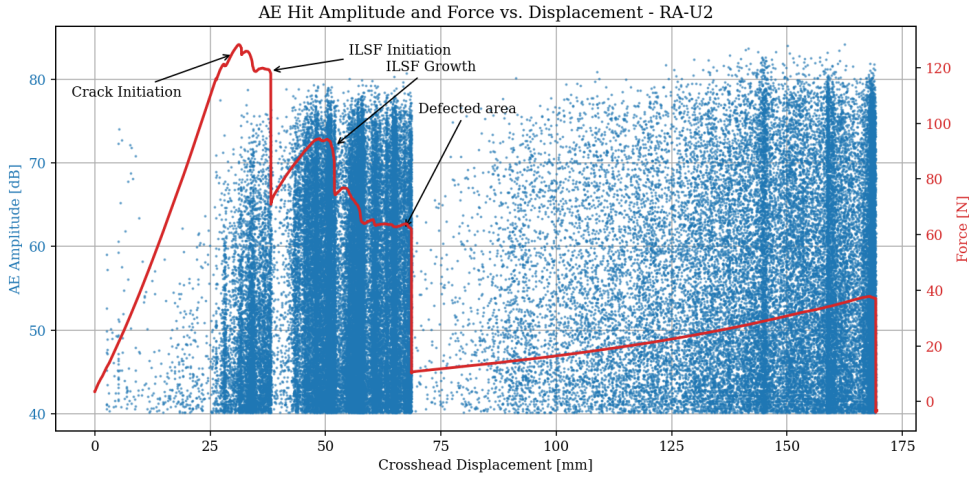

Figure 87: Hits detected during testing - P1

Hits start to be detected after crack initiation. This is followed by the initiation of inter laminar shear failure in the carbon adherend, which could be seen in Figure 63a. This failure is followed by less AE activity, due to the force increase needed to proceed with failure of the bondline. When the defective region is reached, once more complete failure occurs. However, during the reloading of the specimen there is noticeably more activity when compared to AC2. This is likely due to progression of the inter laminar shear failure in the composite adherend. The cumulative hits and energy can be found in Figure 88 and Figure 89 respectively. Once more, period of rapid crack growth or failure (such as ILSF) are seen to be followed by periods of stagnation. The upwards trending slope after initial failure from reaching the contaminated surface suggests hits originating from the ILSF continuing to grow while the bond layer remains stagnant.

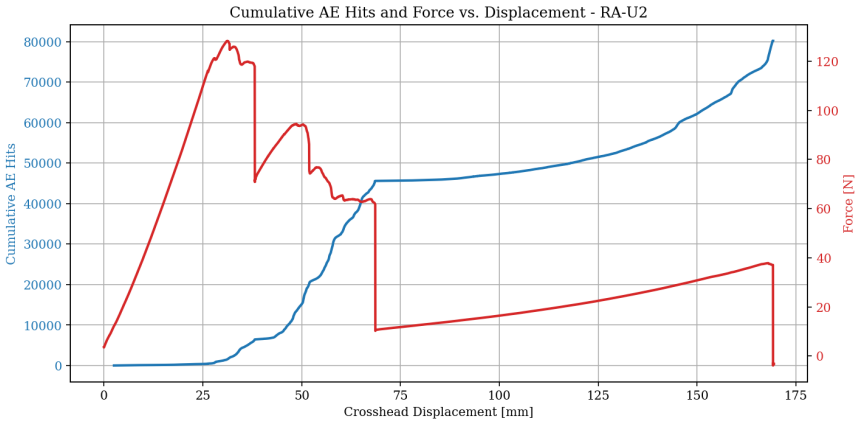

Figure 88: Total cumulative hits measured compared to force - RA-U2

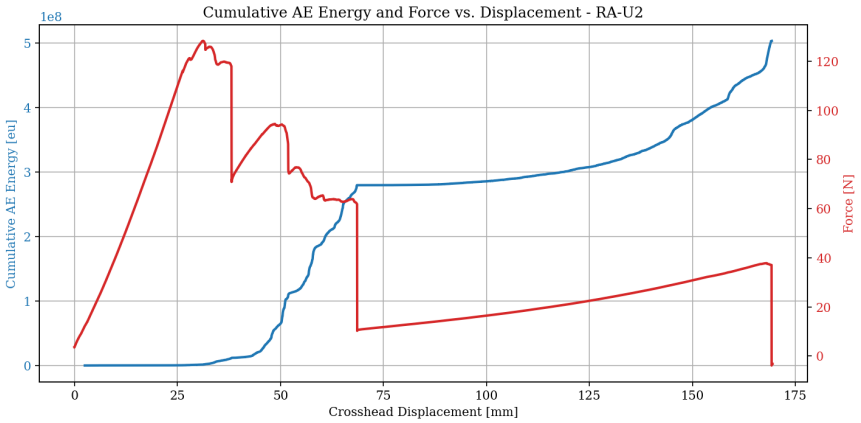

Figure 89: Total cumulative energy measured compared to force - RA-U2

Lastly, the results are shown for all RA specimens. RA-U2 shows the most hits and energy, likely due to it having the longest period of crack growth before reaching the contaminated region. All other specimens failed prior to reaching the contamination due to partial delamination. What can be noted is the upwards curving trend of both RA-U2 and RA-U3 after reaching initial failure. This trend has a different slope when compared to cohesively failing specimens. This can be explained as both RA-U2 and RA-U3 had ILSF occurring and growing during this stage of testing, resulting in more signals being detected while the crack in the bondline was not growing.

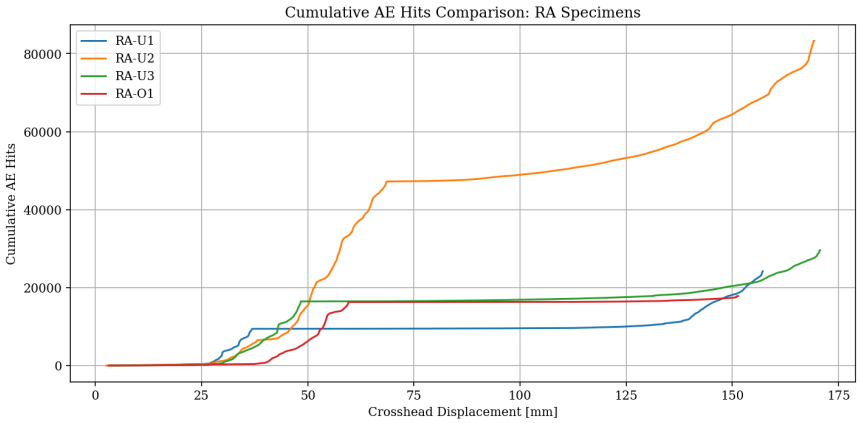

Figure 90: Cumulative hits comparison between RA specimens

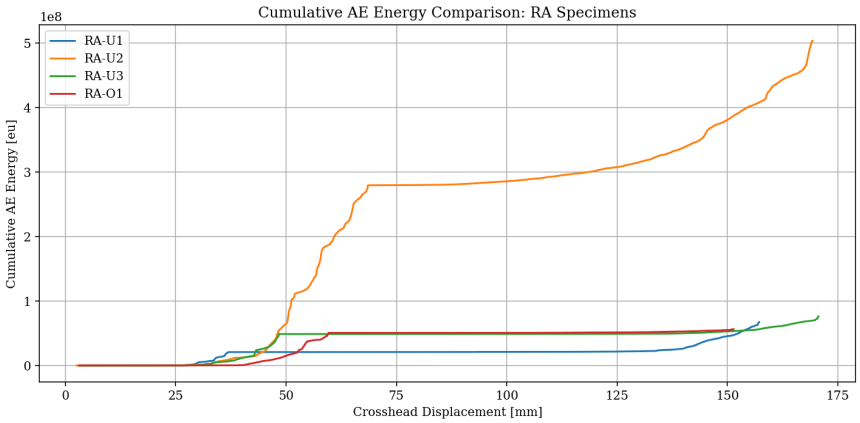

Figure 91: Cumulative energy comparison between RA specimens

9.3.3 Comparison Defects and Pristine

All pristine specimens similar results in terms of their acoustic characteristics regarding hits and energy, except P1, which started to deviate when partial delaminations occurred. After crack initiation, both specimens contaminated with adhesive film or release agent showed similar progression during cohesive failure of the bond. A comparison between specimens from each defect type can be found in Figure 92.

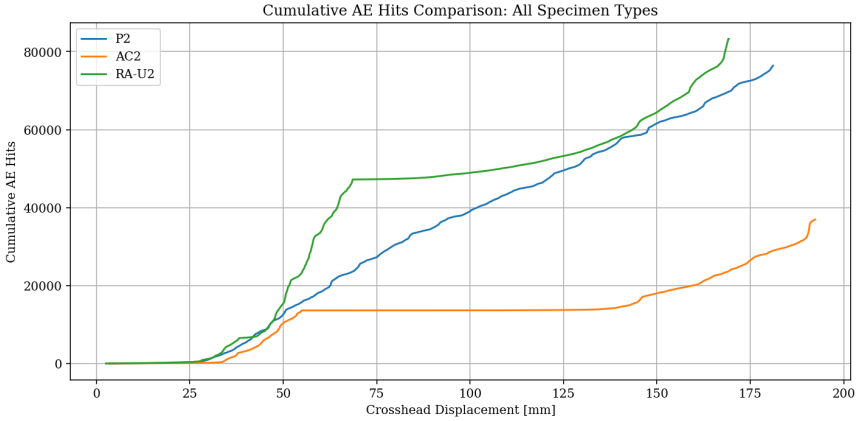

Figure 92: Cumulative hits comparison between specimen types

What can be noted is that RA-U2 has the largest increase in hits initially. This is likely due to both ILSF and cohesive failure occurring at the same time. ILSF also delayed crack propagation, meaning cohesive failure could occur for longer when compared to AC2, even though both specimens reached critical failure at the same bondline crack length. The curved increase in hits for RA-U2 is further highlighted to indicate incoming hits due to ILSF. A similar comparison is made for cumulative hits Figure 93.

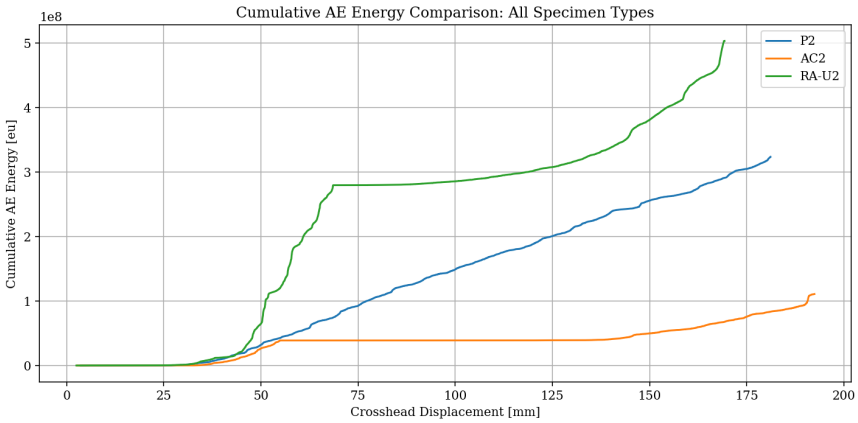

Figure 93: Cumulative energy comparison between specimen types

This comparison further reinforces the assumption that ILSF is causing RA-U2 to grow more rapidly in terms of activity, as the increase in energy is even more noticeable, starting at the point where ILSF was first observed. ILSF also seems to affect the increase of energy more than the increase of hits, which is similar to the increased activity of P1 when compared to the other pristine specimens when failing due to delamination. It is therefore likely that increased activity due to delamination at the adhesive adherend interface and ILSF have similar effects regarding increases in acoustic hits and acoustic energy measured.

9.3.4 Cumulative Acoustic Energy and Fracture Toughness

Cumulative Acoustic Energy is directly compared to global effective fracture toughness G_{eff}. It was hypothesized in section 6, that a bond containing defects would have a reduced G_{eff} and a reduced cumulative AE energy as results. This assumption was made based on the idea that contamination would result in complete bond failure, as not proper formation of chemical bonds could occur. Therefore, less bonds needed to be broken, resulting in less elastic waves to be measured by the AE system.

The G_{eff} and cumulative acoustic energy for the pristine specimens are outlined below.
As can be seen, the hypothesis does not hold. Firstly, specimen P3 has the highest G_{eff} out of all pristine specimens. However, it also shows the least cumulative acoustic energy measured. In addition, P4 has the lowest G_{eff} of all pristine specimens that failed cohesively, while having the highest acoustic energy. Therefore, this hypothesis does not hold, even when considering only the specimens that showed complete cohesive failure without the presence of artificial defects. Specimen P1, which partially delaminated showed a significant reduction in G_{eff}, while simultaneously showing a large increase in acoustic energy.

When it comes to defective specimens, a similar pattern emerges. RA-U2 showed 4x the number of hits and over 5x the amount of energy measured. However, its G_{eff} was comparable to the other RA specimens. The only slight correlation that could be made was AC1, which had only half the acoustic energy of AC2 or AC3 and also showed approximately half the G_{eff}. However, this results can not be seen as definitive due to the complex failure it experienced, leading to premature failure.

It can for these reasons be stated that this method of comparing acoustic cumulative energy and global fracture toughness G_{eff}, does not hold. What can be said however is the consistency of the results when it comes to consistent failure. All pristine specimens, except P1, showed highly similar acoustic responses in terms of hits and energy. Besides the energy seemingly be less when compared to G_{eff}, the differences in G_{eff} and acoustic energy remain small, meaning that certain pristine bonds can be associated with a certain acoustic hit, energy and G_{eff} range with high accuracy. This means that when measuring a specimen with possible defects, any divergence from the expected hit and energy trend-line could act as an indication of bond defects, where increased activity might signal delamination or ILSF and decreased or no activity is caused by adhesion failure, meaning a large crack event may have occurred.

9.4 Acoustic Emission Clustering

While identifying the number of signals and their corresponding energy, more aspects of the acoustic waves can be analyzed to group them and associate certain failure modes with certain signals. This can be done using Acoustic Emission Clustering approach. Such an approach can help identify patterns in the acoustic hits, besides energy and amplitude. This is particularly applicable for trying to find characteristic frequency bands which can be linked to types of failure modes, such as cohesive failure or delamination.

9.4.1 Unsupervised Clustering

For each acoustic signal, two features were extracted from each waveform:

- **Signal Energy:** Computed by taking the sum of squared amplitude.
- **Peak Frequency:** Computed by performing a Fourier Transform on each signal.

These signals were clustered and grouped based on these two main parameters. In this clustering approach, frequency is being given a higher impact as distinct failure modes are mainly frequency dependent. The AE hits were then clustered based on these features using the following techniques:

1. **Principal Component Analysis (PCA):** Here, the data is simplified by compressing the frequency and energy component into variables that can be directly compared. In this step, energy impact is reduced to make the results more frequency dominant.
2. **Self-Organizing Map (SOM):** Next, hits with similar frequency and energy components are mapped on a 2D grid, creating groups of similar data points.
3. **K-Means Clustering:** Finally, the data is grouped into clusters, where the groups are formed by minimizing the variance within each group, essentially grouping acoustic hits with similar properties.

The clustered the hits were plotted based on they peak frequency and amplitude. Examples of the results can be found in Figure 94.

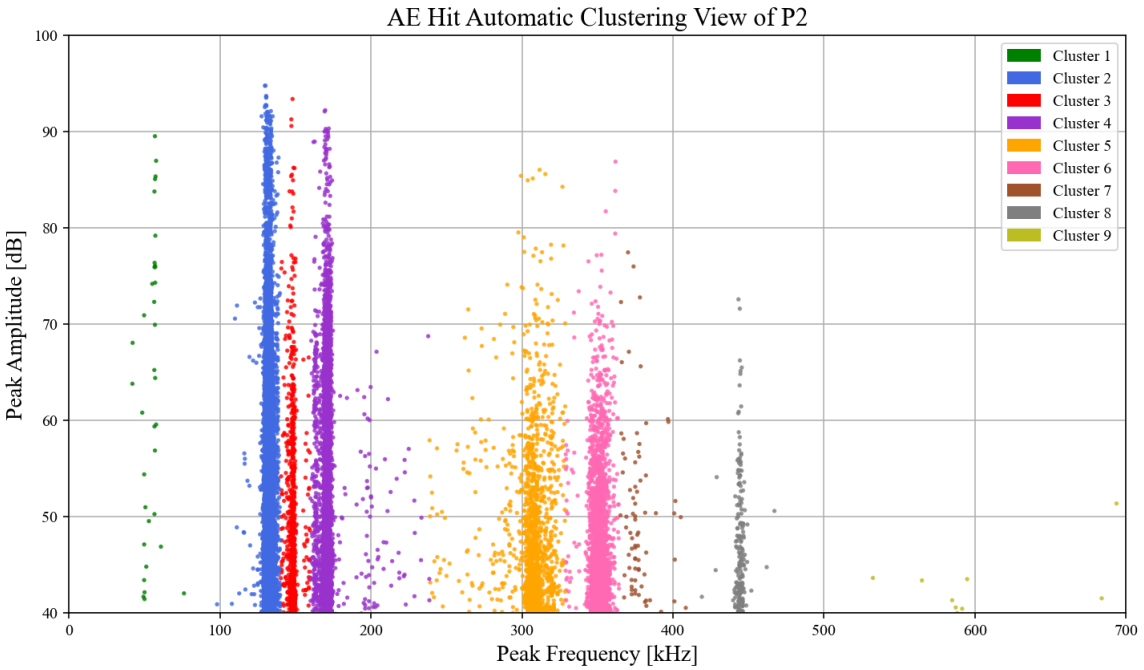

Figure 94: Acoustic signals grouped using a Automatic Clustering Approach - P2 (10.000 signals)

The plot reveals that the acoustic signals indeed appear in clusters around certain peak frequencies. In the case for P2, a total of 9 clusters were identified. However, the unsupervised clustering method resulted in a large variation in the number of clusters for specimens with identical defects. For example, the same algorithm identified 6 cluster for P3 and 7 clusters for P1, as can be seen in Figure 95.

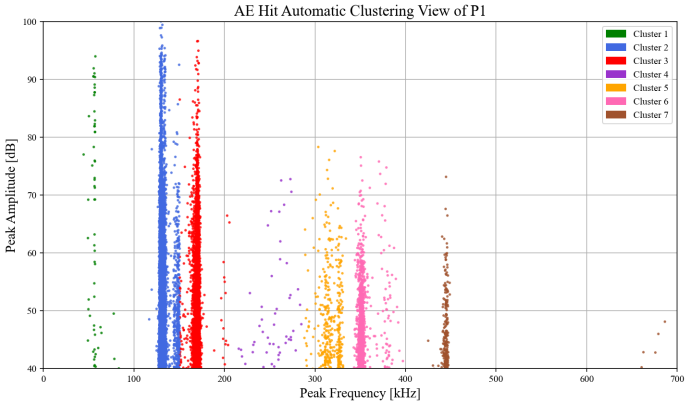

(a) Automatic clustering - P1

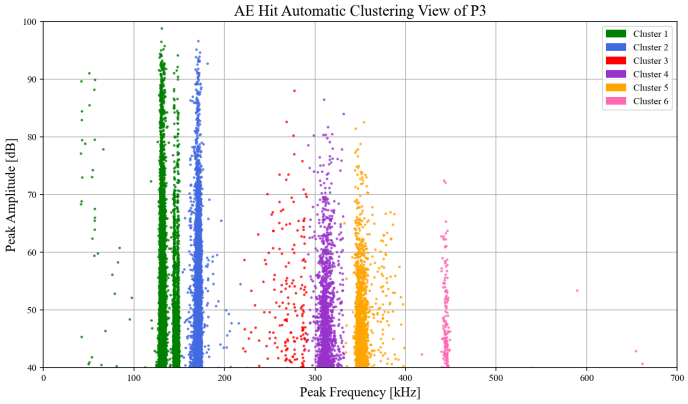

(b) Automatic clustering - P3

Figure 95: Comparison of unsupervised AE clustering for specimens P1 and P3.

While each specimen shows a different amount of clusters, the same frequency bands can be found in every specimen. Meaning each identified cluster is present in each specimen to some extend. The large variation in the number of clusters identified using this approach therefore made the comparison between specimens and comparison between defect types difficult. Due to the consistency peak frequency bands, it was therefore decided that the analysis was shifted to a manual clustering approach instead, where specific frequency bands were designated manually. These clusters were based on the prevalent clusters identified from the automatic clustering analysis, containing all main frequency bands observed across all specimen types. By observation, it can be noted that the following groups of signals, based on their peak frequency, appear consistently across the different specimen groups:

- Cluster 1: $<$ 100 kHz
- Cluster 2: 130 kHz (100 - 155 kHz region)
- Cluster 3: 170 kHz (155 - 180 kHz region)
- Cluster 4: 180 - 300 kHz region

- Cluster 5: 320 kHz (300 - 340 region)
- Cluster 6: 350 kHz (340 - 400 region)
- Cluster 7: $>$ 400 kHz

By manually grouping the clusters, the inconsistency in the number of clusters and their designation was removed. The results of using this approach of frequency based clustering per defect type can be found in Figure 96, Figure 97 and Figure 98.

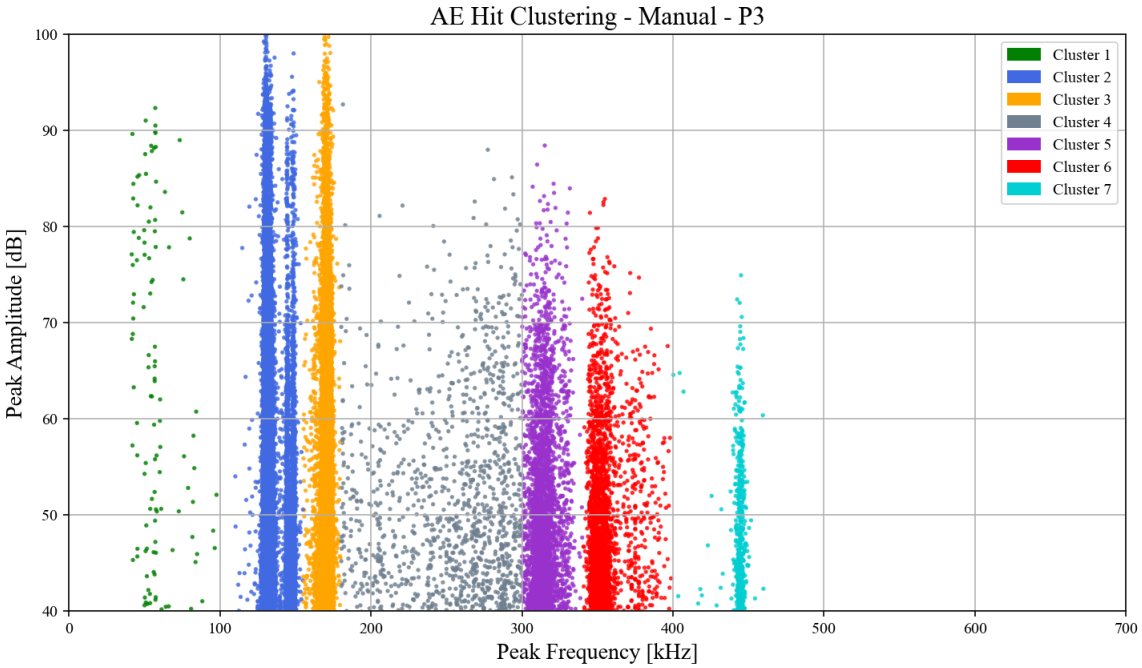

Figure 96: Clusters of P3

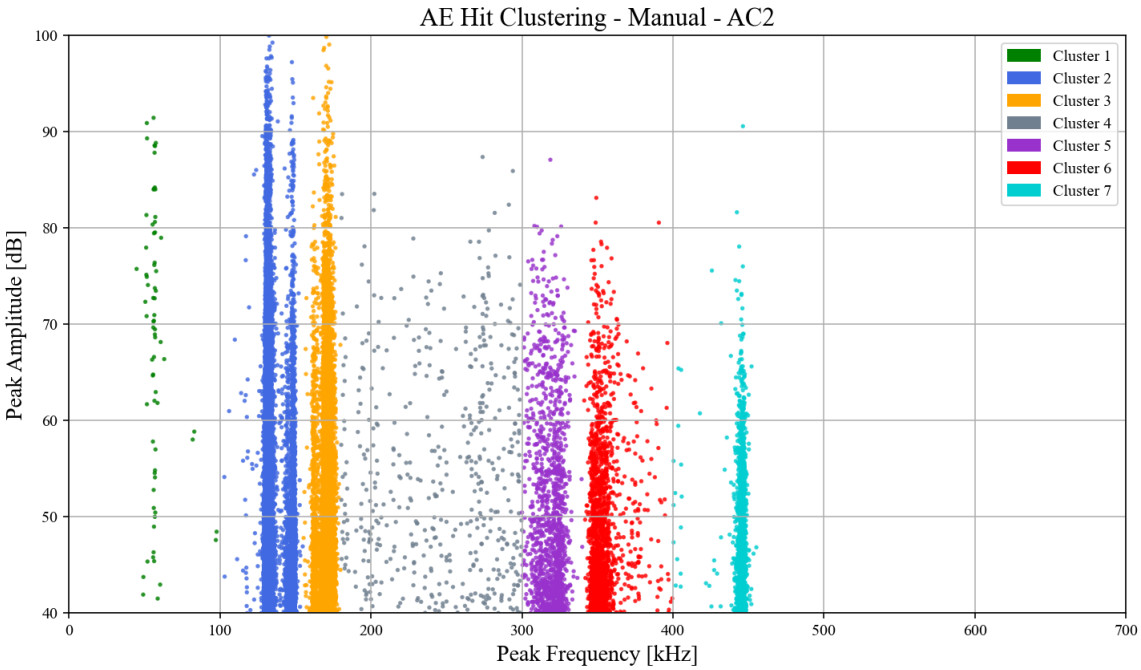

Figure 97: Clusters of AC2

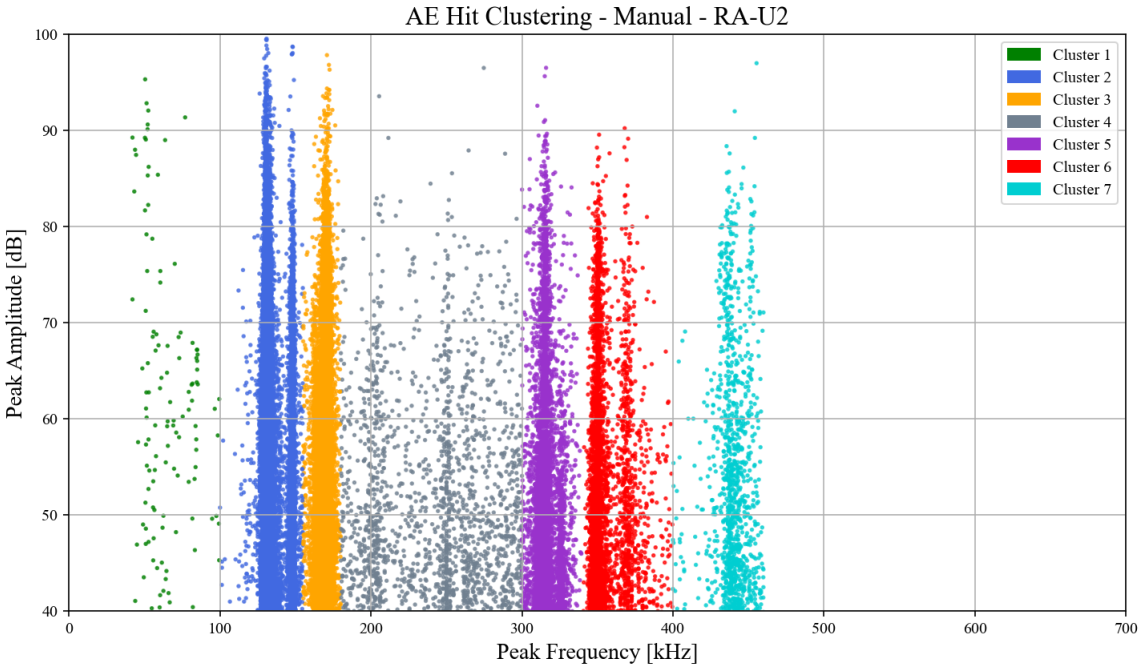

Figure 98: Clusters of RA-U2

Differences in the prevalence of clusters can be visually observed in the figures above. For example, RA-U2 shows more activity in Cluster 6 and Cluster 7 when compared to the other two specimens. AC2 shows a clear reduced activity in Cluster 4, in comparison to the other specimens. However, a quantitative assessment of the number of hits is needed to determine more specific characteristic frequency ranges for each specimen defect type.

For a direct comparison, the hits per cluster are counted and displayed in a column-normalized heatmap, which can be found in Figure 99. Here, each column corresponds to a specific frequency cluster. Each cell indicates the percentage of all hits that occur in this cluster for a given specimen. In other words, by normalizing the values per cluster, the relative contribution of each specimen to that frequency cluster can be assessed.

Higher percentages, indicated by darker colors, signify that this specific specimen has more of its signals occur in this cluster compared to other specimens. It does not automatically imply that this cluster is then also dominant over all signals of this specimen, but rather that this cluster is more active compared to other specimens. This normalization approach allows for a comparison between specimens, independent of the total number of hits measured.

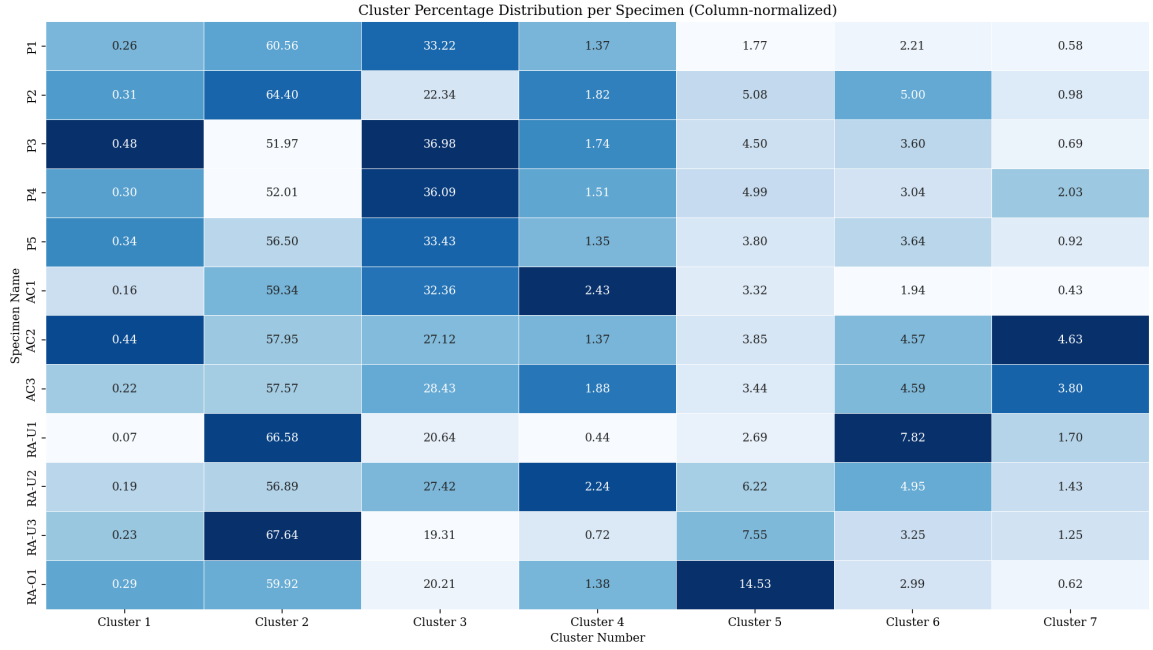

Figure 99: Heatmap of all clusters for all specimens

To further outline how this heatmap should be interpreted; specimen P3 has a relatively high presence of Cluster 1 compared to the other specimens, indicated by the dark blue coloration. However, it should be noted that Cluster 1 is only assigned to 0.48 % of all signals detected from P3. Similarly, while P3 shows the lowest prevalence of Cluster 2 at only, 51.97 %, the total number of signals assigned to this cluster is much higher compared to the number of signals in Cluster 1.

9.4.2 Identification of Failure Modes using Manual Clusters

Cluster 1 (<100 kHz)

Accurate identification of Cluster 1 is difficult, seeing as this cluster contains at most 0.5% of all signals, as is the case for P3. Additionally, the VS900-M sensor used is less sensitive at these lower frequency ranges, making identification of where and when they occur hard, as many signals that may occur are likely to be missed.

This cluster is likely related to matrix cracking or early cohesive failure or cohesive failure initiation. All pristine specimens show relatively high presence of Cluster 1. Additionally, AC2 shows the highest percentage of Cluster 1 of all AC specimens, where AC2 was the only one to fail fully cohesively prior to reaching the contaminated area. This is also the case for RA-U1, which out of all RA-U specimens prematurely failed the soonest. It also failed the most premature of all specimens tested. Cluster 1 signals less presence in these specimens, because they did not have the time under failure to generate these signals. What exactly causes these signals however, can not be confidently stated.

Cluster 2 (130 kHz)

Cluster 2 can more confidently be identified as **Delamination**. Firstly, both Specimens P1 and P2 shows a more prevalent Cluster 2 when compared to the remaining pristine specimens. Both these specimens show the most delamination at the adhesive interface. P3 and P4 showed the lowest activity in this cluster of all specimens, and also showed the least delamination on their fracture surface. Similarly RA-U1 and RA-U3 show higher delamination when compared to RA-U2, where delamination was less present before rapid failure due to the defected area.

Cluster 2 is the most present cluster out of all clusters for all specimens. It would therefore be difficult to assume Cluster 2 is indicative of delamination, when P3 and P4 which show no delamination still show over 50% activity in Cluster 2.

The confidence in identifying this cluster as delamination stems from the results from additional specimens that were tested. Specimens contaminated with Mist (a fine layer of sprayed water) on the adhesive interface were produced and tested. This contamination was applied in the exact same area as RA-U and AC specimens. The intention was in using Mist as a surface contamination that would possibly promote adhesion failure. However, almost complete delamination was the resultant failure mode during testing. It was therefore decided to not include these specimens for further analysis, as at this stage of research the reproduction of kissing-bond like defects had the main focus. These specimens were designated M, where 3 specimens were mechanically tested while acoustic measurements were taken. The dominant delamination failure can be seen in Figure 100.

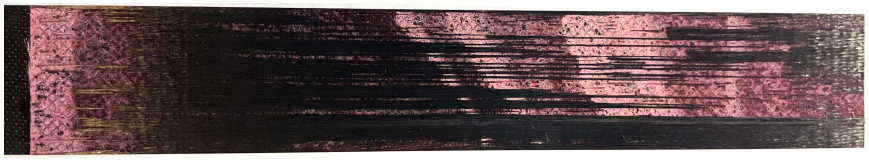

(a) M1 fracture surface

(b) M2 fracture surface

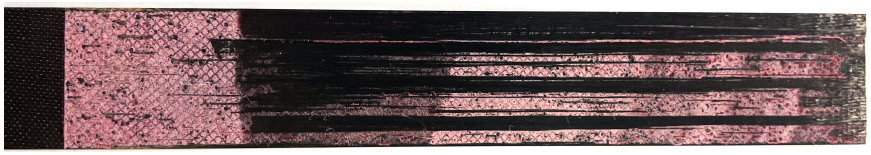

(c) M3 fracture surface

Figure 100: Fracture surfaces of specimens M1, M2, and M3.

While having been excluded from most mechanical and acoustic analysis, their measured signals reveal insight on the identification of Cluster 2, as can be seen below in Figure 101. Here, Mist contaminated specimens are included in the heatmap comparison.

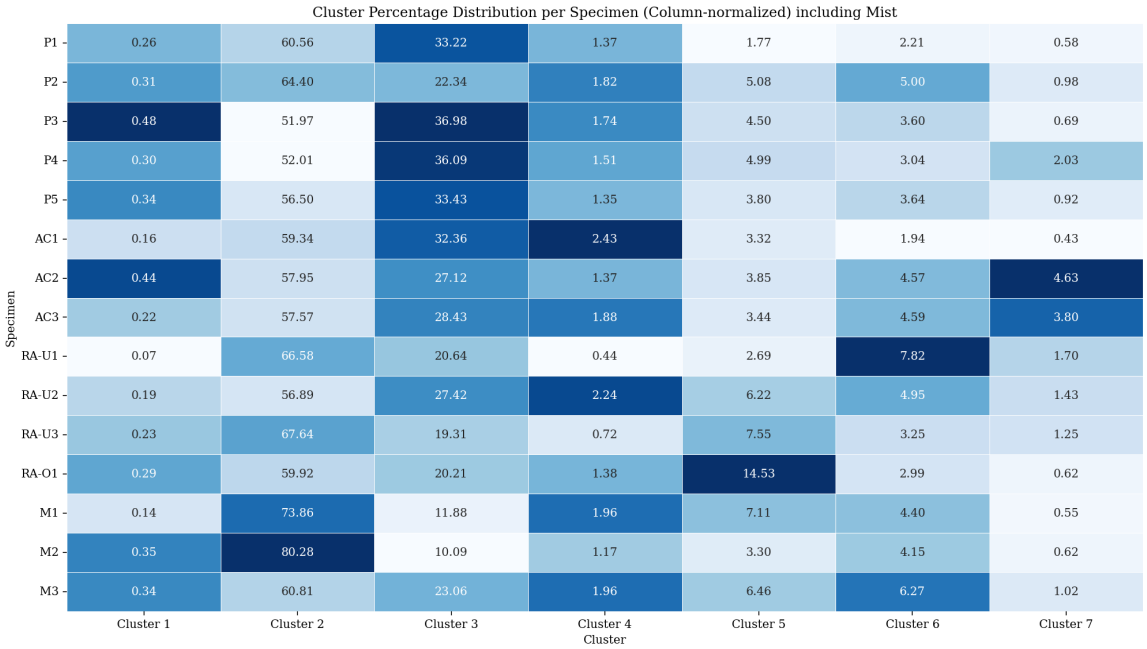

Figure 101: Heatmap of all clusters for all specimens (Mist added)

As can be seen, Mist specimen 1 and 2 (M1 & M2) show exceptionally high activity in Cluster 2. Mist specimen 3 (M3) shows the least activity of the M specimens, but comparably still high compared to other specimens. The fracture surfaces of these specimens show that indeed M1 and M2 failed the most through delamination out of all specimens tested. M3 experienced a more mixed failure and failed more cohesively. It more closely resembles P1, which can be found in Figure 50a. Additionally, both P1 and M3 show near identical activity in this cluster.

Cluster 3 (170 kHz)

Subsequently, this cluster is associated with cohesive failure. This is due to their high representation in pristine specimens. P3, which is seen to have the most cohesive failure on its fracture surface, also has the highest representation of Cluster 3. Additionally, M3 showed 2.5 times the activity when compared to M1 and M2, the opposite of Cluster 2. This further reinforced the notion that Cluster 2 and Cluster 3 are seemingly opposites, indicating delamination and cohesive failure respectively. This increased activity of M3 was further motivation to include the Mist contaminated specimens in this analysis, despite their under representation throughout other parts of the research.
RA-U2 shows the most activity in Cluster 3 of all RA specimens, while also having the most cohesive failure. For example, it failed more cohesively compared to RA-U3, which had a similar test duration. While RA-U1 shows some activity in Cluster 3, despite having minimal cohesive failure, it must be restated that RA-U1 failed destructively at an early stage. It failed rapidly, where in early stages cohesive failure did occur, making it a high relative percentage despite being largely absent from its respective fracture surface.

Cluster 4 (180 - 330 kHz region)

This cluster is more difficult to identify. This region is less sharply defined as other clusters. Additionally, no real pattern can be found in the prevalence of these signals when comparing its occurrence between specimen types. It is likely broadband scatter, caused by wave interactions or more complex wave mechanics caused by lower and higher frequency waves interfering.

Cluster 5 (320 kHz)

This cluster is most likely related to adhesion failure, or waves interacting with a poorly adhered region. The main reason for this characterization is RA-O1, which has the largest Cluster 5 contribution of all specimens by a large margin. The reason is while RA-O1 shows adhesion failure more prominently when compared to other RA specimens it how the contamination was applied. By contaminating only a part of the width of the specimen, the specimen failed both cohesively and adhesively at the same time. For RA-U specimens, adhesion failure onset rapid and sudden, causing the crack propagation to completely skip this contaminated region when reached. Despite this, RA-U2 and RA-U3 still show high activity in this cluster, which were the only other specimens failing adhesively due to release agent. RA-U1 failed destructively, not long after crack initiation. This specimen therefore did not have the opportunity to reach the contaminated region, therefore also showing very low activity in Cluster 5.

Cluster 6 (350 kHz)

Cluster 6 is likely the result of fibers breaking. This can be from either carbon fibers breaking at the adherend interface, or it could originate from the adhesive carrier fibers breaking while cohesively failing. Fiber bridging was observed, most noticeably while testing specimen P2. Additionally, specimen AC2 and AC3 had visible fiber bridging, before a different failure mode could occur. In general, specimens with more cohesive failure, show a more dominant Cluster 6. An image of fiber bridging occurring during testing can be found in Figure 102.

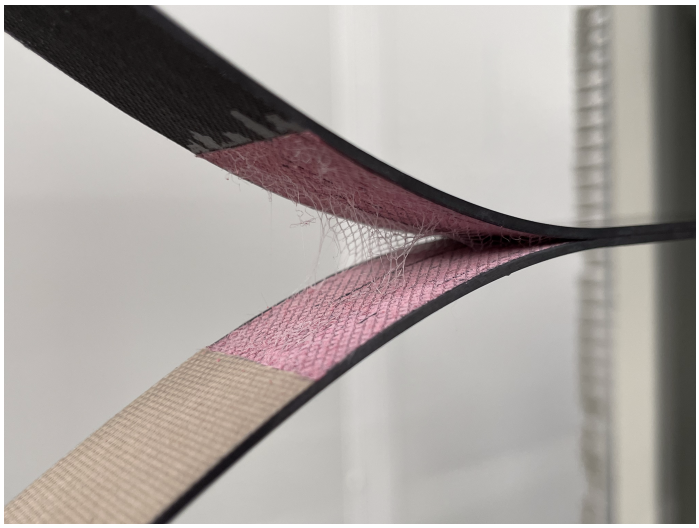

Figure 102: Bridging of Adhesive Carrier fibers

The reason for the large presence of this failure mode in RA-U1, can not be confidently stated. This

specimen experienced early failure, meaning fiber bridging did not have the opportunity to occur in any significant amount. It is possible that this specimen delaminated, combined with carbon fibers breaking at the adhesive adherend interface. This was not confirmed using microscopy methods, which could further reaffirm the origin of these signals.

Cluster 7 (450 kHz)

This cluster is most prevalent in specimens AC2 and AC3. These were the only specimens with inclusions, where the crack front reached the inclusion progressive. Specimen AC1, the only other specimen containing this inclusion, fail too early and as a result, the inclusion defect was not reached before being passed entirely.

Due to the fact that this cluster is also present in other specimens, it can not be stated that the inclusive adhesive film was the origin of these signals. Rather, the presence of the film seems to increase its activity, possibly due to more complex wave interference caused by an inclusive piece of protective film, interacting with waves progressing through the adhesive adherend interface.

9.5 Wavelet Transform

Wavelet transforms can be used to study the frequency components of a signal, as a function of time. This helps in identifying not only which peak frequencies occur and with their corresponding amplitudes, but also other high energy frequency components that might be missed when only regarding peak frequency or peak amplitude. An example of a Wavelet Transform can be found below in Figure 103, using a Morlet wavelet.

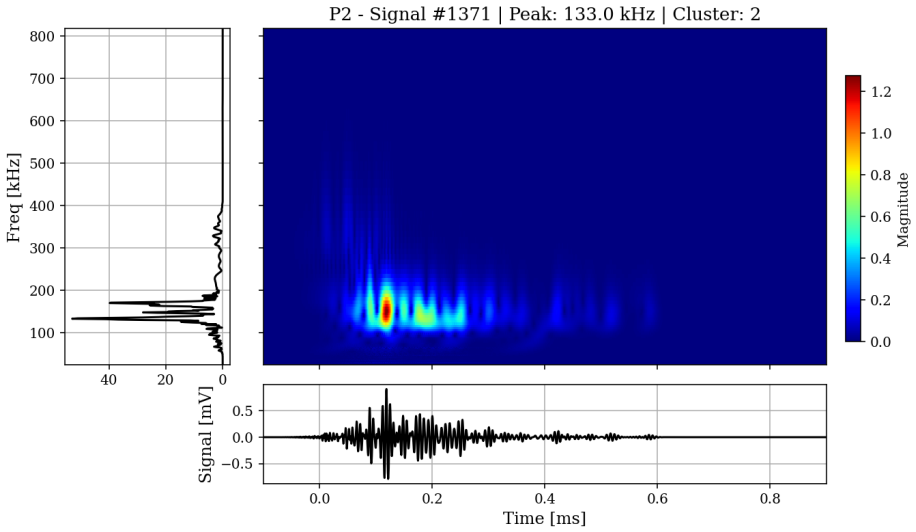

Figure 103: Morlet Wavelet Transform of an Acoustic Signal - P2

This signal corresponds to Cluster 2, with a clear peak frequency at 133 [kHz]. Similarly, other transforms can be made of signals found in other clusters, such as Cluster 3 in Figure 104 and

Cluster 6 in Figure 105.

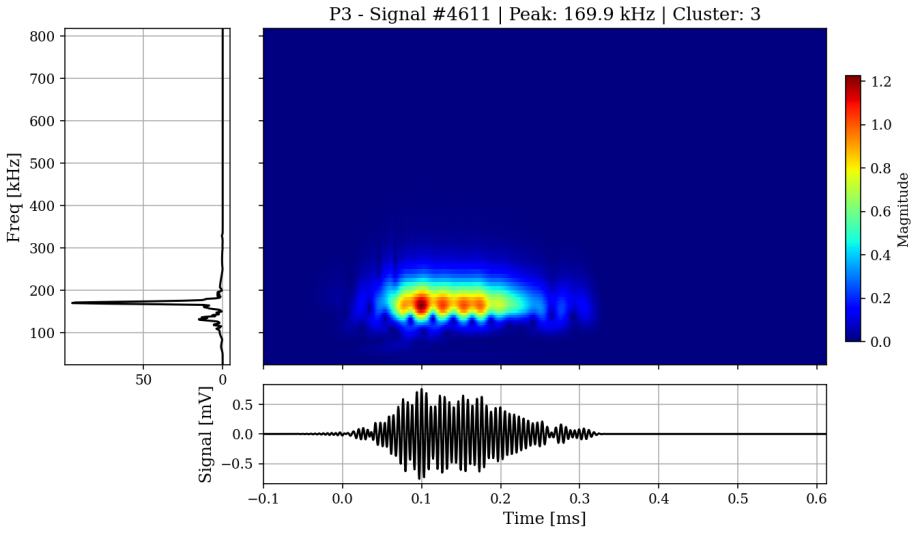

Figure 104: Morlet Wavelet Transform of an Acoustic Signal - P3 - Cluster 3

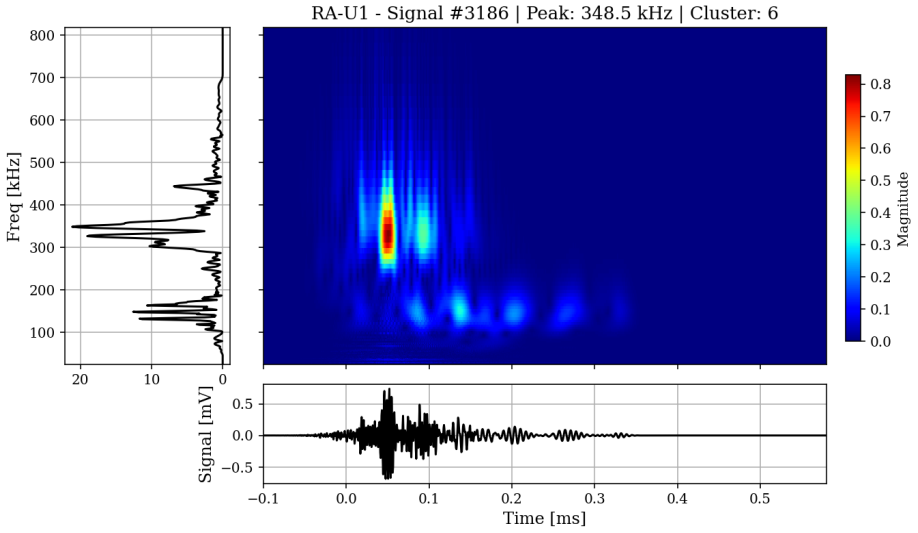

Figure 105: Morlet Wavelet Transform of an Acoustic Signal - RA-U1 - Cluster 6

9.5.1 Preemptive Detection of Kissing Bonds

As previously described in the section 5, a high frequency scattering was noted in research performed by Teixeira et al. [68]. Here, specimens were contaminated with release agent to simulate artificial kissing bonds. Wavelet transforms were performed on measured signals from testing both pristine and contaminated specimens. A scattering effect is observed in the contaminated specimen, possibly

due to wave interactions with the contamination. The scattering is most noticeable in the 300 to 500 [kHz] range.

In order to recreate this effect, wavelet transforms were performed at multiple instances over all specimens types. Indeed, a scattering effect was observed for all specimens containing artificial defects in the majority of signals. One such example can be found in Figure 106.

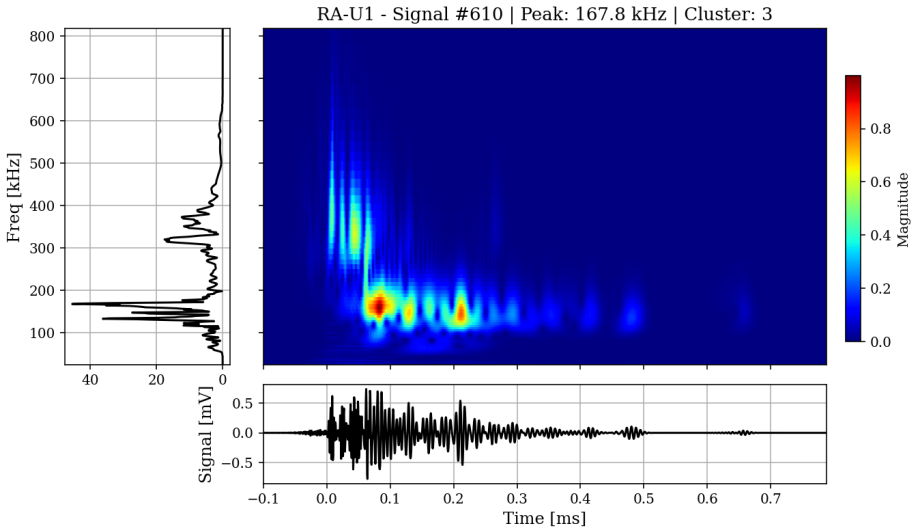

Figure 106: Scattering observed in signal frequency spectrum prior to reaching contaminated area. - RA-U1

This signal was captured while the crack was propagating cohesively prior to reaching the defective area. This aligns with results found by Teixeira et al. By observing this frequency scatter prior to reaching a kissing bond defect, observing such scatter could be used as an early detection method for bondline contamination.However, scattering was also observed in pristine specimens, containing no intentional defects. A signal captured from a pristine specimen can be found in Figure 107.

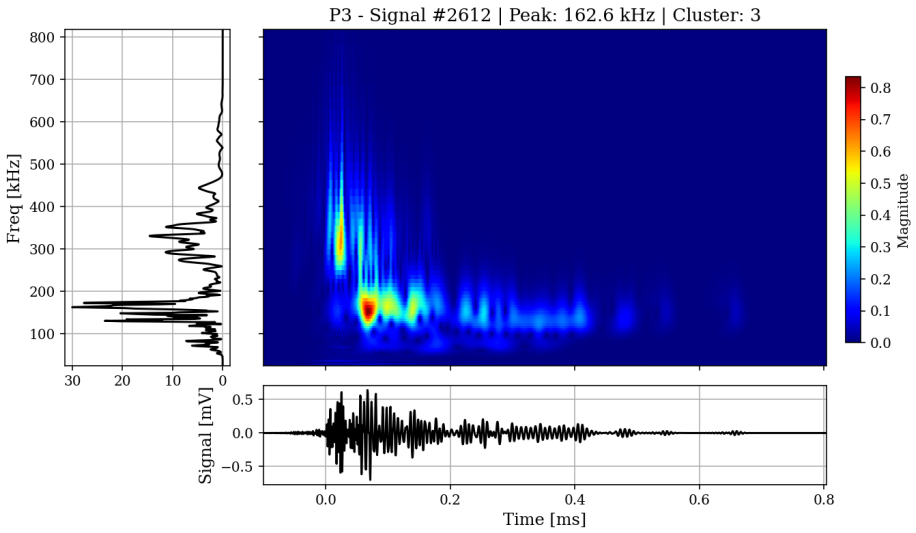

Figure 107: Scattering observed in signal frequency spectrum in pristine specimen - P3

It can be noted that both signals look distinctly similar, despite being taken from specimens containing either no defects or highly impaction contamination. In actuality, the majority of all signals across the different specimen types are shown to have a broad frequency spectrum. The more distinct wavelet transforms of Cluster 2, Cluster 3 and Cluster 6 signals shown in Figure 103, Figure 104 and Figure 105 respectively, which showed single peak frequencies, are in the minority when considering all transformed signals. A number of Cluster 3 signals have been transformed to indicate the average transformed signal profile for each specimen type, which can be found in Figure 108.

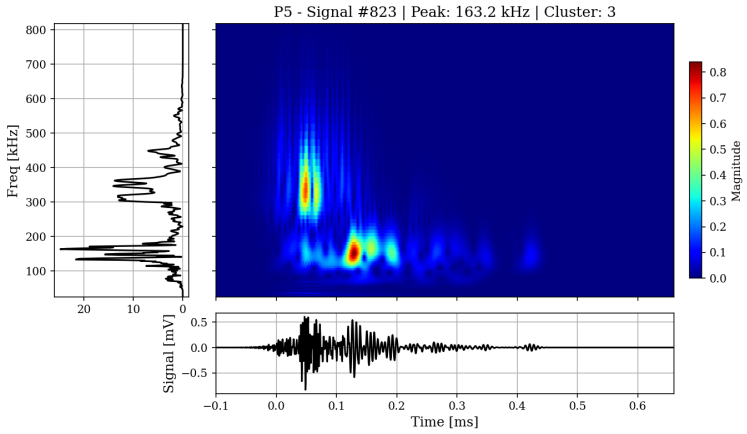

(a) Transformed Signal P5 – with frequency scatter

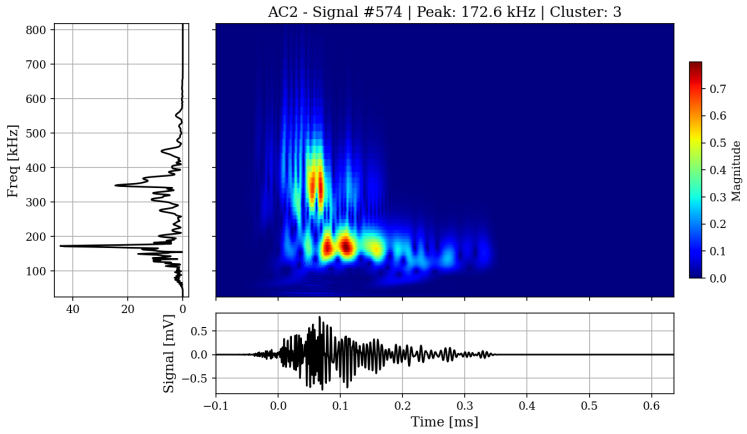

(b) Transformed Signal AC2 – with frequency scatter

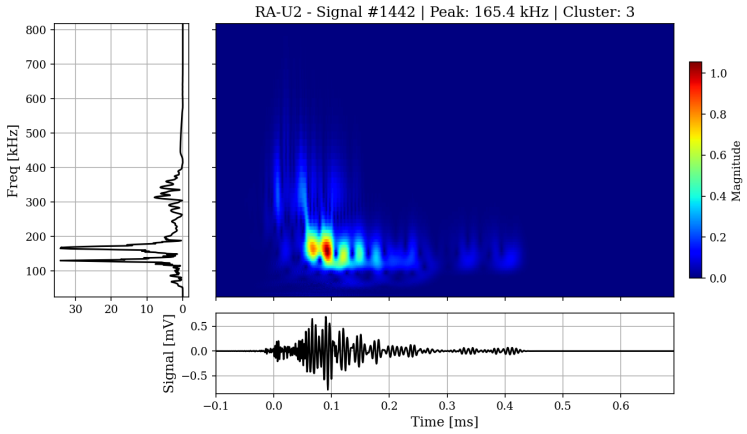

(c) Transformed Signal RA-U2 – no frequency scatter

Figure 108: Examples of transformed signals across three specimens, showing presence or absence of high-frequency scattering.

It can be stated that these signals, in their transformed state, show many different frequency components in the same signal. In the case of Figure 108a, Cluster 2, Cluster 3, Cluster 5 and Cluster 6 all seem to be present. This specimen shows a wide frequency range, despite not being contaminated with added defects. AC2 shows a similar signature in Figure 108b, where Cluster 3 appears more dominant.

RA-U1, shown in Figure 108c, was included to outline the difficulties with assigning specific clusters to signals with a broad frequency spectrum. Here, Cluster 3 only shows a slightly more dominant contribution, with Cluster 2 showing a near identical peak at 130 [kHz]. However, because manual clustering only considers the peak frequency, this signal was labeled as a Cluster 3 signal, despite Cluster 2 showing near equal representation. When using manual clustering, this information is not represented when characterizing signal types.

This new insight shows the limitations in performing clustering analysis based on peak frequency, amplitude and energy. As can be seen in these wave transforms, signals can have a multitude of different components, all significant and dominating at different times in a signals frequency spectrum.

9.5.2 Spectrum Comparison including All Signals

Instead of looking at peak frequency of signals to classify certain failure mode, the frequency spectrum of each specimen type is averaged across all specimens. This is done to create a signature frequency spectrum per specimen defect type. This method considers all contributions to different frequency ranges in all signals measured, whereas clustering only revealed information on the signals based on their peak frequency measured.

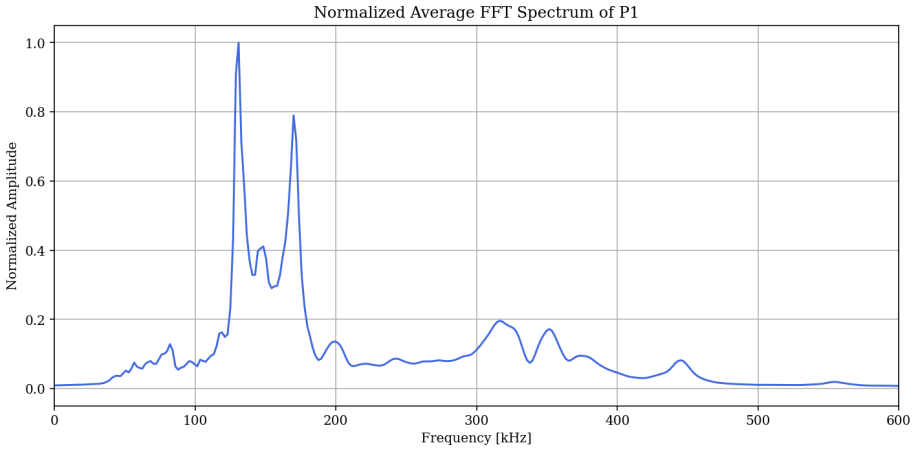

Figure 109: Signature Frequency Spectrum of P1

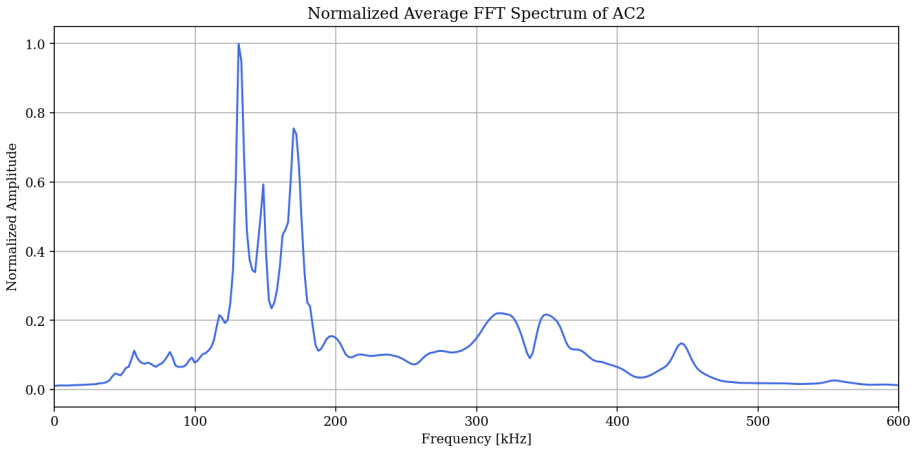

Figure 110: Signature Frequency Spectrum of AC2

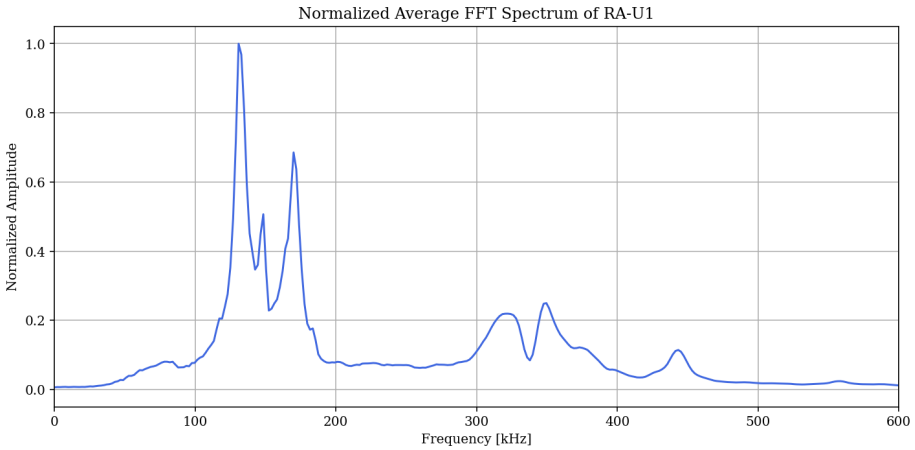

Figure 111: Signature Frequency Spectrum of RA-U1

In these plots, certain patterns can be noted that reaffirm findings of the manual clustering approach. First, RA-U1 again shows a higher Cluster 2 and Cluster 6 activity, as can be seen by its peaks at 130 [kHz] and 350 [kHz] in Figure 111. For this specimen, minimal Cluster 1 activity can also be noticed. P1 shows higher Cluster 3 activity, whereas AC2 shows more activity in Cluster 7. This can be seen in Figure 109 and Figure 110, respectively. Both these observations align with findings found in the previous manual clustering approach.

While certain features can be identified using this method, the main contribution of this on the analysis of the measured signals is to signify the similarities that can be found across the different specimen types. More so, it shows the challenges of identifying signal characteristics based on frequency and amplitude components, when signals are highly complex in their frequency spectrum.

9.6 Discussion

The acoustic emission (AE) analysis results presented in this chapter have further demonstrated the potential of identifying failure modes in bonded composite joints using AE monitoring techniques. Failure modes such as cohesive failure, adhesion failure, delamination and bondline inclusions could be identified through a manual clustering approach. Using Morlet wavelet transforms, the acoustic signals could be characterized based on their dominant frequency components over time. Both methods show that classification of failure modes and identification of specimen defect type is possible, to an extend.

Initial analysis of signals revealed insights on fracture behavior of the specimens, simply by observing trends in acoustic hits and acoustic energy measured. Patterns related to cohesive failure, delamination and adhesion failure were identified by observing hits over time, as well as cumulative hits and cumulative energy measured. These initial AE metrics act as initial indicators for failure modes originating and propagation, which diverge from the norm set by baseline specimens. They can therefore be used as an early-stage detection of defected areas or in-situ monitoring of crack propagation.

Challenges in the identification of signal characteristics for signals with a broad frequency spectrum remain, as the majority of signals show multiple peak frequency components of different clusters occurring within the same signal frequency over time spectrum.

Specimen characteristics were able to be identified based on acoustic signals measured. For example, pristine specimen P1 showed increased activity in the cluster associated with delaminations (Cluster 2). Other pristine specimens (P3, P4 and P5) which failed primarily cohesively showed an increase activity in the cluster assigned to cohesive failure (Cluster 3). The added analysis of specimens M1 and M2, which almost entirely delaminated during mechanical testing reinforced the classification of these clusters, showing the most contribution to Cluster 2 (delamination) and the least contribution to Cluster 3 (cohesive failure) out of all specimens tested.

However, unexpected inconsistent results also appeared. For example, P2 shows a higher contribution to delamination compared to P1, while the fracture surfaces of both specimens clearly show P1 experiencing more delamination as a failure mode. Additionally, pristine specimen P4 shows relatively strong indications of inclusive failures (Cluster 7), which mainly dominates in specimens with inclusions, AC2 and AC3. These observations suggest that while AE characteristics are shown to reveal reliable identification of certain failure modes, the variability in the results must be further studies to achieve a consistent failure mode detection method.

The difficulty in detecting and characterizing Cluster 1 might originate from the sensor's inherently low sensitivity to signals below 100 [kHz]. This insensitivity likely preventing low-energy signals belonging to the cluster from being identified. This inability to detect lower-energy signals can be crucial, especially when attempting to identify minor defects such as interface disbonds or kissing bonds. Therefore, additional testing using more low-frequency sensitive sensors must be conducted in future research to further identify the origin of Cluster 1 signals and the quantify of signals that in this presented research were non-detectable.

While manual cluster provided characteristic clusters, interpretation of the results are more difficult to define. Cluster 2, designated as delamination, can be identified with high confidence. However,

this cluster is present in all specimens testing to a large extend. Even in specimens that showed no visible delamination on the fracture surface, which can be observed for specimens P3, P4 and P5. It is possible that acoustic emissions from cohesive failure / adhesive fracture are similar to delamination signals, or it could be that delaminations present amplify this cluster, the signals of which originating from a different failure mode present in all specimens. Similarly, Cluster 7 is identified as being resultant from inclusion type defects. Their presence in all specimens however, suggest that the origin of these signals are not related to the inclusion itself, but their signature is instead amplified by the presence of inclusions. Cluster 6, identified with fiber breakage in either the composite or adhesive carrier, has a less certain origin. This is due to limited distinguishing features across specimens. Microscopy images of the fracture surface post-testing might reveal more insights in the cause of this frequency cluster.

As for unsupervised clustering, the inconsistencies in identified clusters made comparison between specimens inconsistent, as the amount of clusters identified was variable even between specimens of the same type. This approach could be further refined, by introducing other wave characteristics besides energy and frequency. For example, wave duration, rise time and the number of counts per hit can be added in the mapping of these specimens, potentially leading to more consistent identification of clusters that is less reliant on manual observations on peak frequency occurrence.

Wavelet transforms provided more detailed insights in the frequency signature of each signal and how it varies over time. The identification of multiple frequency components revealed the importance of using this type of analysis. This effect would not be apparent when only considering the peak frequency, as is the case for manual clustering. It became apparent that the majority of signals had multiple frequency components, where the difference between components was at times minimal.

Lastly, by performing wavelet transforms, the scattering of high-frequency components in contaminated specimens could be observed, as was revealed in research done by Teixeira et al. However, scattering was observed in all specimens, including specimens containing a pristine bondline. Additionally, most signals captured showed multiple frequency components in their signatures, including a broad high-frequency contrition.

It can also be observed that the high-frequency scattering observer in Figure 108, are similar in signature to the identified Cluster 6, which can be found in Figure 105. It therefore can be said that this scattering is likely the result of an unknown failure mode associated with Cluster 6, likely related to fiber failure. However, it could also be the case that this frequency scatter is indeed caused by defects in the adhesive interface, adhesive itself or the adherend material. Unintended defects in either of these areas could unintentionally be the origin of these higher-frequency components. It could be the case that these signals were not present in results presented by Teixeira et al., due to a higher quality in specimen production or a more consistent introduction of indented defects. The inconsistent nature of the carbon material used in the presented research further supports this theory, as a result of manufacturing challenges encountered previously outlined in subsection 7.3.

In order to further understand these effects, additional testing must be conducted. Specimens of higher quality might result in a more controlled failure and failure mode, making for better identification of these failure modes using acoustic data. More accurate crack length measurements can be taken using a traveling microscope or by using Digital Image Correlation. This would aid in identifying when certain signals occur at the crack tip location. Additionally, using a specimen that fully fails through delamination can be included as a reference without an adhesive layer present

to further identify which signal clusters can be attributed to failure of the adhesive or adhesive interface, as they should be absent or less represented in those results.

9.7 Conclusion on Acoustics

This chapter has explored the potential use of Acoustic Emission (AE) analysis to characterize failure modes in adhesively bonded joints and to study the feasibility of using this monitoring technique to preemptively detect bond defects, specifically kissing bonds. By extracting AE features such as hits and energy, clustering analysis of signals and time-frequency analysis using Morlet wavelet transformations, partial classification of failure mode has successfully been achieved. The results provide insights in the relation between Acoustic signal signatures and artificial bond defects.

Using fundamental acoustic parameters such as hits and cumulative energy, the dominant failure mode per region could be identified. Cohesive failure revealed steady increases in both metrics. Delamination resulted in more acoustic hits and higher cumulative energy observed. Adhesion failure or rapid delamination could be recognized by stagnation in cumulative hits and energy, as a results of large crack propagation occurring. While basic compared to other metrics considering frequency components, these principle metrics remain a valid method for monitoring general damage progression and identification of failure modes.

The identification of main failure modes such as cohesive failure, adhesion failure and delamination could be identified with relatively high confidence. This was also the case for inclusion type defects, but the origin of these characteristic signals remains speculative. The differences in cluster activity associated with delamination (Cluster 2: 130 [kHz]), cohesive failure (Cluster 3: 170 [kHz]) and adhesion failure (Cluster 5: 320 [kHz]) show the potential for AE monitoring to distinguish between bondline defects and present failure modes. However, overlap between the different clusters and the presence of multiple significant peak frequencies suggest room for improvement in classifying signals into these distinct clusters. Additionally, inconsistencies in the results outline the limitations when using a clustering approach in this manner.

Morlet wavelet transforms revealed the time-dependence of peak frequencies occurring in the measured signal signatures. These insights could not be identified using other AE metrics, such as hit or energy counting and clustering based on peak frequency and energy. This method revealed the broad frequency range present in the majority of signals, and the complications that arise when it comes to signal characterization.

Additionally, the findings regarding frequency scatter attributed to bondline defects described by Teixeira et al. [68] could not be replicated in this study. High-frequency scatter was observed in all specimens, including pristine specimens with no artificial bond defect. The high-frequency component observed was present in the majority of signals across all specimens and appears to be related to fiber failure instead of contamination. An alternative theory would be that inconsistencies in the specimen quality resulted in high-frequency scattering occurring in all specimens, including pristine ones. This would also explain how such signals are present in all specimens, regardless of potential included defects or failure modes. Still, the observation of this effect refutes the assumption that scattering is caused by contamination of the bond interface, while also highlighting the need for further research using more controlled application of defects and a more consistent production quality of the specimens.

AE monitoring shows significant promise when it comes to evaluation of bonded joints. But, additional research is needed in order to further develop this technology as a method of structural health monitoring of adhesive bonds. Additional methods for analyzing bond failure during and after mechanical testing can be implemented, such as fracture surface microscopy for identifying failure modes, or more accurate crack propagation measurements. As for the analysis of acoustic data, machine learning techniques can help improve the accurate clustering of acoustic signals. This is especially needed considering the multitude of peak frequencies present in acoustic signals and their complex nature. Additional specimens, including specimens of higher quality should be made to further study the origin of frequency scatter for defective specimens to accurately decern if this effect is truly related to interfacial defects in the bondline. Lastly, damage detection of bonds undergoing failure should be studied outside of static DCB tests. Fatigue testing and lap shear tests are to be conducted to obtain a more complete understanding of the failure modes in adhesive bonds and their characteristic AE signatures. More realistic structures should also be tested to determine if AE monitoring is applicable when not measuring a consistent and simple structure such as a DCB specimen. This must be done to determine if failure modes can still be detected and characterized when signals are propagating a complex, three-dimensional structure.

Further refinement in the analysis of AE signals captured while monitoring adhesive bondlines can result in AE monitoring becoming a method of measuring bond integrity for aerospace structures, which could further lead to a more efficient and replicable method of bondline certification in industry.

Conclusion

This thesis was conducted to study the potential of Acoustic Emission (AE) monitoring as a method of detecting kissing bonds and other bond defect types in adhesively bonded composite structures. Bonded joints allow for more structurally efficient aircraft design and are becoming an increasingly preferred alternative over traditional, mechanical fasteners. However, the inability to reliably inspect bonded joints remains a technological challenge, particularly when it comes to detecting zero-volume bonds, also known as kissing bonds.

Mechanical testing of specimens was conducted, using Double Cantilever Beam (DCB) specimens. During mechanical testing, acoustic emission (AE) monitoring was used to study acoustic signals emitted by the specimen under Mode I loading. Numerous specimen types were manufactured, including pristine, inclusion type and kissing bond type defects implemented by contaminating the adherend surface with release agent. Mechanical test results showed that artificial defects significantly decreased the effective fracture toughness G_{eff} of the bonded joints and induced a multitude of failure modes. These include cohesive failure, adhesion failure and delamination of the adherend material. Most notably, specimens contaminated with release agent showed premature adhesion failure, which simulates a kissing bond failure. The kissing bonds implemented, could not be detected using conventional C-Scan measurements. This validates the effectiveness of using release agent as contamination to induce kissing bonds in bonded structures.

AE monitoring revealed consistent signal characteristics across specimens experiencing cohesive failure. Additional failure modes, such as delamination and adhesive failure, could also be identified using different acoustic metrics. A direct relation between acoustic cumulative energy and G_{eff} could not be confirmed, but were consistent for specimens failing fully cohesively. Trends in cumulative hits and energy could however be related to adhesion failure and delamination, when compared to a baseline behavior set by pristine specimens. This includes the detection of kissing bond defects previously undetectable with conventional C-Scan methods. Therefore, the following hypothesis can be accepted:

Hypothesis 1: Kissing bonds and other defect types can be detected by analysis of the acoustic signals monitored during destructive testing of the bond.

Other acoustic metrics such as peak frequency and amplitude were used to cluster signals in respective frequency bands to distinguish between different failure modes. Cluster analysis of signals revealed specific frequency bands, which were each linked to certain damage mechanisms or failure modes. Manual clustering, combined with a comparative heatmap, allowed for the association of signal frequencies and present failure modes. Frequency clusters associated with cohesive failure, delamination and inclusions could be identified, while other clusters were associated with other or mixed failure modes and potential complex wave interactions. Specimens experiencing delaminations showed increase activity at 130 [kHz], while pristine specimens, predominantly failing cohesively, showed the most activity at 170 [kHz].

Furthermore, wavelet transform analysis revealed evidence of frequency scatter for contaminated specimens, supporting previous finding in similar research. Consistent results could not be replicated, but the potential for preemptive detection of bond defects remains. Wavelet transforms were used to highlight the complex nature of the acoustic signals emitted and the challenges that arise

when performing characterization on specimens containing a multitude of high energy frequency components. Given these findings, hypothesis 2 can be partially confirmed:

Hypothesis 2: High-frequency scattering of acoustic signals vary with with defect size or type and can be used for preemptive detection of bond defects.

Wavelet transforms indeed showed frequency scattering for contaminated specimens. However, scattering was inconsistent and present for all defect types, including pristine specimens. Scattering could therefore also not be correlated to defect size. The potential for preemptive detection however, remains. As a result, hypothesis 3 can be partially refuted:

Hypothesis 3: No correlation is to be found between signal scattering and defect type or size, suggesting that scattering is unrelated to interfacial defects and originate from a different acoustic phenomenon.

While results on frequency scatter were not conclusive, previous assessments using clustering and hit characterization do not support that frequency scatter is completely unrelated to defect type.

In conclusion, AE monitoring of bonded specimens is demonstrated as a promising method for detecting and characterizing bond defects in bonded specimens. Kissing bonds are seemingly detectable when combined with advanced signal processing methods however, future work will be needed to improve the signal classification before a definitive conclusion can be made.

References

[1] K. J. Abbey. "Advances in epoxy adhesives". In: *Advances in Structural Adhesive Bonding* (Jan. 2010), pp. 20–34. DOI: 10.1533/9781845698058.1.20.

[2] M. M. Abdel Wahab. "Fatigue in Adhesively Bonded Joints: A Review". In: *ISRN Materials Science* 2012 (Nov. 2012), pp. 1–25. DOI: 10.5402/2012/746308.

[3] Airbus. *End of life: Reusing, recycling, rethinking.* Nov. 2022.

[4] Alconox Inc. *What is the Water Break Test?* 2013.

[5] ASTM-D5528-13. *Test Method for Mode I Interlaminar Fracture Toughness of Unidirectional Fiber-Reinforced Polymer Matrix Composites.* West Conshohocken, PA, Oct. 2013. DOI: 10.1520/D5528-13. URL: http://www.astm.org/cgi-bin/resolver.cgi?D5528-13.

[6] A. A.. Baker, Stuart. Dutton, and Donald. Kelly. *Composite materials for aircraft structures.* American Institute of Aeronautics and Astronautics, 2004. ISBN: 1563475405.

[7] Mariana D. Banea. "Influence of adherend properties on the strength of adhesively bonded joints". In: *MRS Bulletin* 44.8 (Aug. 2019), pp. 625–629. ISSN: 08837694. DOI: 10.1557/mrs.2019.180.

[8] Werner J Blank, Za He, and Marie Picci-King Industries Inc. *Catalysis of the Epoxy-Carboxyl Reaction.* Tech. rep. 926. 2002.

[9] Kay Y Blohowiak, Matthew A Dilligan, William B Grace, Chul Y Park, Marc J Piehl, Peter Van Voast, Eileen O Kutscha, and Harlan R Ashton. *Qualified Bonded Systems Approach to Certified Bonded Structure.* Tech. rep. NATO Science and Technology Organisation, 2017.

[10] Broughton W.R. *Testing the Mechanical, Thermal and Chemical Properties of Adhesives for Marine Environments.* Tech. rep. Adhesives in Marine Engineering, 2012, pp. 99–154.

[11] Alasdair R Crawford, Mohamad G Droubi, and Nadimul H Faisal. *MODAL ACOUSTIC EMISSION ANALYSIS OF MODE-I AND MODE-II FRACTURE OF ADHESIVELY-BONDED JOINTS.* Tech. rep. 2018. URL: http://www.ndt.net/?id=23572.

[12] Lucas F M Da Silva, Andreas Öchsner, and Robert D Adams. *Handbook of Adhesion Technology.* Tech. rep. 2018.

[13] Davis. *Best Practice in Adhesive-Bonded Structures and Repairs.* Tech. rep. 2007.

[14] M J Davis and D A Bond. *CERTIFICATION OF ADHESIVE BONDS FOR CONSTRUCTION AND REPAIR.* Tech. rep. 2000.

[15] M J Davis and D A Bond. *THE IMPORTANCE OF FAILURE MODE IDENTIFICATION IN ADHESIVE BONDED AIRCRAFT STRUCTURES AND REPAIRS.* Tech. rep. 1999.

[16] Maxwell James Davis, M Eng, Andrew Mcgregor, and B Eng. *Assessing Adhesive Bond Failures: Mixed-Mode Bond Failures Explained.* Tech. rep. 2010. URL: www.adhesionassociates.com.

[17] Juliette Dubon, Gonzalo Seisdedos, Dillon Watring, Mauricio Pajon, Sakhrat Khizroev, Dwayne McDaniel, and Benjamin Boesl. "Multifunctional MEN-Doped Adhesives: Strengthening, Bond Quality Evaluation, and Variations in Magnetic Signal with Environmental Exposure". In: *Applied Sciences (Switzerland)* 12.16 (Aug. 2022). ISSN: 20763417. DOI: 10.3390/app12168238.

[18] Federal Aviation Administration. "14 CFR 23.573 - Damage tolerance and fatigue evaluation of structure." In: *U.S. Department of Transportation* (2010). URL: https://www/ecfr.gov.

[19] Federal Aviation Administration. "Bonded joints and structures- Technical issues and certification considerations (PS-ACE100-2005-10038)". In: *U.S. Department of Transportation* (2005).

[20] C. Fualdes and K. Davis. *Transport Airplane Metallic and Composite Structures Working Group Recommendation Report-Structural Bonding Transport Airplane Metallic and Composite Structures Working Group-Recommendation Report to FAA Structural Bonding*. Tech. rep. FAA, 2021.

[21] Joseph D Garrett. *EXPERIMENTATION OF MODE I & MODE II FRACTURE OF UNIDIRECTIONAL COMPOSITES AND FINITE ELEMENT ANALYSIS OF MODE I FRACTURE USING COHESIVE CONTACT*. Tech. rep. 2016.

[22] Christian U Grosse, Masayasu Ohtsu, Dimitrios G Aggelis, and Tomoki Shiotani. *Springer Tracts in Civil Engineering Acoustic Emission Testing Basics for Research-Applications in Engineering Second Edition*. Tech. rep. 2022. URL: http://www.springer.com/series/15088.

[23] Nsaif jasim Hadi, Ahmed Atiyah Itwayya, Ameer L. Saleh, and Hayder Tarar. "Monitoring corrosion in oil pipelines using non-destructive test". In: *Periodicals of Engineering and Natural Sciences* 7.4 (2019), pp. 1950–1964. ISSN: 23034521. DOI: 10.21533/pen.v7i4.859.

[24] A Higgins. *Adhesive bonding of aircraft structures*. Tech. rep. 1998, pp. 367–376.

[25] N D Hull and T W Clyne. *Cambridge Solid State Science Series*. Tech. rep.

[26] Ibrahim A Imam. *Finite Element Analysis of Delamination in Drilling Composite Laminates*. Tech. rep. International Journal of Engineering Research & Technology (IJERT), 2019. URL: www.ijert.org.

[27] International Energy Agency. *Net Zero by 2050 - A Roadmap for the Global Energy Sector*. Tech. rep. 2021. URL: www.iea.org/t&c/.

[28] Gyoung Gug Jang, Jiheon Jun, Sinchul Yeom, Mina Yoon, Yi Feng Su, John Wade, Michael S. Stephens, and Jong K. Keum. "Atmospheric Pressure Plasma Treatment of Magnesium Alloy for Enhanced Coating Adhesion and Corrosion Resistance". In: *Coatings* 13.5 (May 2023). ISSN: 20796412. DOI: 10.3390/coatings13050897.

[29] C. W. Jennings. "Surface roughness and bond strength of adhesives1". In: *The Journal of Adhesion* 4.1 (1972), pp. 25–38. ISSN: 15455823. DOI: 10.1080/00218467208072208.

[30] Christos Kassapoglou. *DESIGN AND ANALYSIS OF COMPOSITE STRUCTURES: WITH APPLICATIONS TO AEROSPACE STRUCTURES*. Tech. rep. Wiley, 2010.

[31] Shivi Kesarwani. *Polymer Composites in Aviation Sector A Brief Review Article*. Tech. rep. International Journal of Engineering Research & Technology (IJERT), June 2017. URL: www.ijert.org.

[32] Safdar Ali Khan, Seyed Saeid Rahimian Koloor, Wong King Jye, Geralt Siebert, and Mohd Nasir Tamin. "A Fatigue Model to Predict Interlaminar Damage of FRP Composite Laminates Subjected to Mode I Load". In: *Polymers* 15.3 (Feb. 2023). ISSN: 20734360. DOI: 10.3390/polym15030527.

[33] A. J. Kinloch. *Adhesion and Adhesives*. Dordrecht: Springer Netherlands, 1987. ISBN: 978-90-481-4003-9. DOI: 10.1007/978-94-015-7764-9. URL: http://link.springer.com/10.1007/978-94-015-7764-9.

[34] F Kishinouye. "Frequency-distribution of the Itô Earthquake Swarm of 1930". In: *Bulletin of the Earthquake Research Instituem Tokyo Imperial University* 15(3) (Mar. 1937), pp. 785–827.

[35] Martin Kluke. "The joining of composite materials: the best of both worlds". In: *Reinforced Plastics* 62.2 (Mar. 2018), pp. 79–81. ISSN: 00343617. DOI: 10.1016/j.repl.2017.06.082.

[36] Tribikram Kundu. *Acoustic source localization*. Jan. 2014. DOI: 10.1016/j.ultras.2013.06.009.

[37] Tribikram Kundu, Samik Das, Steven A. Martin, and Kumar V. Jata. "Locating point of impact in anisotropic fiber reinforced composite plates". In: *Ultrasonics* 48.3 (July 2008), pp. 193–201. ISSN: 0041624X. DOI: 10.1016/j.ultras.2007.12.001.

[38] J. Kupski, S. Teixeira de Freitas, D. Zarouchas, P. P. Camanho, and R. Benedictus. "Composite layup effect on the failure mechanism of single lap bonded joints". In: *Composite Structures* 217 (June 2019), pp. 14–26. ISSN: 02638223. DOI: 10.1016/j.compstruct.2019.02.093.

[39] D. S. Lee, D. W. Fahey, A. Skowron, M. R. Allen, U. Burkhardt, Q. Chen, S. J. Doherty, S. Freeman, P. M. Forster, J. Fuglestvedt, A. Gettelman, R. R. De León, L. L. Lim, M. T. Lund, R. J. Millar, B. Owen, J. E. Penner, G. Pitari, M. J. Prather, R. Sausen, and L. J. Wilcox. "The contribution of global aviation to anthropogenic climate forcing for 2000 to 2018". In: *Atmospheric Environment* 244 (Jan. 2021). ISSN: 18732844. DOI: 10.1016/j.atmosenv.2020.117834.

[40] R A A Lima, A Oswal, N Roux, A Bernasconi, M Carboni, N Carrere, and S Teixeira De Freitas. "ENHANCEMENT OF MODE I FRACTURE TOUGHNESS OF ADHESIVELY BONDED SECONDARY JOINTS USING LAYUP PATTERNING OF CFRP". In: (2022). DOI: 10.5075/epfl-298799{_}978-2-9701614-0-0.

[41] R. A.A. Lima, R. Tao, A. Bernasconi, M. Carboni, and S. Teixeira de Freitas. "Acoustic emission approach for identifying fracture mechanisms in composite bonded Joints: A study on varying Substrate's stacking sequence". In: *Theoretical and Applied Fracture Mechanics* 132 (Aug. 2024). ISSN: 01678442. DOI: 10.1016/j.tafmec.2024.104490.

[42] Junyi Liu, Xiaohu Huang, Yi Ren, Lai Mun Wong, Hongfei Liu, and Shijie Wang. "Galvanic corrosion protection of Al-alloy in contact with carbon fibre reinforced polymer through plasma electrolytic oxidation treatment". In: *Scientific Reports* 12.1 (Dec. 2022). ISSN: 20452322. DOI: 10.1038/s41598-022-08727-7.

[43] Chuanlong Ma, Anton Nikiforov, Dirk Hegemann, Nathalie De Geyter, Rino Morent, and Kostya Ostrikov. "Plasma-controlled surface wettability: recent advances and future applications". In: *International Materials Reviews* 68.1 (2023), pp. 82–119. ISSN: 17432804. DOI: 10.1080/09506608.2022.2047420.

[44] J. Manterola, M. Aguirre, J. Zurbitu, J. Renart, A. Turon, and I. Urresti. "Using acoustic emissions (AE) to monitor mode I crack growth in bonded joints". In: *Engineering Fracture Mechanics* 224 (Feb. 2020). ISSN: 00137944. DOI: 10.1016/j.engfracmech.2019.106778.

[45] Gao Mantong and Xu Changgan. *CONTACT CORROSION BETWEEN CARBON FIBER REINFORCED COMPOSITE MATERIALS AND HIGH-STRENGTH METALS 19951023 096*. Tech. rep. National Air Intelligence Center, 1995.

[46] Ana C. Marques, Alexandra Mocanu, Nataša Z. Tomić, Sebastian Balos, Elisabeth Stammen, Asa Lundevall, Shoshan T. Abrahami, Roman Günther, John M.M. de Kok, and Sofia Teixeira de Freitas. *Review on adhesives and surface treatments for structural applications: Recent developments on sustainability and implementation for metal and composite substrates*. Dec. 2020. DOI: 10.3390/ma13245590.

[47] martin cames martin, jakob graichen jakob, anne siemons anne, and vanessa cook vanessa. *DIRECTORATE GENERAL FOR INTERNAL POLICIES POLICY DEPARTMENT A: ECONOMIC AND SCIENTIFIC POLICY Emission Reduction Targets for International Aviation and Shipping STUDY*. Tech. rep.

[48] Carosena Meola, Simone Boccardi, and Giovanni M. Carlomagno. "Composite material overview and its testing for aerospace components". In: *Sustainable Composites for Aerospace Applications*. Elsevier, Jan. 2018, pp. 69–108. ISBN: 9780081021316. DOI: 10.1016/B978-0-08-102131-6.00005-0.

[49] Miller R. K., P. O. Moore, and E. v.K. Hill. *Nondestructive Testing Handbook: Volume 6 - Acoustic Emission (3rd ed.)*. Tech. rep. American Society for Nondestructive Testing, 2005.

[50] B.-G Min, Z H Stachurski, J H Hodgkin, and G R Heath. *Quantitative analysis of the cure reaction of DGEBA/DDS epoxy resins without and with thermoplastic polysulfone modifier using near infra-red spectroscopy*. Tech. rep. 1993.

[51] Miracle. Daniel B. and Steven L. Donaldson. *ASM INTERNATIONAL ® Publication Information and Contributors*. Tech. rep. ASM International Handbook Committee, 2001, pp. 271–286.

[52] Govindu N and Jayanand Kumar T. "Design and Optimization of Screwed Fasteners to Reduce Stress Concentration Factor". In: *Journal of Applied Mechanical Engineering* 04.04 (2015). DOI: 10.4172/2168-9873.1000171.

[53] Nondestructive Testing (NDT) Resource Center. *Introduction to Acoustic Emission (AE)*. URL: https://www.nde-ed.org/NDETechniques/AcousticEmission/AE_History.xhtml.

[54] Stanley Udochukwu Ofoegbu, Mário G.S. Ferreira, and Mikhail L. Zheludkevich. *Galvanically stimulated degradation of carbon-fiber reinforced polymer composites: A critical review*. Feb. 2019. DOI: 10.3390/ma12040651.

[55] Sadik Omairey, Nithin Jayasree, and Mihalis Kazilas. *Defects and uncertainties of adhesively bonded composite joints*. Sept. 2021. DOI: 10.1007/s42452-021-04753-8.

[56] Siva Palani, Corrdesa Llc, Alan Rose, and Keith Legg. *MODELING GALVANIC CORROSION BEHAVIOR OF CARBON FIBER COMPOSITE/AL 7050 JOINTS UNDER EXTENDED EXPOSURES*. Tech. rep. 2017.

[57] Edward M. Petrie. "Adhesive Bonding of Aluminum Alloys". In: *Metal Finishing* 105.9 (Sept. 2007), pp. 49–56. ISSN: 0026-0576. DOI: 10.1016/S0026-0576(07)80220-0.

[58] Edward M. Petrie. "How moisture affects adhesives, sealants, and coatings". In: *Metal Finishing* 109.7 (2011). ISSN: 00260576. DOI: 10.1016/S0026-0576(13)70070-9.

[59] Marvin Pollum, Joseph Kriley, Masa Nakajima, Kar Tean Tan, Jeffrey Stalker, Richard Fleischauer, and Brian Rearick. *STRUCTURAL ADHESIVE WITH COMBINED HIGH STRENGTH AND DUCTILITY FOR MULTIMATERIAL JOINING AND GALVANIC ISOLATION*. Tech. rep. 2018.

[60] *Practice for Classifying Failure Modes in Fiber-Reinforced-Plastic (FRP) Joints*. West Conshohocken, PA, June 2019. DOI: 10.1520/D5573-99R19. URL: http://www.astm.org/cgi-bin/resolver.cgi?D5573-99R19.

[61] Yao Qiao, Yongsoon Shin, Madhusudhan R. Pallaka, Ethan K. Nickerson, Daniel R. Merkel, Robert J. Seffens, Angel Ortiz, Jose L. Ramos, and Kevin L. Simmons. "Plasma surface modification coupled with thermal and step-over distance effects on significant fracture improvement of adhesively-bonded metal-CFRTP dissimilar materials". In: *Composites Science and Technology* 232 (Feb. 2023), p. 109833. ISSN: 0266-3538. DOI: 10.1016/J.COMPSCITECH.2022.109833.

[62] Antonia Rahn, Kai Wicke, and Gerko Wende. "Using Discrete-Event Simulation for a Holistic Aircraft Life Cycle Assessment". In: *Sustainability (Switzerland)* 14.17 (Sept. 2022). ISSN: 20711050. DOI: 10.3390/su141710598.

[63] Salvatore Salamone, Ivan Bartoli, Patrizia Di Leo, Francesco Lanza Di Scalea, Augusto Ajovalasit, Leonardo D'Acquisto, Jennifer Rhymer, and Hyonny Kim. "High-velocity impact location on aircraft panels using macro-fiber composite piezoelectric rosettes". In: *Journal of Intelligent Material Systems and Structures* 21.9 (June 2010), pp. 887–896. ISSN: 1045389X. DOI: 10.1177/1045389X10368450.

[64] M G R Sause and E Jasiūnienė. *Structural Health Monitoring Damage Detection Systems for Aerospace*. Tech. rep. Springer, 2022. URL: http://www.springer.com/series/8613.

[65] Jochen Schanz, Dieter Meinhard, Isabell Dostal, Harald Riegel, Anjali K.M. De Silva, David K. Harrison, and Volker Knoblauch. "Comprehensive study on the influence of different pretreatment methods and structural adhesives on the shear strength of hybrid CFRP/aluminum joints". In: *Journal of Adhesion* 98.12 (2022), pp. 1772–1800. ISSN: 15455823. DOI: 10.1080/00218464.2021.1938004.

[66] Jochen Schanz, Sara Nester, Dieter Meinhard, Timo Pott, Harald Riegel, Anjali K.M. De Silva, David K. Harrison, and Volker Knoblauch. "Adhesively bonded CFRP/Al joints: Influence of the surface pretreatment on corrosion during salt spray test". In: *Materials and Corrosion* 73.2 (Feb. 2022), pp. 158–170. ISSN: 15214176. DOI: 10.1002/maco.202112752.

[67] Yongsoon Shin, Yao Qiao, Yelin Ni, Jose L. Ramos, Ethan K. Nickerson, Daniel R. Merkel, and Kevin L. Simmons. "Interfacial bond characterization of epoxy adhesives to aluminum alloy and carbon fiber-reinforced polyamide by vibrational spectroscopy". In: *Surfaces and Interfaces* 42 (Nov. 2023), p. 103346. ISSN: 2468-0230. DOI: 10.1016/J.SURFIN.2023.103346.

[68] Sofia Teixeira de Freitas, Dimitrios Zarouchas, and J. A. Poulis. "The use of acoustic emission and composite peel tests to detect weak adhesion in composite structures". In: *Journal of Adhesion* 94.9 (July 2018), pp. 743–766. ISSN: 15455823. DOI: 10.1080/00218464.2017.1396975.

[69] Hans Maria Tensi. *THE KAISER-EFFECT AND ITS SCIENTIFIC BACKGROUND*. Tech. rep. Journal of Acoustic Emission Vol. 22, 2004.

[70] *Test Method for Hydrophobic Surface Films by the Water-Break Test*. West Conshohocken, PA, Apr. 2021. DOI: 10.1520/F0022-13R21. URL: http://www.astm.org/cgi-bin/resolver.cgi?F22-13R21.

[71] Andrew J. Timmis, Alma Hodzic, Lenny Koh, Michael Bonner, Constantinos Soutis, Andreas W. Schäfer, and Lynnette Dray. "Environmental impact assessment of aviation emission reduction through the implementation of composite materials". In: *International Journal of Life Cycle Assessment* 20.2 (Feb. 2015), pp. 233–243. ISSN: 16147502. DOI: 10.1007/s11367-014-0824-0.

[72] Toppr. *Plastic Deformation*. https://www.toppr.com/guides/physics/elasticity/plastic-deformation/. 2023.

[73] Chris Worrall, Kellar E, and Vacogne C. *JOINING OF FIBRE-REINFORCED POLYMER COMPOSITES*. Tech. rep. Composites UK, 2020.

[74] Zi Long Zhou, Jing Zhou, Long Jun Dong, Xin Cai, Yi Chao Rui, and Chang Tao Ke. "Experimental study on the location of an acoustic emission source considering refraction in different media". In: *Scientific Reports* 7.1 (Dec. 2017). ISSN: 20452322. DOI: 10.1038/s41598-017-07371-w.

[75] Natalie Zimmermann and Peng Hao Wang. "A review of failure modes and fracture analysis of aircraft composite materials". In: *Engineering Failure Analysis* 115 (Sept. 2020). ISSN: 13506307. DOI: 10.1016/j.engfailanal.2020.104692.